Title

An Automated Microscope System to Monitor Dynamic Stress Responses in Neurons

Permalink

https://escholarship.org/uc/item/8p25k1x3

Author

Daub, Aaron C

Publication Date

2013

Peer reviewed|Thesis/dissertation

An Automated Microscope System to Monitor
Dynamic Stress Responses in Neurons

by

Aaron C. Daub

DISSERTATION

Submitted in partial satisfaction of the requirements for the degree of

DOCTOR OF PHILOSOPHY

in

Bioengineering

in the

GRADUATE DIVISION

of the

UNIVERSITY OF CALIFORNIA, SAN FRANCISCO

AND

UNIVERSITY OF CALIFORNIA, BERKELEY

Dedication and Acknowledgments

I have had the great fortune to be surrounded by an intelligent, thoughtful and caring group of individuals through my graduate school career. The following work is a result of the small and large contributions of these individuals, and I would surely not have been able to complete my Ph.D. without their invaluable advice, suggests, and overall support. The Finkbeiner lab is a unique place to do science. When I set out to find a lab, in addition to exciting science, I was looking for an environment where I would be supported irrespective of how well my project was going. In all of you, I found the types of people that would not only be my colleagues, but also my friends. You have all, in your own way, truly been friends and supported me through my ups and downs. You have seen me through one of the most challenging periods of my life, when I have matured as an individual and as a professional. I am indebted to your talent, your judgment and your character. Thank you for helping me be a better scientist and more engaged human being.

There are a few individuals that I had particularly close relationships with, and I would like to give them special acknowledgement at this time. As an engineer feeling a little uneasy about doing science at the bench, Montserrat Arrasate was brave enough to take me on as a rotation student and teach me the basics of culturing neurons, running gels, and cloning. I have not met a more kind and generous person than Montse, and I was truly fortunate to have her as my first mentor in lab. She was incredibly patient with my amateur mistakes and always provided the most positive outlook on my failed experiments. I have modeled my

own mentoring after the model demonstrated by Montse, and I know that she has helped me be a more patient and positive individual. Thank you Montse for your goodness of heart and teaching me wet lab techniques for the first time. I will always have fond memories of the time we were able to see Barcelona together with the group at Candlestick Stadium. The lab gave me a Barcelona Messi shirt at my exit talk, so I am now a true Catalan! I also want to recognize Punita Sharma for working hand and hand with me over my first two years in lab. We learned a lot together improving the screening capabilities of the robotic microscope. Thank you for being my partner in crime, often tag teaming on ridiculous schedules for imaging plates or repairing the microscope. Your very generous contributions to the technology and my learning were invaluable in taking the analysis and hardware development of the microscope to another level. Ana Oliveira, it has been a joy working with you to finish up critical experiments as I head back to medical school. Thank you for your ever positive attitude and willingness to learn techniques while putting up with my obsessive compulsive tendencies. You have filled my last days in lab with many smiles. I would also like to give special acknowledgement to Jason Miller for being the best possible example of a successful graduate student for all of us who were young and somewhat naïve in the lab. Your example and dedication to science is truly admirable. I was often in awe over the detail and skill you demonstrated while carrying out experiments. You were truly driven to understand every aspect of what you did, and I was fortunate to see the results of your hard work. Most importantly, you provided an example of the connection between hard work,

talent, and success. It gave me hope that although not inevitable, this type of dedication will maximize the chances of high achievement. I also was able to mature as an engaged citizen by seeing your work with Darfur and the numerous emails you shared about policy, social equity and the importance of contributing a voice to the larger problems that challenge society each day. I look forward to the many contributions you will make over the course of your career. I know they will be significant.

My two super post-docs that I relied on immensely throughout my years in lab were Gaia Skibinski and Sami Barmada. I cannot fully explain how talented and hard working they are. Gaia, in addition to always wearing a contagious smile and exuding positivity, you taught me how to be a good scientist. Thank you for your continual guidance in my project and being a sounding board for my experiments and ideas. Our discussions were always very fruitful and they always made my experiments better controlled and more likely to yield an interpretable result. I learned from your time management skills and thorough analyses. Thank you also for becoming a dear friend over these past five years. Sami, outside of Steve, you have probably been my most significant mentor in lab. You have stood as an example of the MD/PhD career track, and your career guidance has really been a source of inspiration and support as I worked towards my own PhD. When I was frustrated with my project, seeing you bike to clinic to see patients and then return to complete experiments was inspiring, and I was able to witness firsthand how your extensive medical knowledge was able to inform and motivate your work. Thank you for providing extensive comments on

my grant applications and for your curbside consults. You have been a continued source of trusted advice in both my professional and personal life. I will always remember our crazy sprint triathlon in Oakdale.

There are two very special friends and fellow graduate students that made my experience in lab significantly more fun and unpredictable. Nothing could replace the camaraderie of these two friends who were going through the same training as me. We were able to pick each other up when our spirits were low and share in each others' accomplishments. Ian Kratter, your humor definitely spiced up my days and, I could always rely on you to say the things that I might have been thinking but wasn't willing to say. Thank you for convincing me to submit an abstract to Society for Neuroscience (SFN) before I was ready and to help in my graduation decision. Submitting my work to SFN helped me to organize my data and set me up for an earlier graduation. Over these years, you have become a true friend, sharing many hard fought soccer games and discussing some of the most important decisions in our lives. I look forward to your continued support and friendship in our two years of medical school together. Hengameh Zahed, your kind soul has been a steady force of reassurance for me. Thank you for your always enlightening insight into my experimental results and advice on techniques. I have also enjoyed all our robotic microscope troubleshooting together! You have a gift of being able to make others feel better, building those up around you. You do give immensely and deserve much in return. Many thanks for all the times you put a plate on for me or helped out with finishing an experiment of mine. I will always remember our Vegas and Tahoe trips together.

These are as much a part of my graduate school experience as the science. I know our friendship will continue for many years, hopefully with another chance to shop together.

Special acknowledgement is certainly reserved for Steve Finkbeiner. Steve, I still clearly remember the first time I came to interview for the MSTP at Gladstone. I walked into your office a little nervous, wondering what details you were going to drill me on about my research. Instead, you welcomed me with a big smile and immediately helped me feel at ease. We went on to talk more about how beautiful the human body is and what a privilege it is to be able to discover its workings. You have repeatedly demonstrated over the course of my graduate career how brilliant you are, and I can only hope that some of this intelligence has been passed down to me. In truth, I have learned a tremendous amount about how to do good science under your tutelage. Through your extensive comments on my writing, you have helped me become a better scientific writer. I have been able to learn how to conduct controlled experiments and be able to better interpret results based on the discussions we had during my weekly meeting time. I am also thankful for the confidence that you have in all of your students. You place a lot of responsibility in our hands by asking us to present to academic and industry collaborators as well as negotiate and decide on major lab purchases. On numerous occasions, you were willing to put significant money towards an idea I had. Thank you for your confidence in my judgment and ability. Thank you also for always making sure to acknowledge the work that I and others did in the lab. Your special mention leaves a deep impression in the minds

of us as young scientists and reminds us all of the humbling fact that science is, at every level, a collaborative endeavor.

I lastly and most importantly want to thank my family. Mom, Dad, Heidi, Benoy, Elina, Ursula, Logan, Papa Uwe, Maperanza and my dear wife Tess. Dad, I remember you showing me the starry sky at a young age and exposing me to the wonders of the universe. It was always you who asked me why things were the way they were and inspired my appreciation for the beauty and logic of the scientific world. You were the major force behind my subsequent desire to explore and have the tenacity to replace ignorance with understanding. Mom, you provide a constant source of love and confidence in my life. Your unwavering trust in my decisions and willingness to support me, irrespective of the path I take, are gifts that I could never buy or replace. Mom and Dad, together you have financially supported the best education that I could ever hope for and as such, provided the types of opportunities that I dreamed of as a child. Heidi and Benoy, thank you for your incredible generosity throughout my graduate years. You have opened up your home to the whole family on a number of occasions and have gone out of your way to make me feel special on birthdays and other holidays. Heidi, I have really enjoyed discussing our clinical careers and the art of manuscript writing and publishing. Our career paths are converging to a certain extent, and I look forward to many more times where we can support each other. I have to give an extra special thanks to Tess, the love of my life, for putting up with my ridiculous schedule over the course of my Ph.D. I apologize for the late nights and constant inaccuracies in my estimated finishing time. I've lost count of

how many times you drove with me to lab late at night or on the weekends so that I could image a plate or finish an experiment. You have the patience of a saint, and I truly could not have finished the work I needed to get done without your understanding and forgiveness. Your smile when I arrived home each day was a source of immeasurable happiness for me, and all of our adventures to India, Peru, Hawaii, Greece and many more will be inextricably tied to these years of my life. I love you dearly.

Contributions of Others in Work Presented

I am indebted to a number of collaborators that contributed to the work presented in this dissertation. Punita Sharma carried out all of the optimization for 96-well microtiter plates. Punita also made significant contributions to the acquisition and analysis of the BDNF data used to validate the robotic microscope system for screening. Mike Ando made important contributions to the development of the image analysis pipeline. I would also like to thank Gaia Skibinski for providing the results of her data showing Nrf2 modificaiton of α-synuclein, which was used to validate the automated image analysis. Ana Oliveira helped with the qPCR data presented in Chapter 5. Ana also conducted the HSF1 nuclear translocation experiments in their entirety.

Chapter 2 of this work was originally published as Daub A, Sharma P, Finkbeiner S (2009) High-content screening of primary neurons: Ready for prime time. Current Opinion in Neurobiology 19:537-543.

Portions of the following work were also taken from Sharma P, Ando DM, Daub A, Kaye JA, Finkbeiner S (2012) High-throughput screening in primary neurons. Methods Enzymol 506:331-60.

Abstract

An Automated Microscope System to Monitor

Dynamic Stress Responses in Neurons

by

Aaron C. Daub

Despite years of incremental progress in our understanding of diseases such as Alzheimer's disease (AD), Parkinson's disease (PD), Huntington's Disease (HD), and amyotrophic lateral sclerosis (ALS), there are still no disease-modifying therapeutics. The discrepancy between the number of lead compounds and approved drugs may partially be a result of the methods used to generate the leads and highlights the need for new technology to obtain more detailed and physiologically relevant information on cellular processes in normal and diseased states. We developed a high-throughput automated microscope system and primary neuron model of HD that allows us to monitor dynamic stress responses in intact, fully differentiated neurons. We are able to assay thousands of conditions, including millions of neurons, in a short period of time, which can reveal completely new aspects of biology and identify lead therapeutics in the span of a few months when conventional methods could take years or fail all together. We use this system to understand how neurons, a long-lived, postmitotic cell type, differ in their acute responses to proteotoxic insults including those associated with malformed protein. We show that neurons have a deficient acute stress response to multiple known stimuli, including thermal

stress, Hsp90 inhibition, and proteasome inhibition. We find that neurons have low expression of the two major stress-responsive transcriptional activators in mammals, HSF1 and HSF2. We also find that neurons have high constitutive chaperoning capability through relatively high levels of Hsp90 and Hsc70. High Hsp90, however, decreases the acute stress response through negative regulation of HSF1. By increasing HSF1 levels, we were able to restore the response in neurons and protect them from the toxicity associated with malformed protein. We propose a mechanism for the attenuated acute stress response in neurons that implicates a high Hsp90 to HSF1 ratio, which results in an increased ability to cope with chronic stresses, but decreased ability to respond acutely when basal homeostatic responses are overwhelmed. We conclude that targeted therapies to bolster acute stress responses in neurons through increasing HSF1 expression or activation will therefore benefit HD and other neurodegenerative disorders of protein conformation.

Table of Contents

List of Tables

List of Figures

Chapter 1

Introduction

Normal cell function requires the proper expression, folding, and degradation of proteins. Perturbations in the elaborate machinery that regulates these processes, resulting in abnormal protein homeostasis or proteostasis, lead to protein misfolding and disease. Neurodegenerative conditions, such as Alzheimer's disease (AD), Parkinson's disease (PD), Huntington's disease (HD), amyotrophic lateral sclerosis (ALS), and frontotemporal dementia (FTD) share a common thread of protein misfolding, aggregation, and accumulation within the brain(Soto, 2003). Although protein misfolding is integrally involved in development of these disorders, it is unknown how malformed protein perturbs cellular proteostasis machinery on a systems level or how individual pathways involved in protein homeostasis contribute to adaptive or maladaptive protein maintenance and cell fate. We developed primary neuron models of neurodegenerative disease and live-cell automated microscopy to study the effect of aggregation-prone proteins *in situ*.

Our lab has established a primary neuron model of HD that is both physiologically relevant and amenable to high-throughput assays(Arrasate et al., 2004; Saudou et al., 1998; Daub et al., 2009). The model recapitulates over 14 features of the disease seen in HD patients. In a number of cases, this model has shown HD pathogenic mechanisms that were later validated *in vivo*(Arrasate et al., 2004; Mitra et al., 2009; Humbert et al., 2002; Miller et al., 2010a). Fluorescence readouts in this HD model are measured by a customized automated microscope system that has the unique ability to capture hundreds to thousands of images from multi-well plates and return to the same fields of view over time(Arrasate and Finkbeiner, 2005). This combination enables the

physiological processes of large cohorts of individual cells to be monitored in real time, yielding dynamical measurements that would otherwise not be possible with fixed endpoint analysis. The system has already led to novel findings on the relationships between Htt levels, polyQ length, IB formation and cell death, and has further shown the dynamics of UPS dysregulation and conformation specific toxicity(Miller et al., 2010a; Arrasate et al., 2004; Mitra et al., 2009; Miller et al., 2011). With our longitudinal imaging, we are able to capture transient cellular responses that would be missed if imaged at a single point in time. Chapter 2 provides a rationale and theoretical framework for adapting our automated microscope and primary neuron model of HD to high-throughput screening. It also introduces the reader to high-content analysis and the benefits of its combined use with high-throughput screening.

Chapter 3 describes the significant technological advancements that were necessary to adapt this existing system to high-throughput assays. We required that all the capabilities of the system were retained, but we sought to extend the system to work with 96-well microtiter plates and automate certain steps of the pipeline where manual intervention was previously necessary. We further wanted to increase the richness of the measurements by greatly expanding the number of morphology- and intensity-based cellular parameters we extracted. We split the system into two broad logical grouping, namely acquisition and analysis. Acquisition captures multi-wavelength fluorescence from cells expressing fluorescent proteins or reporters using automated scripts that control an inverted microscope. Analysis processes these raw images and performs a series of steps to identify cells and extract multiparametric information. We envisioned a number of different types of screens that could be performed, each requiring a unique set of fluorescent proteins or reporters and imaging frequency. We therefore made both

the acquisition and analysis pipelines customizable through user-defined parameters and protected the core functionality common to all automated microscope assays.

We used our automated microscope system to monitor the heat shock response (HSR) in neurons to determine how they respond to the stress associated with malformed proteins, including huntingtin protein with an abnormally expanded polyglutamine (polyQ) repeat (mHTT). The HSR is the major inducible stress response to acute proteotoxic stresses and one of the most important protective pathways cells use to guard against detrimental perturbations to the folding state of their proteome. Chapter 4 gives a brief introduction to the genetic cause of HD and how the resulting polyQ expansion places a significant burden on multiple cellular proteostasis pathways. A case is made for HD being, at its root, a disease of protein conformation or a proteopathy. We therefore wanted to understand why neurons, when compared to other cell types within the CNS and body show differential susceptibility to malformed protein. Neurons are unique in that they are a long-lived, post-mitotic cell type with high metabolic demands due to their activity and morphology. Neurons that are born in the developing mammalian brain often have lifetimes only limited by the lifetime of the organism. We hypothesize that the proteostasis network neurons use to maintain their proteome and buffer environmental stresses under normal conditions has the unintended effect of sensitizing them to stochastic acute challenges that occur more frequently due to the concomitant stress of the disease-associated protein. In Chapter 5, we show that neurons have high expression of constitutive chaperones that increase their chronic homeostatic capacity. However, this coupled with low expression of HSF1, the master regulator of the HSR, negatively regulates the acute stress response. Neurons therefore have a decreased ability to respond to acute stresses and restore proteostasis when chronic homeostatic responses are overwhelmed.

The interconnected and dynamic nature of cellular stress responses requires monitoring systems that can match the dynamic nature of the biology. We present an automated microscope system that can accomplish this and simultaneously acquire data from thousands of cells with hundreds of different conditions. We use the system and complementary biochemical approaches to understand the neuron specific stress response system. This heightened understanding will help in the development of proteostasis therapeutics that target malformed proteins central in HD and other neurodegenerative diseases.

Chapter 2

High-Content Screening of Primary Neurons: Ready for Prime Time

Aaron Daub[1,2,3,6], Punita Sharma[1,3,6], and Steven Finkbeiner[1,3-5*]

[1]Gladstone Institute of Neurological Disease, San Francisco, CA 94158

[2]Medical Scientist Training Program and Program in Bioengineering, University of California, San Francisco, 94143

[3]Taube-Koret Center for Huntington's Disease Research and the Consortium for Frontotemporal Dementia Research, San Francisco, CA 94158

[4]Program in Biomedical Sciences, Neuroscience Graduate Program, Biomedical Sciences Program, University of California, San Francisco, 94143

[5]Departments of Neurology and Physiology, San Francisco, CA 94143

[6]These authors contributed equally to this work.

*Corresponding author: Finkbeiner, Steven (sfinkbeiner@gladstone.ucsf.edu)

Summary

High-content screening (HCS), historically limited to drug-development companies, is now a powerful and affordable technology for academic researchers. Through automated routines, this technology acquires large datasets of fluorescence images depicting functional states of thousands to millions of cells. Information on shapes, textures, intensities, and localizations is then used to create unique representations, or "phenotypic signatures," of each cell. These signatures quantify physiologic or diseased states, for example,

dendritic arborization, drug response, or cell coping strategies. Live-cell imaging in HCS adds the ability to correlate cellular events at different points in times, thereby allowing sensitivities and observations not possible with fixed endpoint analysis. HCS with live-cell imaging therefore provides unprecedented capability to detect spatiotemporal changes in cells and is particularly suited for time-dependent, stochastic processes such as neurodegenerative disorders.

Introduction

Biological research is entering a new era. Molecular biology will be combined with novel engineering technologies and increased computational power to examine living systems in exciting new ways.

We are only beginning to understand the benefits—in fact, the necessity—of studying biological systems with large-scale unbiased screens (Friedman and Perrimon, 2007). Here we focus on high-content screening (HCS) and considerations needed to use this method effectively to study normal and disease physiology in primary cells, currently the most biologically relevant models.

Why high-content screening?

HCS is a multiplexed, functional screening method based on extracting multiparametric fluorescence data from multiple targets in intact cells(Giuliano et al., 1997; Krausz, 2007). By temporally and spatially hresolving fluorescent readouts within individual cells, HCS yields an almost unlimited number of kinetic

and morphometric outputs. HCS was developed to facilitate drug-target validation and lead optimization before costly animal testing(Giuliano and Taylor, 1998). Today it is broadly used to catalog cellular, subcellular, and intercellular responses to multiple systematic perturbations and is applicable to basic science, translational research, and drug development(Doil et al., 2009; Loh et al., 2008; Zhang et al., 2007a; Young et al., 2008). We distinguish HCS from high-content analysis (HCA). HCA refers to extracting information from image data. HCS is the automated, high-throughput application of HCA.

HCS can fill a gap in academic research. Our growing awareness of biological complexity underscores the need to examine more than one variable at a fixed point in time. Traditional low-throughput methods have severe limitations. For complex systems with many interacting genes, measuring any single perturbation is not very informative. For gain-of-function diseases, especially those with late onset, a toxic gain-of-function may not be related to a protein's normal function. Unbiased screens therefore identify potential pathogenic mechanisms faster and more comprehensively, and the large datasets are less prone to sampling error when analyzing stochastic events.

HCS assays capture cell-system dynamics and exploit typically confounding cell-to-cell variability. For example, a recent study used simultaneous tracking of ~1000 proteins in lung carcinoma cells after drug treatment to detect time-dependent proteomic changes that predicted individual cell fate(Cohen et al., 2008). Hypotheses in HCS are used to design tracked variables and outputs that maximize the likelihood of meaningful results. We labeled mutant huntingtin and

measured cell survival to determine the role of inclusion bodies in Huntington's disease (HD)(Arrasate et al., 2004), a question unanswered by 10 years of time-invariant, low-throughput approaches. HCS provides large datasets that unveil multiple, often nonintuitive, correlations that seed subsequent lines of thought. Thus, HCS accelerates the iterative process of classical hypothesis-driven research(Smalheiser, 2002).

Primary cells or cell lines?

Choosing the best cell type for a particular HCS assay is challenging. Each option comes with inherent benefits and drawbacks (Table 1). Primary cells provide high-quality models for several reasons. They are more physiologically relevant than immortalized cell lines(Nolan, 2007). They form synapses, thus incorporating significant neuromodulatory and trophic inputs. Neuronal physiology and disease are also notoriously cell-type specific, and neurons differentiated in vivo best recapitulate actual neuronal subpopulations. One study found hepatoma cell lines differ

Property	Immortalized cells	Primary Neurons	Embryonic stem cells	Induced pluripotent stem cells
Current use in HCS	Ubiquitous	Limited	Differentiation screens	Differentiation screens
Ready for HCS	Yes	Yes	No	No
Source	Specific to cell line	Animal tissue • Specific brain regions	Established or new cell line • From human or animal embryos	Established or new cell line • From human or animal fibroblasts (most common)
Freeze/Thaw	Yes	Once	Yes	Yes
Proliferative capacity	Very High	Post-mitotic	High • Murine better than human	High • Murine better than human
Differentiation required	In some cases	No	Yes	Yes
Population type	Clonal or Heterogeneous	Heterogeneous	Clonal → Heterogeneous	Clonal → Heterogeneous
Handling	Durable	Sensitive	Sensitive	Sensitive
Ability to be engineered	High	Limited	Medium to high	Medium to high
Cost	Low	High	Medium	Medium
Physiologic relevance	Low	High	Medium to high	Medium to high
Major challenge for HCS	• Physiologic relevance	• Limited human source • Labor intensive	• Limited human source • Differentiation • Quality control	• Dedifferentiation • Differentiation • Quality control
Major benefits for HCS	• Quantity • Engineering	• Physiologic relevance	• Quantity • Diversity of cell types	• Quantity • Diversity of cell types • Patient-specific screening

Table 1. Neuronal cell models for HCS. The advantages and disadvantages of different cell types are summarized for their use in HCS. Adapted from Eglen *et al*(Eglen et al., 2008).

profoundly from primary hepatocytes, consistent with a shift from oxidative to anaerobic metabolism, upregulation of mitotic proteins, and downregulation of typical hepatocyte functions(Pan et al., 2009). High attrition rates for candidate neuropharmacologics (Fig. 1) suggest even more striking differences in neurons.
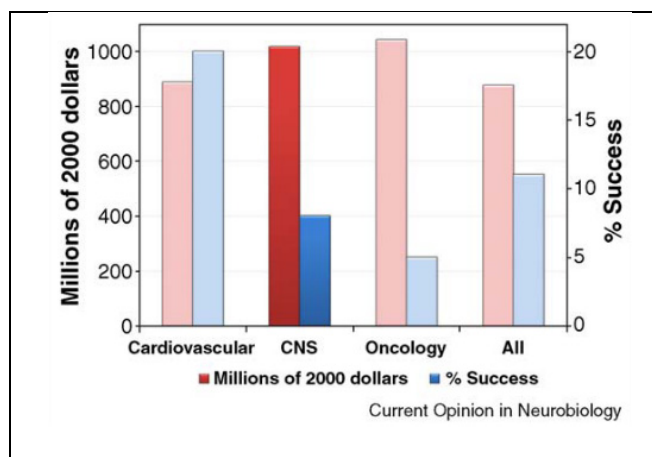
Figure 1. Success rates and millions of dollars spent from first-in-man to registration by therapeutic area. The overall clinical success rate is 11% with ~900 million dollars spent. However when the analysis is carried out by therapeutic area, big differences emerge with central nervous system (CNS) and oncology trailing far behind cardiovascular diseases in the % success rate compared to the dollars spent(Kola and Landis, 2004; Adams and Brantner, 2006).

Most screenings have involved cell lines, but future screenings will use primary and stem cells(Eglen et al., 2008; Rubin, 2008). Embryonic stem (ES) cells can be differentiated into motor neurons in large numbers(Di Giorgio et al., 2007). Mouse and human induced pluripotent stem (iPS) cells(Takahashi and Yamanaka, 2006; Takahashi et al., 2007) may better predict in vivo drug side effects and are particularly attractive for disease-focused HCS(Rubin, 2008; Di Giorgio et al., 2007; Takahashi and Yamanaka, 2006; Takahashi et al., 2007; Dimos et al., 2008; Ebert et al., 2009; Soldner et al., 2009). For example, iPS

cells from patients with spinal muscular atrophy differentiated into motor neurons retained pathological deficits and drug responses consistent with the disease. More work is needed to characterize iPS cell lines, and better dedifferentiation protocols will avoid viral vectors and oncogenes(Soldner et al., 2009; Stadtfeld et al., 2008; Okita et al., 2008; Kaji et al., 2009). Ultimately, HCS will place additional demands on dedifferentiation and redifferentiation, including high efficiency and reproducibility. High throughput screens are already helping to address these needs(Ivanova et al., 2006; Borowiak et al., 2009).

Despite technical challenges in isolating, culturing, and transfecting primary neurons, their use decreases false negatives and saves time and money wasted on pursuing false positives. Until protocols are improved for differentiating ES and iPS cells into many neuronal cell types, primary cells will remain the most physiologically relevant model for large-scale screens.

HCS planning for live-cell imaging

Assay development encompasses selecting fluorophores and proteins to label, choosing a transfection method, migrating to 96- or 384-well formats, upgrading automation, and completing preliminary experiments to determine robustness of readouts. None of these steps are trivial. Migrating to a new format alone requires re-optimizing labware, intra- and inter-well cell distributions, and transfection and image-acquisition protocols. During this time, a lab data management system must also be integrated.

Fluorophores. Excellent reviews describe fluorophores for HCA(Shaner et al., 2007; Giepmans et al., 2006). Notably, mKate (Shcherbo et al., 2007) (now mKate2), mOrange2 and TagRFP-T(Shaner et al., 2008), and EBFP2 (Ai et al., 2007) provide improved brightness and photostability. After balancing these features, the best options for live-cell imaging are listed in Table 2. HCS allows up to four fluorophores with sufficient spectral separation to avoid crosstalk. In the future, more channels will be simultaneously acquired with spectral imaging(Zimmermann, 2005).

Fluorescent Protein*	Spectral Class	Excitation peak (nm)	Emission peak (nm)	Brightness[†]	Photostability[‡]	pKa[‡]	Association state[‡]	Filter Set[§]
EBFP2	Blue	383	448	18	55	5.3	Weak dimer	DAPI/BFP
mCerulean	Cyan	433/445	475/503	27/24	36	4.7	Monomer	CFP
mEGFP	Green	488	507	34	174	6.0	Monomer	FITC/GFP
mEmerald	Green	487	509	39	101[¶]	6.0	Monomer	FITC/GFP
EYFP	Yellow	514	527	51	60	6.9	Weak dimer	FITC/YFP
mCitrine	Yellow	516	529	59	49	5.7	Monomer	FITC/YFP
mOrange2	Orange	549	565	35	228	6.5	Monomer	TRITC/DsRed
TagRFP-T	Orange	555	584	33	337	4.6	Monomer	TRITC/DsRed
mCherry	Red	587	610	17[††]	96	<4.5	Monomer	TxRed
mKate2	Far-red	588	633	25	118	5.4	Monomer	TxRed

Table 2. Recommended fluorescent proteins. Physical properties for fluorescent proteins (FPs) in each spectral class. *Common literature FP abbreviation. [†]Product of the molar extinction coefficient and the quantum yield $(mM \times cm)^{-1}$. [‡]Literature values except as noted. [§]Specialized applications may require choosing filter combinations that closely match the spectral profiles [50]. [¶]Measured in live cells with mEGFP ($t_{1/2}$=150 seconds) as a control. [††]Averages of literature values. Adapted from Shaner *et. al.*(Shaner et al., 2007; Shaner et al., 2008).

Transfection. Lipid-based methods, Ca^{2+}-phosphate co-precipitatation, viral infection, electroporation, and nucleofection all have benefits and drawbacks(Zeitelhofer et al., 2007). Primary neurons pose additional challenges: they are susceptible to transfection toxicities and plagued by low transfection efficiency(Halterman et al., 2009). We found Lipofectamine 2000 (Invitrogen) best for efficiency, cell viability, and automation in assays that require transfection after cell plating. With this reagent, most transfection variability results from cell-plating density, total mass of DNA, and ratio of transfection reagent to DNA. These factors must be optimized for specific cells and DNAs. Reverse transfection with this reagent now makes arrayed libraries of transfection-ready DNA and siRNA a reality for HCS(Erfle et al., 2007; Erfle et al., 2008). Although biochemical assays of large numbers of pooled cells rely on high transfection efficiencies, this actually complicates microscopy-based screening of individual cells. Identifying the same cell over time can be confounded by cell movement. The researcher must strike a balance between maximizing transfected cell number per field and verifying the ability of image-analysis algorithms to accurately track the cells.

Automation. Automation can be applied to each step of HCS, including sample preparation, image acquisition and analysis, quality-control measures, and data reporting. Highly capable liquid-handling robots are increasingly affordable for individual labs. They represent scalable options for liquid aspiration and dispensing of large and small volumes. Multiple high-content microscopy systems are now available(Lang et al., 2006). The most popular use confocal or

wide-field microscopes, and all offer hardware autofocus, options for environmental control, and data management and image-analysis software. They provide out-of-the-box access to HCS for many scientific applications. Downsides to these solutions include expense, proprietary image formats and algorithms, and the inability to write ground-level scripts for true user customization. Lab automation upgrades should be integrated early into low-throughput assay development so quality measures are determined from datasets reflecting the automation.

Robustness. Minimizing assay variability is essential for HCS. The Z'-factor is a useful way to estimate assay quality and is calculated as a signal detection window between positive and negative controls scaled by the dynamic range(Zhang et al., 1999). It is an excellent measure of single-output assays. Since HCS allows powerful multiparametric analyses with potentially hundreds of quantified parameters, a Z'-factor can be calculated individually for each parameter(Abraham et al., 2008). Alternatively, multivariate criteria without informational losses due to averaging can be instituted from the beginning(Loo et al., 2007). In either case, large data sets from positive and negative controls should be used to determine assay quality before initiating screening.

Data Management. HCS datasets are large. Live-cell imaging of a single 96-well plate with three channels and nine images per well yields ~30 GB of raw image data. A reliable informatics infrastructure is needed. Data should flow seamlessly from acquisition to storage on a server where it can be accessed for offline image analysis. Initially, hierarchal file structures can be used, but optimal management

14

should include a central database for storing images and metadata that can be accessed by both acquisition and image-analysis software(Swedlow et al., 2009).

Image analysis, the new bottleneck

Automation advancements have been valuable for HCS, but extracting meaningful data from complex image sets poses major challenges. These challenges arise from a combination of microscopy and image-processing limitations and the need for new statistical tools. Neuroscience poses particular difficulties due to complexities in neuronal morphology and subcellular trafficking. Most laboratories use image-analysis algorithms and manual labor to analyze images, but the throughput is too low for HCS. More robust and accurate image-analysis algorithms that can be applied to entire data sets with minimal user intervention are necessary(Jones et al., 2009). Zhang *et al.* published a neurite extraction algorithm(Zhang et al., 2007b) for HCS, and multiple commercial packages quantify neuronal bodies and neurites. To understand HCS informatics problems more fully, we refer you to excellent reviews(Zimmer et al., 2006; Meijering et al., 2006; Xiaobo and Wong, 2006).

HCA uniquely provides multiplexed quantification of individual cell features with temporal and spatial resolution. Image analysis comprises image segmentation and cell tracking, extraction of individual cell features, and data modeling and classification(Xiaobo and Wong, 2006). Image-analysis programs routinely measure size, shape, intensity, texture, moments, and subcellular localization that, when combined, yield hundreds of parameters that characterize a specific

cell phenotype(Glory and Murphy, 2007). For example, Loo *et al*. used ~300 unbiased parameters and a multivariate clustering algorithm to determine separation between drug-treated HeLa cells and controls(Loo et al., 2007). The redundancy of this parameter set was reduced, resulting in a minimal phenotypic signature of the treated cells at various drug dosages. With the signatures, a drug class could be predicted, and therapeutic windows could also be deduced. The close relationship of neuronal morphology and functional state (Rocchi et al., 2007) holds promise for similar phenotypic signatures to emerge from HCS focused on neuronal development, physiology, and disease. For instance, an HCS study of cultured rat primary cortical neurons identified $A\beta_{1-42}$ induced reduction in neurite outgrowth with no apparent effect on neuron number, pointing to more subtle morphological changes that can precede cell death. These studies used fixed-cell imaging, however, the full potential of HCS will be realized with imaging live cells over time(Neumann et al., 2006; Harder et al., 2009).

HCS and live-cell imaging of primary neurons: putting it all together

HCS with live-cell imaging in relevant neuronal models promises to elucidate physiologic and pathophysiologic processes with unprecedented sensitivity and correlative power. Live-cell imaging captures cell phenotype changes. Thus, previously static features are transformed into dynamic features where timed occurrences and rates of change generate more informative phenotypic signatures. Imaging in live cells also permits cause-and-effect relationships to be determined. We use this novel approach to investigate pathogenic mechanisms

of neurodegenerative disorders, including HD, Parkinson's disease, and frontotemporal dementia. Our system (Fig. 2) allows us to correlate events in thousands of neurons to individual cell fates—enabling us to determine if the events are adaptive, maladaptive, or incidental to disease progression(Arrasate and Finkbeiner, 2005). For instance, we used live-cell imaging in a primary neuron model of HD to establish a mitigating role for inclusion bodies (Loh et al., 2008) and reveal the interplay between ubiquitin-proteasome system function and inclusion body formation(Mitra et al., 2009). Such studies necessitate large sample sizes and the ability to follow individual neurons over time. They highlight the power of HCS, when coupled with live-cell imaging, to reveal causal relationships in biological processes.
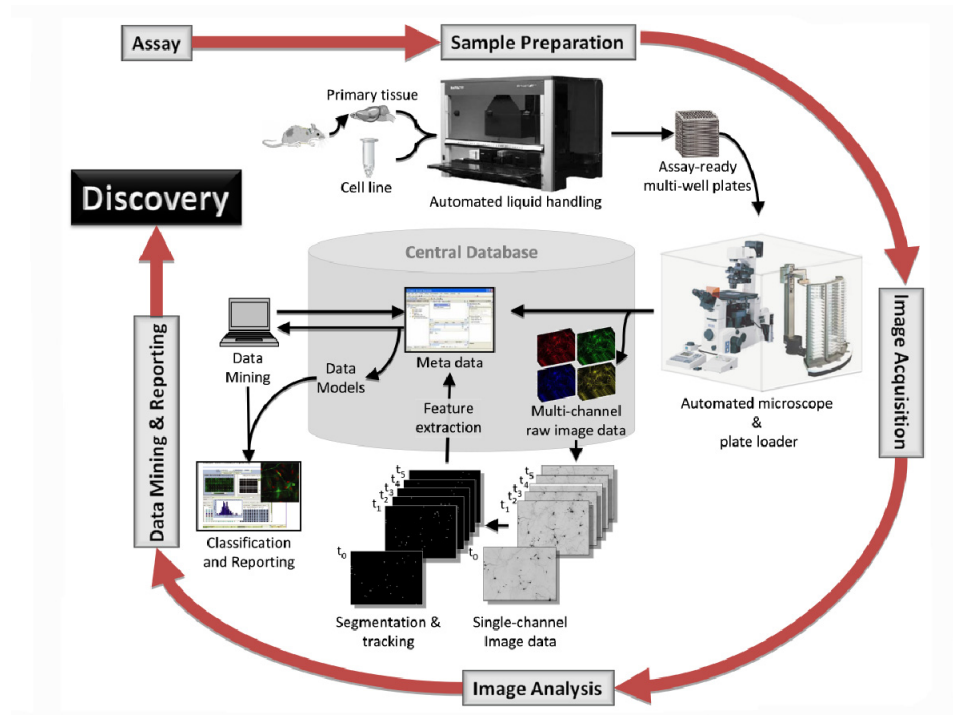
Figure 2. Workflow of our second generation high content screening system for live-cell imaging. Our system uses primary neurons from embryonic mice. A Microlab STARlet (Hamilton, Reno, CA) automated pipetting workstation prepares and transfects cells in 96-well plates, which are then transferred to the plate stacker of a KiNEDx 4-axis robot (Peak Robotics, Colorado Springs, CO). The plates are loaded onto an MS-2000 stage (Applied Scientific Instruments, Eugene, OR) fixed to a Nikon TE-2000 (Nikon, Melville, NY) microscope. The robot and microscope are enclosed in an environmental chamber (InVivo Scientific, St Louis, MO) to enable around-the-clock imaging for 6-7 days. Widefield images are acquired according to in-house scripts written in Image-Pro Plus (MediaCybernetics, Silver Spring, MD). At each time point, montage images are generated for each well and fluorophore channel. Image analysis algorithms then extract cell-based information. Metadata generated from image acquisition and analysis flows into a central database for data modeling, mining and classification.

Repeated measures of individual cells by automated microscopy facilitates use of powerful statistical techniques, such as Cox proportional hazards (CPH) analysis(Klein and Moeschberger, 2003). CPH integrates a user-defined number of parameters to determine whether they explain time-to-event outcomes, for instance cell survival. Much as in a prospective cohort study, we allow cells, through stochastic diversification, to "take on" certain traits and then retrospectively determine how significant these traits are in predicting outcomes. Our goal is to find robust, disease-specific phenotypic signatures for screening

small-molecule pharmacological agents and genome-wide siRNA libraries. CPH takes advantage of inherent cell-to-cell heterogeneity, and the increased sensitivity resulting from temporal analysis permits fewer cells to be analyzed. We therefore avoid two main drawbacks of screening in primary cells—decreased transfection efficiency and lack of cell homogeneity.

Conclusion

HCS is a technology with vast potential for academic researchers and particularly neuroscience. Large-scale screens are strategically essential in understanding complex biological systems and gain of function diseases. HCS can be applied to an incredible diversity of assay types depending on the experimental conditions and labeled proteins. Challenges still remain in image analysis and data interpretation, and new statistical tools will be necessary to analyze time-dependent processes of millions of cells across thousands of conditions. Advances in HCS will result from new microscopy techniques, such as spectral imaging, better fluorescence proteins, and the maturation of stem cell technology. Greater knowledge of what proteins to probe for particular physiologic and disease processes will increase HCS sensitivity. HCS with live-cell imaging in primary neurons is practical and will likely contribute to some of the most elusive questions in neurobiology and related disease.

Chapter 3

Developing an Automated Pipeline for Image Acquisition and Analysis

Construction of a Second Generation Automated Microscope

Our goal in building a second generation automated microscope was to increase our lab capabilities for high-throughput screening. High-throughput assays typically test hundreds to thousands of independent conditions in a single experiment. They require significant advances in automation to process samples and analyze the results in a reasonable amount of time. We leveraged the technology of the first generation automated microscope (Arrasate and Finkbeiner, 2005) and introduced a number of advancements that improved image quality and throughput. The second generation microscope was built around a Nikon TE-2000 with the first commercial hardware focusing system called Nikon Perfect Focus System (PFS). The PFS uses a long wavelength laser to reflect off the bottom of a microtiter plate and provide a constant feedback control for adjustment of the z-axis, keeping the sample in focus. This technology is faster than brightfield focusing routines that use phase information from captured images to search for an optimal focus plane(Price and Gough, 1994). It also exposes the sample to less light, which minimizes unwanted phototoxicity, photoconversion, and photobleaching. The microscope uses an Applied Scientific Instrument (ASI) (Eugene, OR) MS-2000 automated stage to precisely move and return to programmed plate coordinates over the course of each experiment with submicron accuracy (<700 nm RMS). Although linear

encoders were tried on the system to increase precision, the acquisition time significantly increased without noticeable change in the reproducibility of fields of view. We decided to use rotary control, which is still a closed loop feedback system and provided excellent image reproducibility at 20X and 40X magnification. In order to capture multi-fluorescence images, the system uses automated control of excitation and emission filters that work in combination with a multiple bandpass or polychroic filter to illuminate the sample with a very narrow spectrum of light. This corresponds to the excitation peak of the fluorophore being imaged. The wheel containing the polychroic filter moves slowly compared to the excitation and emission filter wheels, which change position in as little as 50 ms. Therefore, the polychroic filter typically remains constant for a group of wells or an entire plate, and individual fluorophores are sequentially captured by rapidly changing the filters on the excitation and emission wheels (Fig. 3). In preparation for high-throughput assays, we needed a way to run experiments on multiple microtiter plates without the user having to manually load individual plates onto the microscope. We integrated a Peak Robotics KiNEDx 4 axis robot (Colorado Springs, CO) with a 24 plate capacity plate stacker. The robot was trained with teach positions that corresponded to a safe trajectory from the plate stacker to the plate loading position on the automated stage. We designed and manufactured a customized plate holder that contained a chamfer on the holder edges that accommodated small inaccuracies in the plate grip position and still allowed for the repeatable positioning of the plate at the base of the holder. In order to
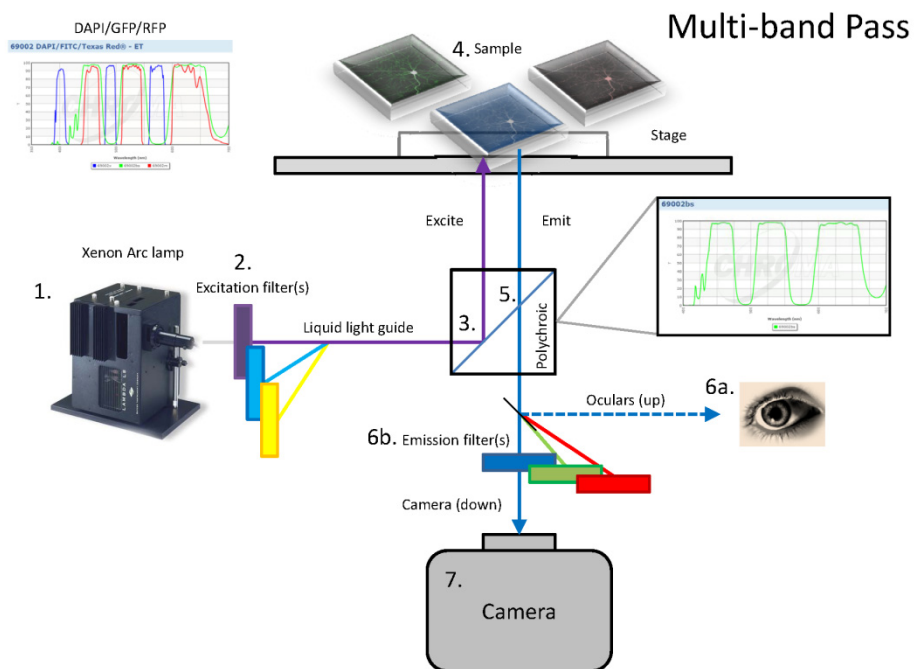
Figure 3. An inverted multi-channel fluorescence microscope. (1) Light from a full spectrum (e.g. white) light source is filtered by (2) excitation filters corresponding to the excitation peak of the fluorophore being illuminated. (3) The excitation light is reflected by a polychroic filter through the objective to illuminate the (4) sample. (5) Longer wavelength emitted light corresponding to the emission spectrum of the fluorophore is passed through the polychroic filter (other light is reflected). (6a) Light is directed to the oculars before the emission filters or (6b) light is directed to the emission filters and detected in the camera.

control for rotational displacements of the plate within the plate holder, we partnered with ASI to design a small servo that pushes the plate to one side of the holder and rigidly constrains the plate along three degrees of freedom. The entire system is enclosed within a temperature and CO_2 controlled environmental

chamber from In Vivo Scientific (www.invivoscientific.com). We attempted to humidify the environmental chamber to 60% by placing water baths on the isolation table, but the camera, robot, and microscope hardware would not tolerate the prolonged exposure to moisture. ImagePro Plus software from Media Cybernetics, Inc. (Rockville, MD) was used to write customized scripts that carried out all aspects of the hardware control and integration. The full list of second generation automated microscope system hardware and software is listed in Table 3.

Table 3. Second Generation Automated Microscope Components
Nikon TE-2000 inverted epifluorescence microscope
Sutter Instruments Lamda-XL light source
Sutter Instruments Lamda 10-3 controller
Chroma ET Filter Sets
Andor Clara 16/14-bit super-cooled CCD
Vincent brightfield shutter
Applied Scientific Instruments (ASI) MS-2000 Stage
ASI linear encoders
Nikon Perfect Focus System (PFS)
Peak Robotics KiNEDx 4 axis robot
Peak Robotics 24 stack plate holder
In Vivo Technologies environmental chamber
Nikon Plan Fluor ELWD 20X 0.45 NA Objective
Nikon Plan Fluor ELWD 40X 0.60 NA Objective
ImagePro Plus Control Software

Selecting Assay Plates

The first generation microscope was designed to work with 24-well plates. We built the second generation system with increased flexibility so that images could be captured from either 24-well or 96-well microtiter plates. The improved capability to image 96-well plates was necessary for conducting drug screens and siRNA screens that our lab was planning to carry out. We tested a number of different multi-well cell culture plates (Table 4) for their compatibility with Nikon's

perfect focus system (PFS) and evaluated them based on cell survival, robustness of focus, media loss, and cost. To assess survival, primary mouse neurons were cultured on day in vitro (DIV) 0 and then longitudinally imaged on DIV3, 10, 20, 30 and 40. The surviving cells were counted in each well and a mean and standard deviation (SD) was calculated for each plate. These statistics were plotted against DIV and compared to our control plate. There was significantly more toxicity in plates 2, 3, 5, 9 and 11. We next tested how focused the cells were in each well across the entire plate. At each DIV that images were obtained, we counted the number of wells that were in sharp focus by eye. Again, we plotted the number of focused wells against DIV and determined that the best performing plates (8, 9, 10, 11) typically had 95/96 (~99%) of the wells in sharp focus. Lastly we tested media loss in the plates over time. This is a critical parameter for high-throughput applications because we wanted to avoid the extra time it would take to remove plates from the incubator to add media. We also noticed that adding media to the cells adversely affected their health, potentially due to mechanical stimulation (Charles et al., 1991) caused by the liquid flow or dilution of secreted growth factors in the existing media. When we compared the media loss between DIV0 and DIV40 by weighing the plates at each time point, similar loss was measured in all the plates. Of the tested plates that displayed similar or better survival than the control plate (Plates 1, 4, 6-8, 10, 12) and had 95/96 wells in sharp focus (Plates 8, 9, 10, 11), only plates 8 and 10 performed well in each category. Of these two, plate 8 from MidSci was substantially lower in cost because it is a plastic bottomed plate. We therefore chose this plate for all

future experiments and it still remains very robust across the many different assay conditions we have tested, including the culture and imaging of induced pluripotent stem (iPS) cells.

Table 4. Microtiter Plate Testing	Catalogue
1. Corning 96-well pre-coated with PDL	3372
2. BD BioCoat 96-well pre-coated with PDL	354640
3. BD BioCoat 96-well pre-coated with PDL-L	354596
4. Nunc MicroWell pre-coated with PDL	152039
5. Corning Special Optics 96-well	CLS3614
6. BD Optilux 96-well	353948
7. Nunc Optical Bottom 96-well	165305
8. Midsci 96-well	TP92096
9. Nunc 96-well Coverglass bottom	265300
10. Matek 96-well glass bottom without PDL	PG96G-1.5-5-F
11. Matek 96-well glass bottom with PDL	PG96G-1.5-5-F
12. IBIDI 96-well u-plate	89626

Customized Script for Automated Image Acquisition

We chose Media Cybernetics ImagePro Plus software to control our image acquisition. Compared to Molecular Devices Metamorph software (Sunnyvale, CA), which was employed in the first generation microscope, ImagePro Plus provided a more flexible scripting language based on Visual Basic. This allowed us to more clearly expose user-defined parameters in the script header that provided a level of customization that we were not able to obtain with Metamorph. We additionally had more direct control over the hardware, allowing us to engage and disengage the PFS between wells and communicate with non-microscope hardware, such as the robotic arm, through serial I/O commands. Table 5 lists the parameters used to customize each plate acquisition. At the beginning of each experiment, the robotic arm loads a 96-well plate from the input stack of the plate stacker and places it within the plate holder of the stage.

The servo is then engaged to lock the plate against the plate holder walls, and the microscope moves to the approximate location of a fiduciary mark along the x, y, and z axes of the stage coordinate system. As in the first generation system, the fiduciary mark is a fixed point on the plate that defines a local origin

Table 5. Acquisition Parameters	Description
X_INTERWELL_DIST_24W = 18.6	X Distance in mm between wells (24 well)
Y_INTERWELL_DIST_24W = 18.6	Y Distance in mm between wells (24 well)
X_INTERWELL_DIST = 9.0	X Distance in mm between wells (96 well)
Y_INTERWELL_DIST = 9.0	Y Distance in mm between wells (96 well)
X_WELL_OFFSET = 0	Column offset for first well to image
Y_WELL_OFFSET = 0	Row offset for first well to image
NUM_COL_24WELL = 6	Number of columns to image (24 well)
NUM_ROW_24WELL = 4	Number of rows to image (24 well)
NUM_COL_96WELL = 12	Number of columns to image (96 well)
NUM_ROW_96WELL = 8	Number of rows to image (96 well)
HEIGHT_PIXELS = 1040	CCD pixels height
WIDTH_PIXELS = 1392	CCD pixels width
MONTAGE_OVERLAP_PIXELS = 75	Pixel overlap in adjacent images
IS_LOOP = 0	Loop plate for continuous timelapse
TURRET_POS = 0	Position of polychroic within wheel
OBJECTIVE_POS = 2	Position of objective 2=20X 3=40X
NUM_TILES_Y = 3	Number of images along Y axis of grid (n)
NUM_TILES_X = 3	Number of images along X axis of grid (m)
EXP_FILE As String = "..\ANDOR_1000MS_EXP.vpf"	Full extension of exposure file defined in IPP
WAVELENGTHFLAG = 1 or 0	Choose imaging wavelengths (i.e. BFPFLAG, CFPFLAG, GFPFLAG, etc.)

for the (x, y) coordinates of each image(Arrasate and Finkbeiner, 2005). At subsequent imaging time points, the fiduciary mark is captured again and the x and y coordinate shift is calculated by phase correlation, a method that is computationally efficient and robust for registering images with time varying, non-uniform illumination(Zitova and Flusser, 2003). The stage is then moved to correct for the translational offset and the coordinates are stored as a zero reference frame for all subsequent movements. Within each well of a multi-well plate, the script accesses the user-defined acquisition parameters to acquire an *n*

x *m* grid of images using multiple wavelengths of light to match the fluorophores that are present in the sample (Figure 4). The stage movements are calculated to leave a 75 pixel overlap between contiguous images. This overlap is sufficient for post-processing to stitch the images together despite small discrepancies between the theoretical and actual coordinates of the images within the grid. At the end of the image acquisition for a single well, the PFS is disengaged so that it is not perturbed by the discontinuities in the optical feedback that occur during interwell movements. Once at the center of the next well, the same program is executed. The program can be configured to define acquisition parameters on a per well basis such that a truly independent experiment with different fluorophores can be carried out in each well of the plate. Once images have been captured from the entire plate, the stage is instructed to return to the robot loading and unloading position and the robot returns the plate to the output stack of the plate stacker. The program is repeated for each new plate that needs to be imaged. The full code is provided in Appendix 6.
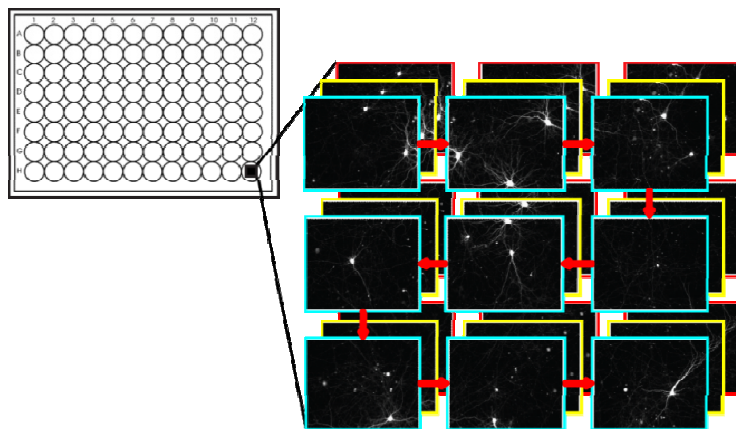
Figure 4. Multi-channel Acquisition. The diagram represents an automated image acquisition for a single well with three separated wavelengths of light. A

typical 3x3 grid of contiguous images are captured by precise stage movements. The movements are programmed to leave a 75 pixel overlaps, which is then used to correct small differences between the camera and stage axes and precisely stitch the individual images together into a large montage. The images are acquired in a snake pattern to minimize distance traveled.

Image storage and retrieval

Storing high-resolution images from automated microscope data sets offers significant challenges because the file sizes are large (Megapixel CCDs with 12–16 bit depth can result in megabytes worth of data for each image), and thousands of images can be acquired from a single 96-well plate. Multichannel, longitudinal acquisitions therefore result in tens of gigabytes of raw image data for each plate and terabytes for full screens. The time spent transferring data from acquisition hardware to servers can be lengthy. If errors occur, data can be lost.

We considered two general approaches to organize images. For relatively simple datasets, a hierarchical folder structure can be saved on a file server with a root folder for each experiment and subfolders if the experiment consists of multiple plates of data. All raw images from a single plate are stored within the same folder. Each image file name has descriptors so individual images are unambiguously placed in the appropriate folder and analysis programs can parse the image filenames and logically group them. For our longitudinal experiments, we chose to embed the date, a unique plate identifier, time point, well, montage

index, and fluorescence channel into the filename separated by underscores (i.e. PID20130704_mHTTHSR_T1_24_A1_1_RFP). Ideally, a more detailed description of each image is contained in the image metadata to allow other viewers to understand exactly what is contained in the image and how it was acquired. Although admirable efforts are being made to standardize image formats and metadata(Linkert et al., 2010), adoption of these standards by automated imaging platforms will likely take time. The second approach involves a relational database. Databases are optimal for storing data from larger screens and are the preferred method for labs with the resources to create and manage them. The up-front cost of time and money is greater, but they offer advantages for querying information, grouping data across multiple experiments, and carrying out retrospective analyses for secondary endpoints. Multiple open source database management programs are available. The most popular are based on the MySQL or PostgreSQL specifications. OMERO (Open Microscope Environment Remote Objects) is a combined client-server platform based on PostgreSQL that can be used for image visualization, management, and analysis(Allan et al., 2012). It is an easy to implement data management solution for labs that want the advantages of a database but do not want to develop one on their own, however, we found the image uploads to be prohibitively more slow than uploads directly to our local fileshare. OMERO has been upgraded since our last testing and we are now considering adoption of the platform as a way to expand our search capabilities and share data with collaborators.

Finally, raw image files can be stored in a hierarchical folder structure, and analysis programs can extract information from these images and save the resulting data into a database. In this approach, the images are not directly contained in the database, but fields within the database can point to the locations of the images on the server. We use Accelrys Pipeline Pilot (San Diego, CA), a commercial data management program, to facilitate easy reading, writing, and analysis of images from our local servers.

Whatever method of storage and retrieval is chosen, there should be a clear vision of how the data relate to each other and what the most intuitive overarching structure is for containing the data. In longitudinal experiments where we track individual neurons over time, we use a data schema represented in Figure 5. Once a database is created that is adequately flexible to store the results from of a large number of experiments, data mining programs can compare data across experiments, generate hypotheses, and even retrospectively test these hypotheses with existing data.
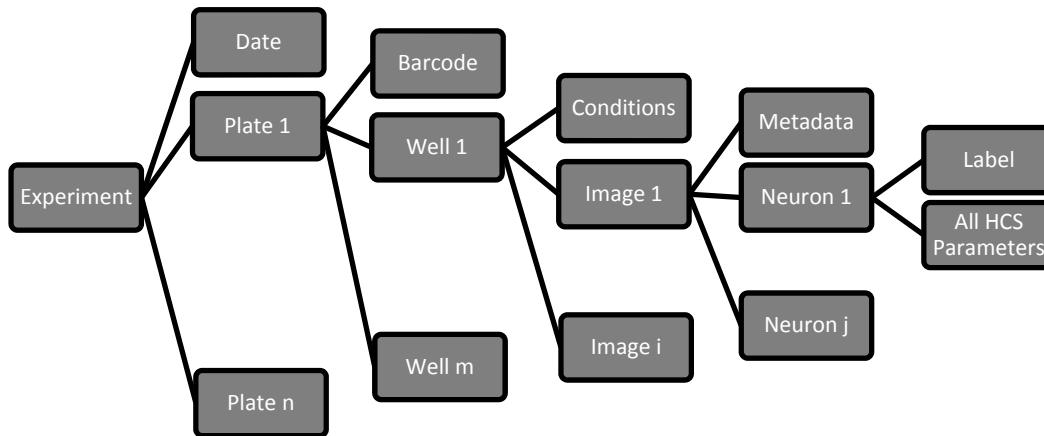
Figure 5. Data schema for storing information. Each experiment is composed of *n* plates that are imaged at a number of different time points. Each plate has a unique barcode that is incorporated into the filenames so that they can be unambiguously traced back to a specific experiment. The plates are composed of *m* number of wells on the plate (e.g. 96 or 384) that each have their associated conditions (e.g. culture medium, plasmids, drugs, cell type, etc.) and set of images. The images have all the stored metadata (e.g. filter positions, exposure time, calibration, and acquisition date/time) and list of neurons. Lastly, each neuron has a label and set of extracted parameters once the analysis is completed.

Image Analysis

A needs assessment. With the rapid advancement of our high-throughput image acquisition capabilities, we soon overwhelmed our ability to manually analyze the data as had been done with the first generation system. Image analysis became

the major bottleneck in our overall workflow. For example, a plate of data with a 3x3 grid of single fluorescence channel images could now be processed in under an hour on the second generation system. This would result in ~50 neurons per well or ~5,000 neurons per plate. For longitudinal experiments, we image once a day over the course of a week, which would easily result in >20,000 neurons to detect and extract information from. In high-throughput screens that capture from multiple fluorescence channels and image over 10 plates a day, the number of measurements that would need to be made approaches 500,000 in a single week, in addition to the overhead it would take to manually open each image and save the results. We therefore developed a customized, server-side, automated image analysis pipeline to (1) longitudinally track single neurons, (2) identify naturally occurring events over the course of their lifetime, and (3) detect endpoints of interest such as cell death or other binary outcome measures. In this way, we had all the necessary information to form powerful statistical models that relate a particular intermediate change of a neuron to its ultimate fate(Arrasate et al., 2004; Mitra et al., 2009; Miller et al., 2010b). The pipeline contains pre-processing steps that correct for CCD dark currents (dark field correction) and inhomogeneities in illumination (flat field correction) as well as perform contrast enhancement and smoothing. The analysis then identifies objects (cell segmention) and relates objects at one time point to objects in adjacent time points (cell tracking). Lastly, the analysis uses the tracking data to extract intensity and morphological parameters from single cells over the duration of the experiment. The analysis is modular and flexible so the user can carry out

steps separately or skip steps such as background correction that they don't want to include in the analysis (Figure 6).

Background Correction. In the first step of the imaging pipeline, the user points the program to a root folder containing all the raw images of the experiment. If "Background Subtract" is selected, images are opened and the filenames are parsed by the underscore character to obtain the plate ID consisting of the date and experiment descriptor, time point, and fluorescence channel. This grouping is based on our knowledge that variations in microscope field illumination result from variations in the lamp intensity, which can change throughout a long multi-day experiment. In addition, each fluorescence channel has a unique background signature that is related to the amount of autofluoresence emitted at that wavelength
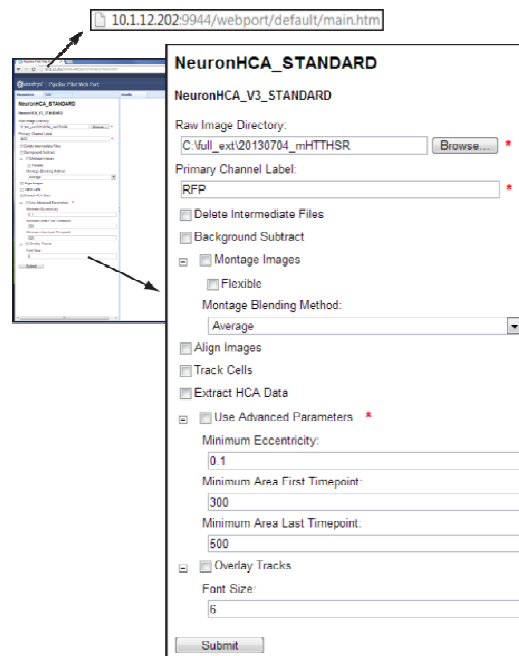
Figure 6. Start Page of Analysis Pipeline. The analysis is set up to run on a remote server. The server is accessed through a browser window where the user chooses a number of modular steps to perform within the analysis pipeline from the dialogue box. This modularity is important in situations where the user wants to rerun steps (e.g. Extract HCA Data) with different analysis parameters or when only a single step of the pipeline needs to be performed. To start an analysis, the user defines a root directory where all images of the multi-channel, longitudinal dataset are saved. The cell marker channel is defined, which must match the channel specified in the image filenames, and the user checks all the steps to perform. Within the "Montage Images" submenu, a blending method can be specified to tell the program how to calculate pixel values in the overlap region. "Advanced Parameters" give the user more control over cell segmentation during the data extraction module. The "Overlay Tracks" module produces a low resolution file with the segmented regions of interest (ROI) overlaid onto the cell marker channel.

(Aubin, 1979; Lu et al., 2010; Hawkins and Yager, 2003). We therefore calculate a background image for each fluorescence channel and each time point. For example, in a seven day experiment with two fluorescence channels, there would be fourteen total background images. In order to calculate these backgrounds, we take advantage of the structure of our images. Each image usually consists of a few neurons or bright objects per field and mostly dark pixels containing information about illumination variance across the field and autofluoresence. We

rely on this sparse object structure because there is very little chance that a pixel

will contain signal (e.g. intensity that does not represent the background) in more

than 50% of the analyzed images. After grouping the images, we calculate the

median intensity at each pixel. The resulting median value background image is

an image with the same pixel dimensions as the input images, but the pixel

values are the median intensities of the combined image set. We find that this

background correction method increases the signal to noise ratio (SNR) in our

images (Figure 7), calculated by $SNR_{image} = \frac{(\mu_{sg} - \mu_{bg})}{\sigma_{bg}}$, where μ_{sg} is the average

signal, μ_{bg} is the average background, and σ_{bg} is the standard deviation of the

background.
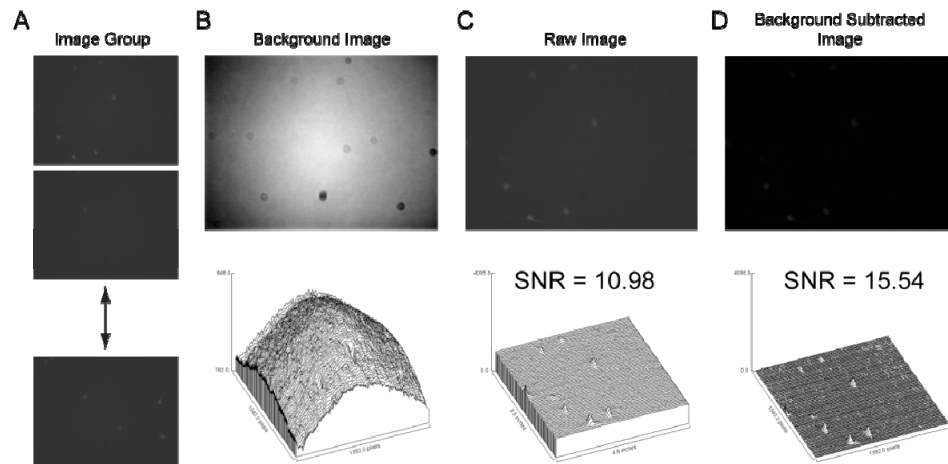
Figure 7. Median Value Background Correction. (A) All images are opened,

grouped by time point and channel, and placed into an image stack. (B) For each

time point and channel, a single background image is generated by calculating

the median value at each pixel within the stack. When contrasted to see small

changes in pixel value, dust and illumination inhomogeneities are observed. (C

and D) The SNR of a representative raw image with low signal can be increased by ~50% through background correction.

Stitching. The next step in the analysis pipeline is to take the individual images from a well and stitch them together to make a single montage image (Figure 8). This step reconstructs long neurites that originate from a single neuron, but often extend across many fields of view within a well and are cropped in single images. It also enables more complex measurements, such as cell non-autonomous interactions, because the spatial relationship of a much larger number of neurons is preserved. The filenames of the background corrected images are first parsed to determine the plate, time point, well, and fluorescence channel the image represents. The images are grouped according to these parameters and processed with the ImageJ Stitching_.jar plugin(Preibisch et al., 2009). The plugin uses the phase correlation method to calculate translational offsets between all images in the image set and then globally optimizes the sum of translations to find an absolute minimum. The plugin requires the original starting coordinates (in pixels) of the images within the larger montage. These coordinates are dependent on the exact movement pattern used to acquire the images, image size and orientation of the CCD with respect to the axes of the stage. The stitching algorithm needs to be flexible enough to process images after hardware and software upgrades or acquired on different automated microscope systems. Based on the particular hardware and acquisition software configuration, the image coordinates are calculated and a text file is created with the full extensions to the images within the montage followed by the starting

coordinates of each image (Appendix 3). The stitching is prone to error if there is insufficient pixel information in the images, which often happens when there is a low intensity signal. We take the approach in our experiments to always co-express a cell marker composed of a fluorescent protein that is not fused to any other protein and is small enough to diffuse in and out of the nuclear and cytoplasmic cellular compartments. We use the cell marker channel to compute image locations within the montage and then propagate the results to all other fluorescence channels. This ensures robust placement of images irrespective of signal strength and forces all channels to have the same placement, which is critical for the data extraction steps of the analysis.
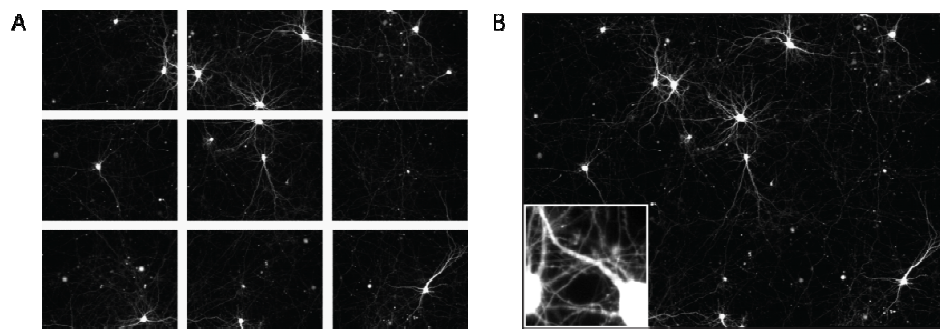
Figure 8. Image Stitching. The individual images captured in each well are stitched together to form a single large montage image. (A) Example of a 3x3 grid of images with a 75 pixel overlap from the second generation automated microscope. (B) Result of the stitching. Inset shows a magnification of the seam between the top-left and top-center images with near perfect preservation of pixel values and location.

Alignment. Once the montages are constructed for each time point, we carry out another step to remove any small shifts in the montage images that occur from

one time point to the next. Although we make great effort to register the plate to the first time point during acquisition, the alignment step during analysis provides a second chance to further refine the registration within each well. This is necessary because small stage drifts and rotational displacements of the plate within the plate holder cannot be corrected for during acquisition. Since downstream neuron tracking steps rely on alignments within 20 μm, about the width of a neuron cell body, the software alignment is an essential step in our overall pipeline.

In the alignment step, the montage images are opened and grouped according to plate ID, well, and fluorescence channel. For each well, the montage images from all the time points of the cell marker channel are grouped together into a stack. This stack is passed into ImageJ and the StackReg_.jar plugin is called to align time point t_n to t_{n-1} starting with t_2(Thevenaz et al., 1998). The full rigid body transformation of the plate would take the form $\vec{x} = \begin{bmatrix} \cos\theta & -\sin\theta \\ \sin\theta & \cos\theta \end{bmatrix} \cdot \vec{u} + \Delta\vec{u}$, but for small angle displacement, the first term only becomes significant at large $\vec{u}$. At large $\vec{u}$, two closely spaced points on the plate (e.g. within the same well) are transformed approximately equal distances by the rotation. Therefore, in order to minimize computation time while still adjusting for the majority of the movement, we restrict the registration to only consider the simple case of translational movements. The registration parameters are of the form $\vec{x} = \vec{u} + \Delta\vec{u}$, where the algorithm solves for $\Delta\vec{u} = \begin{bmatrix} \Delta x \\ \Delta y \end{bmatrix}$. Convergence on $\Delta\vec{u}$ is based on minimizing the

integrated square difference in intensity values between the test image (t_n) and reference image (t_1)(Thevenaz et al., 1998).

Segmentation. Automated detection of neurons in our images has been a challenging design problem. Unlike immortalized cell lines that many groups use in their assays, we use primary neurons that express proteins from plasmids at lower levels. Consequently, our images typically have much lower SNRs than would be obtained with fixed cells or cell lines. Our survival assays also start longitudinal imaging on the day after transfection so that we can capture early, disease-related phenotypes. At this time, our neuronal populations show significant variation in the expression of the cell marker fluorescent protein. This makes it difficult for global thresholding approaches alone, which fail with high signal variances(Lee et al., 1990), to identify cell borders equally for both low and high expressing cells. To add to the segmentation difficulty, neurons have particularly complex morphologies, varying in soma size and shape and the number, width and length of neurites. Neurite segmentation is particularly challenging because there is very low SNR between the neurite and background and they extend over large areas of the image, in many cases across other bright objects such as neuron bodies and debris. One of the last major hurdles we faced was distinguishing live neurons from dead ones. We normally identify a dead cell by the loss of fluorescence of the cell marker(Arrasate et al., 2004). However, in many cases, as a neuron dies, a fluorescence signal persists in the form of an inhomogeneous clump of debris or can even remain as a round cell body devoid of neurites. These assay characteristics make cell segmentation the

most challenging step of the analysis, and we are currently working on more sophisticated multi-parametric segmentation algorithms that use combinations of cellular features to distinguish between live and dead cells. Nevertheless, we present a segmentation algorithm here that has worked effectively in many survival experiments in our lab and is extensively used for single experiments testing a handful of conditions and full screens testing hundreds of different compounds.

We always segment cells based on one of the fluorescence channels, referred to as the primary channel, and propagate the segmented regions to the remaining channels. In almost all cases, the cell marker channel is used for segmentation, but we do envision applications where markers for specific cellular compartments (e.g. nucleus) or organelles (e.g. mitochondria) could be used to complement the whole-cell analysis. We open aligned tiff stacks from this channel that have been background corrected at each time point and then pre-process the images to improve the performance of the segmentation (Figure 9). The first step in pre-processing is contrast enhancement. Within this component, 0.05% of the low value pixels are saturated to zero and 0.5% of the high value pixels are saturated to the maximum. Intermediate pixel values are linearly stretched to the new minimum and maximum values based on an 8-bit scale, corresponding to pixel values from 0 to 255. Next, a smoothing operation is performed to reduce noise in the image. A two-dimensional Gaussian(Nixon and Aguado, 2008) is convolved with the image to reduce high frequency information in the image according to $G(r) = \frac{1}{2\pi\sigma^2} e^{-\frac{r^2}{2\sigma^2}}$, where r is the kernel radius in pixels and σ is the

standard deviation of the Gaussian function. Mild smoothing in our images is achieved with a standard deviation equal to 3 and a kernel radius equal to three times the standard deviation, or 9 pixels. Finally, for pre-processing, a second step of image enhancement is performed to saturate the upper and lower pixels and map the image back to the original scale of a 12-bit image. The visual result of these three pre-processing operations is depicted in Figure 10.
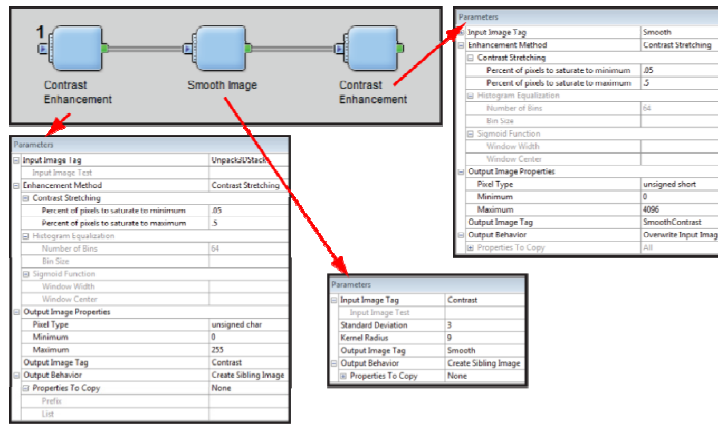
Figure 9. Image Pre-Processing. The diagram depicts the steps used to carry out the pre-processing along with the full list of parameters defining the contrast enhancement and Gaussian smoothing.

| Contrast Enhancement 1 | Gaussian Smoothing | Contrast Enhancement 2 |
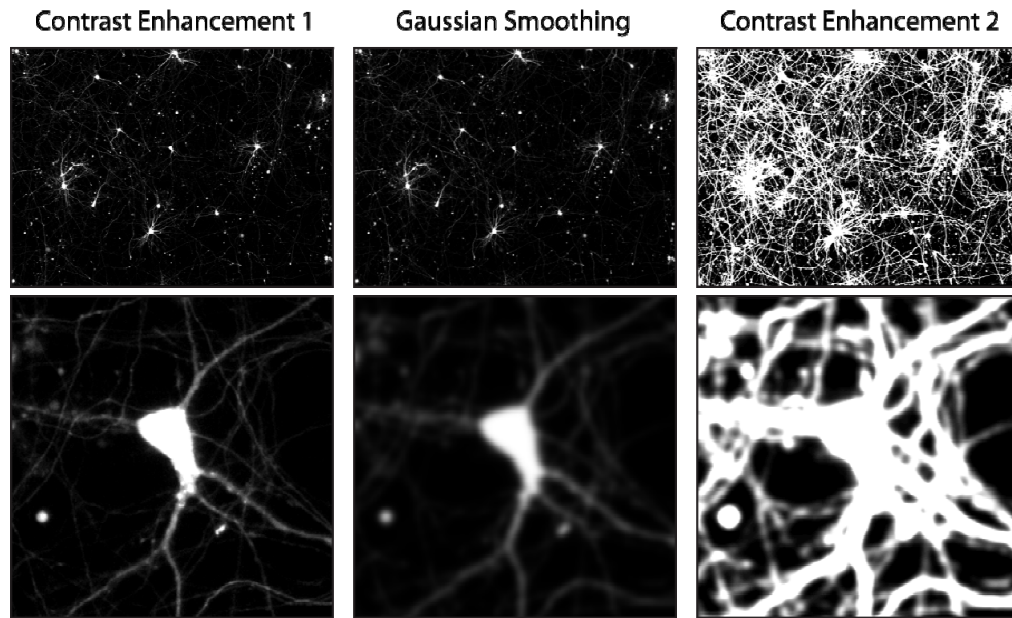
Figure 10. Image Pre-Processing Example. The entire montage image at each step is shown in the top panels, and a magnified region focused on a single neuron is shown in the bottom panels. Gaussian smoothing blurs the image to create a more homogeneous signal throughout the cell body. The second contrast enhancement is able to further separate bright and dark pixels in the image, making dim features, like neurites, brighter and easier to distinguish from the background.

After pre-processing, the image is segmented to distinguish bright objects from the background, and filtering is performed to remove objects that don't meet the criteria of a living neuron (Figures 11-12). First regional maxima or peaks are found in the image. In order to be a true maximum, the pixel intensity must fall within the upper 95 percentile of all pixel intensities in the image. A mask defining each maximum is then generated from all connected pixels to the maximum that have intensities within 2-3 units of the regional maximum. For example, if a

maximum is 200 in a particular region, a mask surrounding the maximum is formed from all connected pixels with intensities greater than or equal to 198. Once all maxima are identified, an opening function is performed on the masks to remove small or thin objects. When the objects are neurons, the opening function has the effect of confining the mask to the soma region and eliminating any long neurite projections. Opening is composed of two sequential operations, erosion and dilation. Each of these is performed with a radius of 5 pixels such that any objects smaller than 10 pixels wide will be completely removed. To further eliminate small masked regions, a user-defined area filter is applied. This filter has the effect of removing small debris within the image that are identified as maxima but are not the size of a living neuron. The user can specify a different size area filter at the first and last time points and the filter size for intermediate time points is linearly interpolated between the first and last. This flexibility is built in to the analysis because the mean neuron area in the cultures increases over time as the neurons mature. Despite significant optimization of the parameters of these segmentation steps, we found that some neurons would die leaving a rounded carcass behind instead of completely dispersing the cell marker fluorescence signal. In order filter out these dead cells, we added another filter based on eccentricity. The filter fits an ellipse to each object and measures the eccentricity of the fitted ellipse according to $e = \frac{c}{a}$, where c s the distance from the center of the ellipse to either foci and a is the length of the semimajor axis. The eccentricity of an ellipse must be $0 < e < 1$. In the limiting case of a circle, $e = 0$. The parameter for this filter is also user defined, but we have found that

values between 0.1 and 0.2 work best to discriminate living neurons with slightly

elongated morphologies from the round carcasses of dead neurons.
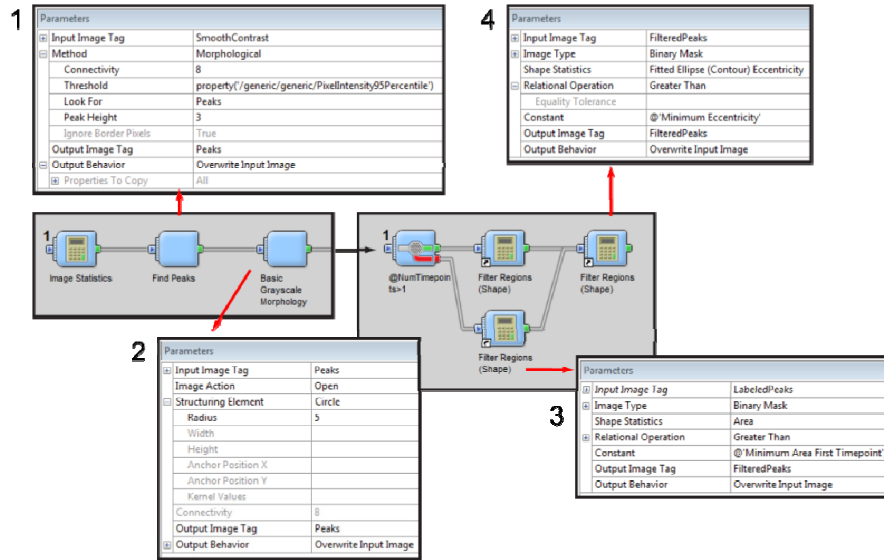
Figure 11. Parameters of the image segmentation pipeline. (1) Regional

maxima are identified in pre-processed images. The peak height can be adjusted

to optimize the mask filling the entire cell body. (2) An open function is performed

on the maxima, and objects are further filtered based on (3) minimum area and

(4) eccentricity criteria.
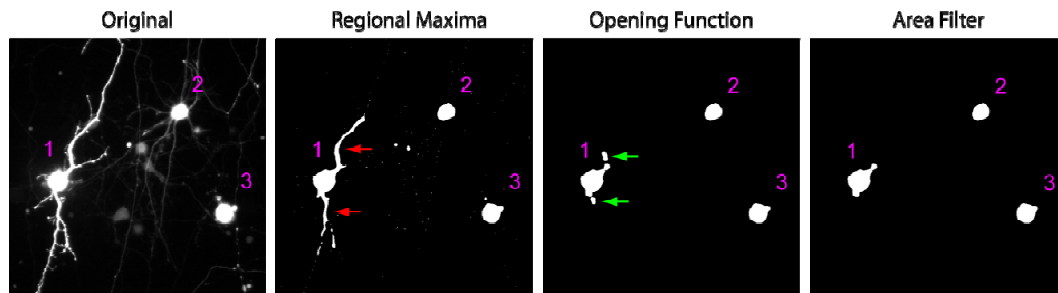
Figure 12. Example of Image Segmentation. One the original image is pre-

processed, masks are generated from the regional maxima identification. The

opening function removes the neurites from neuron 1 (red arrows) and small regional maxima from the background of the image. The area filter further removes small objects that do not correspond to living cells and over-segmentation resulting from the opening function (green arrows).

Tracking. At the end of segmentation, neurons are separately identified in each of the time points of the experiment. In each image, there exists a set of neurons, $N \in \{1,2,\ldots,n\}$, where each neuron is labeled in ascending order according to its $\{x,y\}$ coordinates. However, the set of neurons at each time point is different because neurons die as time progresses and others are newly identified by the segmentation pipeline as they begin to express the cell marker to an appreciable level. Tracking maps the set of neurons in the first time point (t_1) to the set of neurons in all subsequent time points $(t_2, t_3, \ldots, t_i)$ by sequentially changing the labels in t_i to match the labels of the same neurons in t_{i-1}. The result is a new set of neurons, $M \in \{1,2,\ldots,m\}$, that is unique and inclusive of all neurons identified throughout the entire duration of the experiment (Figure 13). Tracking preserves the longitudinal nature of the experiment and allows all parameters (e.g. death, inclusion body formation, intensity, texture, etc.) from an individual cell to be quantified as a function of time. The analysis pipeline uses the most conservative method for tracking, which requires a partial overlap of the segmented regions between adjacent time points. If a neuron in t_i overlaps with a neuron in t_{i-1}, then the label in t_i is changed to the label corresponding to the overlapping neuron in t_{i-1}. This is carried out for the set of all neurons in t_i. If any neuron is unmatched, meaning there is no overlap with the neurons in t_{i-1}, then

the label is changed to the next highest integer in $M \in \{1, 2, \dots, m\}$. The overlap method works well for our applications because the primary neurons used in our cultures do not move significantly within 24 hours, which is our standard imaging period, and the cells do not divide. Tracking cells based on nearest neighbor can confound our experiments because as cells die, they may be incorrectly matched to newly identified, nearby cells that are just beginning to express the cell marker. In the future, we would like to implement more complex algorithms for cell tracking based on optimal matching of cell morphological and intensity features along with trajectory fitting(Harder et al., 2009). Despite the development of methods for time-resolved single cell tracking in low throughput microscopy(Rabut and Ellenberg, 2004), the methods have only recently been adapted to large-scale datasets(Harder et al., 2009; Chen et al., 2006). In these large-scale datasets, the tracking problem is more difficult because global optimization often leads to ambiguous matching based on overlapping feature sets(Meijering et al., 2006). Local optimization performs better, but the features to optimize (e.g. nearest neighbor, cell size, cell marker intensity) need to be determined in an assay-dependent manner. The most feasible next step to improve our tracking would be to match neurons based on nearest neighbor, but only permit matches between neurons if the distance between them is less than a user-defined threshold. The user would define a maximum velocity parameter that would restrict movements to a maximum distance within the imaging period. In order to prevent incorrect matching to newly expressing neurons, a further

step could restrict matches to objects with the same or greater intensity of the cell marker.
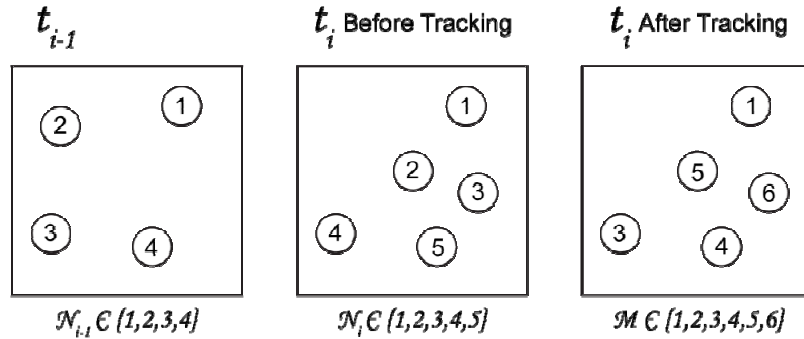
Figure 13. Schematic of tracking algorithm. At time point t_i, objects 1, 4, and 5 overlap with objects 1, 3, and 4 in time point t_{i-1} respectively. The labels are changed to match the existing labels at t_{i-1}. Objects 2 and 3 do not have any overlapping regions and are therefore labeled with the next highest integers in $\in M$. The tracking algorithm code is provided in the Appendix 4.

Feature Extraction. Tracking results in a set of labeled masks that have been linked through successive imaging time point so that individual neurons have the same, unique label over their entire lifetime (Figure 14). The masks outline the neuronal region corresponding to cell body or soma and are applied to each captured wavelength to extract potentially hundreds of different parameters from the underlying pixel locations and values of the multi-channel acquisition (Figure 15). As a starting point, we chose a basic set of parameters that we hypothesized would be useful in defining and predicting disease phenotypes. For instance, Miller *et al* previously determined how the risk of neuronal death and inclusion body formation were highly dependent on the concentration of mutant huntingtin

(mHTT) within each cell(Arrasate et al., 2004; Miller et al., 2010a). We also postulated that inclusion body formation could be automatically detected by changes in pixel intensity variance of the fluorescent protein fused to mHTT. We therefore chose to extract a group of intensity parameters including pixel intensity mean, variance, and intensity order statistics. We further chose to extract a basic set of morphological parameters that we hypothesized would be useful in assessing cell health. The full list of parameters is shown in Table 6. Each parameter has a separate value for each wavelength of light that is captured during acquisition. The full set of multi-wavelength parameters are output in a flat format, easily portable spreadsheet. The data are grouped by plate and well for easy interpretation and visualization.

Statistical Analysis. The flat format spreadsheets generated from data extraction list objects along the rows and parameters along the columns. Because the data we obtain consists of longitudinal information for individual cells, we can use the same powerful statistic models that are employed in clinical trials to assess the outcomes of patients. Instead of getting baseline diagnostic information from patients, we instead measure multi-parametric fluorescence information from neurons and record endpoint phenotypes as they occur. Much as in a
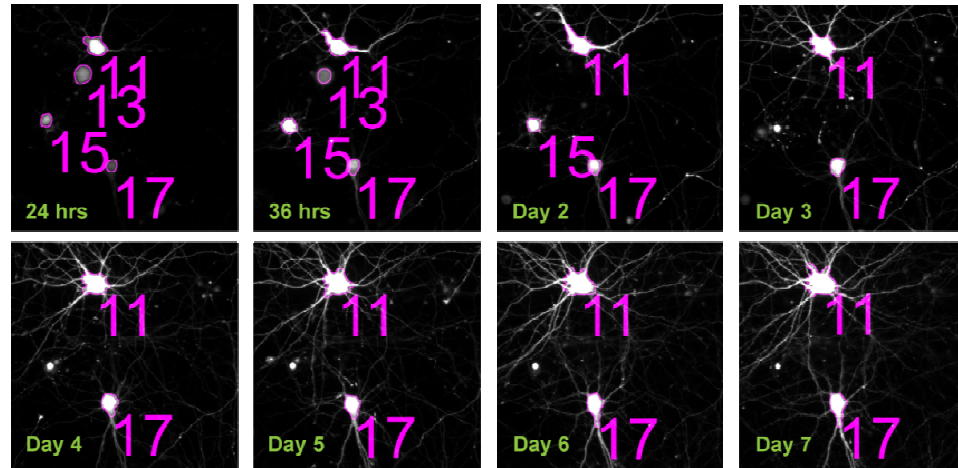
Figure 14. Result of segmentation and tracking. The panels represent a time course of a selected region of the cell marker channel for a 7 day longitudinal experiment. The images show detection of both bright and dim cells starting 24 hours after transfection with mApple as the cell marker and HTT^{586}-Q$_{17}$-EGFP. The accuracy of image alignment can be appreciated by almost no movement of cells throughout the time course. The ROIs accurately trace the borders of cell bodies and track them over 7 days by marking them with the correct label. Once the fluorescence signal of the cell marker completely disappears (Neuron 13 at Day 2) or becomes too small to be a living neuron (Neuron 15 at Day 3) the cell is no longer tracked and the label is removed. Because we use a left censoring convention(Moeschberger and Klein, 2003), the recorded time of death is the last time the cell is detected (e.g. 36 hours for Neuron 13 and Day 2 for Neuron 15).

Parameters Associated With The RFP Channel

Label	MeasurementTag	BlobArea	BlobCircularity	PixelIntensitySkewness
1	RFP	1283	1.065678729	-0.365909263
2	RFP	1111	1.112981326	-8.65E-02
3	RFP	1358	1.185078562	0.236693908
4	RFP	1810	1.266714792	-0.102581508
5	RFP	1041	1.024480524	0.312203977
6	RFP	1465	1.123640927	0.319429863
7	RFP	1197	1.243136002	0.410462087
8	RFP	2518	1.176461972	0.508261682
9	RFP	1763	0.661545922	0.626000999
10	RFP	1688	1.294679785	-0.229903712

More →

Parameters Associated With The GFP Channel

Label	MeasurementTag	BlobArea	BlobCircularity	PixelIntensitySkewness
1	GFP			0.662736264
2	GFP			-8.53E-02
3	GFP			0.545294407
4	GFP			-5.29E-02
5	GFP			1.72405243
6	GFP			0.314586135
7	GFP			0.321512354
8	GFP			0.489364561
9	GFP			0.445673943
10	GFP			-5.01E-02

More →

Figure 15. Multi-channel Extraction of Parameters. Once cells have been properly segmented and tracked, any number of morphological (shape), intensity (pixel magnitude and variance), and texture (combination of pixel intensity and local pattern) parameters can be extracted as a multi-parametric or phenotypic readout of a cell's instantaneous state. The mask is generated from segmentation of the mApple (RFP) channel and is then applied to the HTT (GFP) channel. Morphological parameters of the cell body (e.g. area and circularity) are only calculated for the RFP channel. All other parameters are calculated for both channels. The power of such phenotypic measurements is demonstrated by comparing the coefficient of variance, $C_v = \frac{\sigma}{\mu}$, between HTT[586]-Q[17]-EGFP and HTT[586]-Q[136]-EGFP when an inclusion body has formed. $C_v(Q_{17}) = \frac{63}{103} = 0.61$ and $C_v(Q_{136}) = \frac{3.5}{1.85} = 1.89$ or roughly 3 times the value of the Q[17] cell, showing that pixel information can be used to detect biologically relevant events.

Table 6. List of Parameters Extracted From The Cell Bodies
Object parameters
Plate, Well, Label
Shape parameters
Area, Perimeter, Circularity, Centroid
Intensity parameters
Channel or wavelength (e.g. BFP, GFP, RFP, etc.), Mean, Variance, Standard Deviation, Skewness, Kurtosis, Intensity Order Statistics (Minimum, Maximum, Intensity Percentiles, Interquartile Range)

prospective cohort study, cells, through stochastic diversification, manifest a wide range of traits or fluorescence readouts throughout their life, and retrospective analysis determines how significant these traits are in predicting cell fate. In this way, each neuron is likened to a patient for whom we have a comprehensive diagnostic panel of values. We wish to determine how well each value or parameter predicts a certain outcome measure of interest, for example neuron death, inclusion body formation, or any other bivariate endpoint phenotype. In order to do this, the data are fitted with a Cox Proportional Hazards (CPH) model(Moeschberger and Klein, 2003), a special type of statistical analysis used for time-to-event data. Multivariate CPH integrates a user-defined number of parameters (referred to as covariates in the CPH model) to generate a hazard function, which describes the risk of a certain cellular event taking place given that the cell has lived until that time. Each modeled risk x_i contributes exponentially to the overall hazard function $H(t)$ according to $H(t) = H_o(t)e^{(\beta_1 x_1 + \beta_2 x_2 + \cdots + \beta_i x_i)}$ and CPH assigns a weighting factor β_i to each risk based on how important it is in predicting the outcome or hazard of interest. A larger $\beta_i x_i$ indicates a greater overall importance of the risk factor within the model.

Automated Acquisition and Analysis for Screening Applications: Brain-Derived Neurotrophic Factor (BDNF) As a Positive Control

We needed a disease model and positive control to test the ability of the fully automated system to detect disease modifiers within an assay that simulated a screen. Our lab had already developed a murine primary neuron model of HD based on expression of an exon 1 fragment of the full length huntingtin gene. The strength of the model is evident by its ability to recapitulate 12 known features of the disease in humans and predict other HD related phenotypes later observed in murine models or humans with HD(Miller et al., 2010a). BDNF is a pro-survival factor produced by cortical neurons in the brain and delivered to the striatum through corticostriatal projections(Altar et al., 1997). BDNF is an important trophic factor for promoting both striatal and cortical cell survival synaptic function under normal physiological conditions and when coping with disease(Ghosh et al., 1994; Baquet et al., 2004; Lu, 2003; Zuccato et al., 2001). This is the particularly true in HD because HTT has a direct role in both stimulating BDNF expression through cytosolic sequestration of the repressor element-1 transcription factor (REST) (Zuccato et al., 2001; Zuccato et al., 2003) and promoting axonal anterograde transport(Gauthier et al., 2004). Abnormally expanded HTT interferes with both of these processes to decrease trophic support to striatal and cortical cells, and augmenting BDNF levels has been shown to protect neurons *in vitro* and *in vivo* from the toxic effects of mHTT(Saudou et al., 1998; Simmons et al., 2009).

We received a highly active recombinant form of BDNF from Amgen and used it in our automated system to test our ability to detect HD modifiers with high sensitivity and specificity. We decided to use cultured cortical neurons because the cortex is an affected brain region early in HD(Nopoulos et al., 2010), and we wanted to use a cell type where we would be able to easily obtain large amounts of tissue to test the thousands of different conditions present in high-throughput screens. Primary cortical cultures were prepared from mouse embryos at embryonic day E17-18. The cells were cultured in 96-well TPP microtiter plates (TP92096) that had been pre-coated with poly-D-lysine. At day *in vitro* 4 (DIV4), the cultures were transfected with mCherry as a cell marker and either HTT^{exon1}-Q_{17}-EGFP or HTT^{exon1}-Q_{97}-EGFP according to the plate formats depicted in Figure 16. The expression plasmids were diluted and mixed with Lipofectamine 2000 and added dropwise to the cells. The transfection mixture was then aspirated after a 3 hour incubation period at 37°C, washed with Neurobasal® Medium, and cultured again in 50% conditioned growth medium (Sharma et al., 2012). At this time, BDNF was added to a subset of the wells. We used two different plate formats with replicate conditions in order to pool the data from two wells and make sure the data were not a result of a systematic bias arising from plate location. 24 hours after transfection, the two plates were subjected to longitudinal imaging, where they were placed in our automated microscope and imaged in the RFP channel. The plates were repeatedly imaged once every 24 hours for a week. We then used our automated image analysis to track neurons over time and determine time of death as described in the previous section. CPH

models were fitted to the data from each well and we assessed our ability to identify a known modifier of mHTT toxicity from all 80 tested conditions. Using p<0.05 for significance, 10/12 BDNF wells were identified as true positives and 2/12 were missed as false negatives (Figure 17). In addition, test well 70 was identified as a false positive. From these data we determined the positive predictive value (PPV) of a hit in our simulated screen and the negative predictive value (NPV) of a non-hit. The PPV is calculated by $PPV = \frac{\#True\ Positives}{\#True\ Positives + \#False\ Positives}$. From the BDNF data, PPV = 10/(10+1) = 90.9%. NPV is calculated by $PPV = \frac{\#True\ Negatives}{\#True\ Negatives + \#False\ Negatives}$. The corresponding NPV is therefore NPV= 67/(67+2) = 97.1%. Given a hit in our screen, we therefore have a 90% chance that it is a true hit. Likewise, given a well that is not a hit, we have a 97% chance that the well is indeed not a hit. These encouraging results demonstrated the power of the automated acquisition and analysis pipelines, with minimal user intervention, to collect and analyze data with a sensitivity and specificity that was sufficient to reliably identify a known modifier of mHTT toxicity.

Figure 16. BDNF Plate Formats Used to Simulate A Screen for Modifiers of mHTT Toxicity. Replicate plates with different well locations for BDNF. In plate formats 1 and 2, the 16 black wells are controls (split between either EGFP alone or EGFP + BDNF) and all remaining wells are the HTT^{exon1}-Q$_{97}$-EGFP test wells numbered 1-80. The tan colored test wells are where 5, 50, or 500 ng of BDNF have been added to HTT^{exon1}-Q$_{97}$-EGFP in order to simulate possible modifiers of mHTT toxicity. The wells without BDNF simulate modifiers with no affect. The corresponding heat map shows the cumulative hazard for cell death in each well at the end of the seven day experiment. Red indicates high hazard and white indicates low hazard.
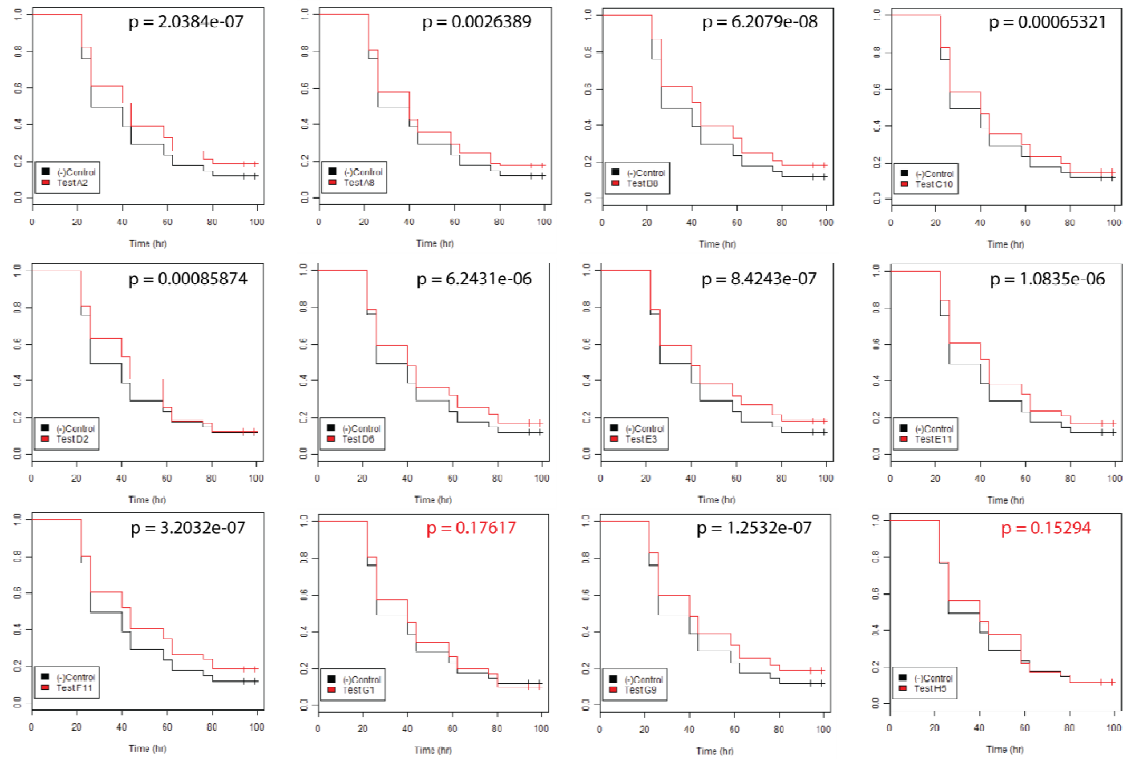
Figure 17. Individual Well Survival Curves and Statistics for BDNF. Kaplan-Meier survival curves for the test wells with HTT^{exon1}-Q_{97}-EGFP + BDNF. The red curves represent the combined survival from duplicate BDNF wells in the two different plate formats. These curves are compared to the black curve representing the plate background, or estimated survival of unmodified HTT^{exon1}-Q_{97}-EGFP. This black curve is the same on each plot and is derived from the survival of all the test wells combined, irrespective of BDNF addition. The presumption is that the prevalence of modifiers will be low within all tested conditions. Abrogation of mHTT toxicity is visualized by a less steep drop-off of the red survival curve compared to the black curve over time. For each well, a CPH model was fit to the data comprising the two survival curves with condition (test well vs. combined background) as the covariate. P-values are for significance of the coefficient associated with the condition covariate in the CPH

model. For BDNF modification of mHTT toxicity, 0.05 was used as an arbitrary criterion for statistical significance.

Validation of Automated Image Analysis

As a second validation of the automated system, we compared the survival curves and CPH models of data analyzed with and without manual editing of the survival tracks. Primary rat neurons were cultured in a 96-well plate as previously described and transfected with a cell marker along with either empty vector or α-synuclein. The plates were subjected to automated longitudinal imaging in the RFP channel for seven days and the resulting image sets were submitted for automated analysis. Statistical analysis was either carried out on the raw data file or a version of the file that was manually procured by a trained user. Manual procurement involved viewing direct output of neuron tracks from the automated analysis pipeline and correcting the tracks for proper cell identification and time of death. Objects not considered living neurons were removed from the analysis, and tracks with incorrect time of death were adjusted to the correct time. Figure 18 shows that the original raw data file produced the same effect as the manually procured data. The magnitude of the cumulative hazard changed, but the divergence of the two curves was preserved. This is reflected in almost identical hazard ratios between α-synuclein and empty vector control in the two cases.
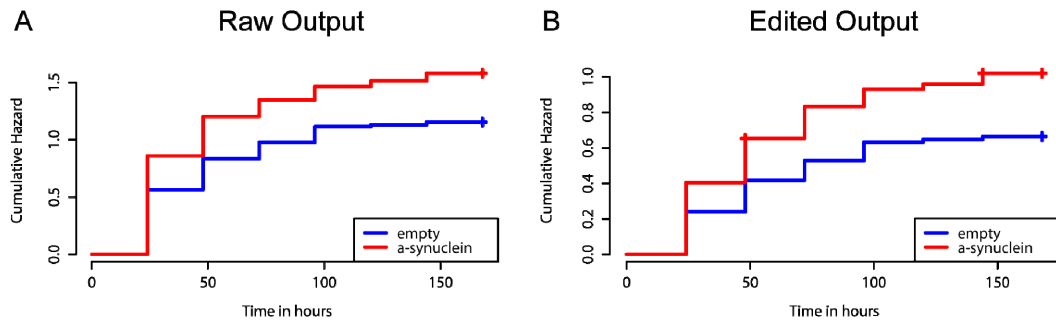
Figure 18. Validation of Automated Analysis. (A) Survival plot generated from the raw output of the automated image analysis. Coefficient for a-synuclein=0.337, HR=1.40, p_{coef}=2.5e-8*** (B) Survival plot generated after procurement of the tracks output by the automated analysis. Coefficient for a-synuclein=0.438, HR=1.55, p_{coef}=8.79e-4***.

Chapter 4

Huntington's Disease as a Disease of Protein Conformation

Huntington's Disease (HD). HD is a devastating neurological disorder that typically begins in the third to fourth generation of life and manifests as progressive cognitive, psychiatric, and motor dysfunction. A slow but persistent decline in function follows symptom onset, and within about 20 years, the disease leads to an inevitable decline to full disability and death(Francis, 2007). Chorea, the classic motor symptom associated with HD, is characterized by involuntary writhing, dance-like movements that cause the patient to be in a perpetual state of motion(Huntington, 2004). Severely affected individuals contract a juvenile form of the disease that is marked by bradykinesia, tremors, and convulsive seizures instead of chorea(Jervis, 1963). Although motor symptoms are the most stereotyped and striking feature of the disease, families describe the psychiatric symptoms of HD that include depression, anxiety and personality change as the most troubling. Unfortunately, these psychiatric symptoms can be the earliest signs of disease, and families must endure the ensuing emotional stress over a particularly long period of time(Duff et al., 2007; Paulsen et al., 2006). Individuals with HD may display symptoms on one end of the phenotypic spectrum, for instance, primarily choreic motor dysfunction or primarily cognitive and psychiatric dysfunction. Some patients may never even display motor symptoms, making their diagnosis a challenge and often overlooked without a positive family history. These variations in phenotype may reflect differences in the genetic background accompanying the mutant protein,

particularly because specific phenotypes can track within families. Although the clinical presentation of HD was first described over a century ago and the genetic cause of HD has been known for twenty years, there are still surprisingly few pharmacological options for patients, even for symptomatic relief, and there are no disease modifying therapies.

Genetic Basis of Huntington's Disease (HD). HD is a heritable, autosommal dominant, neurodegenerative disorder that profoundly affects nervous system function. Neurodegeneration results from an expanded $(CAG)_n$ repeat within the normally polymorphic *IT15* gene on chromosome 4(MacDonald et al., 1993). The $(CAG)_n$ expansion encodes an N-terminal polyglutamine (polyQ) stretch in the huntingtin protein. When the number of repeats exceeds a threshold of 40, the mutation is fully penetrant and sufficient to cause disease(Duyao et al., 1993; Andrew et al., 1993). Disease does not occur when the number of repeats is below 36 and is believed to be incompletely penetrant between 36 and 40. Long repeat lengths, typically over 60, cause a severe, juvenile form of the disease, which can present as early as 2 years old(MacDonald et al., 1993). The age of onset (AO) in HD follows an inverse exponential relationship when plotted against the length of the $(CAG)_n$ repeat. Taken as a whole, the repeat length describes roughly 70% of the AO variability. However, due to significant spread in the data at the most common repeat lengths between 40 and 50 (inclusive of 90% of HD cases worldwide), repeat length could only describe 44% of AO variability. Interesting, the majority (59%) of the residual variability in AO could be ascribed to genetic or shared environmental factors, making a strong case for as

yet to be described genetic modifiers of the disease(Wexler, 2012). The prevelance of HD in white populations is approximately 5-7 per 100,000 individuals. The prevalence in Asian and African populations is significantly less due to a lower frequency of mutant alleles. HD is part of a broader class of 16 known trinucleotide repeat disorders, 9 of which may ultimately share common gain-of-function pathological mechanisms(Orr and Zoghbi, 2007).

Huntingtin Protein and Disease. The Huntingtin (HTT) protein is a large, 350 kD protein that is expressed ubiquitously throughout the body and is required for normal embryonic development(Zeitlin et al., 1995). It is likely involved in numerous cellular processes, including endocytosis and endosomal motility, transcriptional regulation, axonal transport, nuclear-cytoplasmic shuttling, synaptic transmission and preventing apoptosis(Cattaneo et al., 2005). HTT consists of a 17 amino acid N-terminal domain that precedes the polyQ tract. The polyQ region is immediately followed by a proline-rich region that stabilizes the polyQ tract and decreases its propensity to misfold(Bhattacharyya et al., 2006; Dehay and Bertolotti, 2006). A large number of post-translational modifications, including phosphorylation(Humbert et al., 2002; Thompson et al., 2009; Luo et al., 2005; Schilling et al., 2006), acetylation(Thompson et al., 2009; Jeong et al., 2009), and sumoylation(Steffan et al., 2004; Subramaniam et al., 2009), have been identified on HTT along with several cleavage sites(Wellington et al., 2002; Graham et al., 2006; Gafni et al., 2004). These affect protein localization, degradation, and toxicity. New structural insights into HTT were obtained when Kim, *et al* provided the first crystal structure of $HTT^{exon1}\text{-}Q_{17}$(Kim et al., 2009). In

their analysis, the N17 region adopted an α-helix that extended variable lengths into the polyQ stretch. Shortly within the polyQ stretch, however, the α-helix transitioned into an unstructured random coil that persisted until the polyproline (PP) region. The fact that more than one crystal structure existed within the lattice suggests that certain domains of HTT may be natively unstructured and in dynamic equilibrium with multiple semi-stable conformations. Abnormally expanded polyQ may influence the relative occupancy within this conformational set or favor a completely new type of fold. After the genetic determent of HD was discovered, the causative agent in the disease, be it DNA, mRNA or protein was still unknown. Since then, multiple studies have provided strong evidence that HD is indeed a proteopathy. An inducible transgenic mouse model of HD showed that disease could be turned on and off through inducible expression of the mutant transgene, excluding a DNA-mediated mechanism for disease(Yamamoto et al., 2000). Even earlier, the serendipitous creation of a mouse model of HD, which expressed high levels of mRNA but not the HTT gene product due to an inadvertently introduced stop codon, showed no signs of HD symptoms or pathology(Goldberg et al., 1996). Miller *et al* helped to more precisely connect mHTT to disease by showing that a specific epitope recognized by the 3B5H10 antibody was particularly important in predicting neuronal toxicity, which supports the hypothesis that a single or very select group of mHTT conformers may be responsible for driving disease(Peters-Libeu et al., 2012; Miller et al., 2011). Taken together, these data provide a mechanistic understanding of HD that

implicates abnormally expanded polyQ in causing gain-of-function conformational changes in HTT that then lead to pleiotropic, toxic downstream effects.

Maintaining the Proteome. The importance of protein homeostasis is evident in that HD and over 20 other neurodegenerative disorders show signs of misfolding pathology(Ross and Poirier, 2004). Neurons, as other cell types, have highly conserved molecular machinery to maintain the proteome, including the constitutive and inducible chaperone systems, ubiquitin-proteasome system (UPS), and three types of autophagy (micro, macro, and chaperone mediated). These systems work in concert to dictate both the concentration and conformation of cellular proteins. For a metastable protein like mHTT, the dynamic equilibrium between multiple conformations - diffuse correctly folded, diffuse misfolded (monomer or oligomer), or aggregated into inclusion bodies - is governed by intrinsic intramolecular interactions and extrinsic, cell type specific proteostasis. The proteostasis pathways form a homeostatic envelope that buffers a cell against transient and chronic stresses that perturb the state of the proteome(Powers et al., 2009). The most important response that cells have to protect against acute proteotoxic stresses is called the heat shock response (HSR). The HSR is a highly conserved, cytoprotective pathway that results in the stress-induced transcription of multiple genes encoding heat shock proteins (HSPs). Transcriptional activity of the HSR is mediated by *cis*-acting sequences called heat shock elements (HSE) that exist upstream of many HSPs and are recognized by HSF transcriptional activators(Fernandes et al., 1994). The mammalian family of HSFs has two members that take part in the HSR: *HSF1*

and *HSF2*(Akerfelt et al., 2010). Although *HSF1* is the principal regulator of the HSR, *HSF2* coordinates with *HSF1*, through different *HSF1/HSF2* heterotrimers, to influence differential expression of various HSPs(Ostling et al., 2007). HSPs have been shown to modulate polyQ aggregation properties and toxicity. The most potent HSP regulators seem to be those of the Hsp70 and Hsp40 families, and these directly associate with mHTT(Muchowski et al., 2000). The heat shock class of chaperones forms an intriguing link between aging, proteostasis, and neurodegenerative disease. Pathological onset in neurodegenerative diseases occurs in proportion to the model organism's life span(Morimoto, 2008), which indicates that there are age-dependent processes that either facilitate or are permissive of proteotoxic disease mechanisms. The UPS is the main degradation pathway for the majority of non-aggregated proteins in the nucleus and cytosol. The system is composed of three discrete steps: (1) ubiquitin modification of the target protein, (2) poly-ubiquitin linkage recognition and shuttling, and (3) degradation by the 26S proteasome(Ciechanover and Brundin, 2003). Substrate specificity occurs mostly through E3 ligases that attach a mono-ubiquitin molecule to a lysine residue on the target protein. This action is balanced by a second class of proteins called deubiquitinating enzymes (DUBs) that cleave ubiquitin and prevent protein degradation(Turcu et al., 2009). There is still active investigation into the ubiquitinating and deubiquitinating enzymes involved in HTT turnover and how recognition and degradation might change with abnormally expanded polyQ. Autophagy complements the UPS by degrading long-lived cytosolic proteins and is the only known mechanism by which

aggregated proteins or damaged organelles can be cleared within cells. Multiple lines of evidence show the protective role of autophagy in HD. Inducing autophagy through inhibition of mammalian target of rapamycin (mTOR) had beneficial effects in fly and mouse models of HD, particularly with early treatment(Ravikumar et al., 2004). Trehalose, a non-mTOR dependent autophagy inducer increased clearance of diffuse mHTT, decreased aggregate formation, and increased survival of inducible PC12 cells(Sarkar et al., 2007). A more recent study specifically targeted mHTT to chaperone-mediated autophagy (CMA) by synthetically linking a polyQ binding peptide (QBP1) to heat shock cognate protein (Hsc70) binding motifs. When transduced into the brains of an R6/2 mouse model of HD, the synthetic peptide reduced aggregates, improved symptoms, and increased survival(Bauer et al., 2010).

Malformed Protein Stress Caused by mHTT. One of the first pieces of evidence that cemented the notion of underlying protein dyshomeostasis in HD was gained by the generation of mice expressing exon 1 of HTT with an abnormally expanded CAG repeat(Mangiarini et al., 1996). The mice displayed motor and behaviorally phenotypes, decreased survival, and neuropathological signs that resembled the disease in humans. When the brains were examined, deposits of accumulated mHTT that co-localized with ubiquitin, referred to as neuronal intranuclear inclusions or simply inclusion bodies (IBs), were detected for the first time(Davies et al., 1997). Similar huntingtin positive inclusions were soon confirmed to form in the brains of HD patients(DiFiglia, 1997). More detailed investigation showed that these IBs also contained proteasome subunits and

molecular chaperones, which seemed to suggest that accumulation and deposition of mHTT was occurring despite some response to the malformed protein, even if inadequate. This led to the hypothesis that mHTT taxes cellular homeostatic responses until they are no longer able to meet the challenges presented by the inciting stress of the malformed protein. The risk of neuron death has been shown to remain fairly constant over time(Clarke et al., 2000; Miller et al., 2010a), which means that these stresses may be somewhat stochastic with equal probability throughout the lifetime of a cell. Homeostatic responses, then, may be able to largely meet the challenges presented by mHTT, but in certain cases are overwhelmed due to either random fluctuations in neuronal proteome maintenance, coincident environmental stresses, or the age-dependent decline in cellular protein homeostasis capacity. Although the existence of juvenile onset HD demonstrates that ageing is not required per se for HD to manifest, time increases the chances that a stressful event or combination of events, even with low frequency, occur and are able to negatively affect the homeostatic state. Indeed, mHTT causes stress to the proteome in a number of ways. Expression of mHTT specifically in the cytosol or nucleus caused global impairment of the ubiquitin proteasome system (UPS) in both the cis and trans cellular compartments(Bennett et al., 2005). Our lab found that impairment of the UPS occurred transiently in neurons surrounding IB formation using a live-cell fluorescence reporter targeted to the UPS(Mitra et al., 2009). These findings were later validated *in vivo* in the HD94 and R6/2 mouse models respectively(Bennett et al., 2007). Mounting evidence suggests that these

impairments are not due to direct inhibition of the proteasome as previously thought, but rather result from competition with other ubiquitinated proteins for 26S binding and enzymatic activity(Hipp et al., 2012). Disturbances in autophagy have also been associated with mHTT. Although mHTT causes an increased number of autophagic vacuoles in cells, they are functionally deficient due to a decreased ability to recognize and engulf autophagy substrates(Martinez-Vicente et al., 2010). This leads to the abnormal accumulation of organelles such as damaged mitochondria that are degraded by autophagy and could interfere with the degradation of mHTT oligomers and other aggregated protein species once they form. These changes could have more widespread consequences because autophagy and the UPS are functionally connected. Impairments in autophagy lead to the accumulation of p62/SQSTM1, an ubiquitin binding protein that is only metabolized by autophagy. Increased levels of p62 compete with p97, a UPS shuttling protein, for ubiquitin binding and therefore lead to the accumulation of substrates normally metabolized by the UPS(Korolchuk et al., 2009). Lastly, mHTT causes changes in constitutive and inducible molecular chaperone systems. R6/2 mice show a progressive decrease in chaperone protein levels that correlated with the timeframe in which they were detected within inclusion bodies(Hay et al., 2004). Because no differences were detected in mRNA of the same proteins, the decreased protein levels were attributed to incorporation into IBs. The HSR, the major cellular response to acute proteotoxic stress, is also progressively impaired in R6/2 mice due to chromatin remodeling in the promoters of multiple chaperone loci(Labbadia et al., 2011). mHTT may therefore

place considerable burden on constitutive chaperones due to increased probability of malformation and, in parallel, attenuate inducible responses to acute stresses imposed by mHTT itself, other metastable proteins, or the environment. This large body of work shows that mHTT places considerable stress on multiple protein quality control pathways causing widespread dysfunction. Bolstering homeostatic responses is therefore a leading therapeutic strategy in HD that could be applied to other neurological diseases of protein conformation. A deeper understanding of which responses within cells are adaptive and which ones are maladaptive based on their relationship to cell fate will greatly aid the development of targeted drugs to intervene at a specific place and time in the course of disease.

Chapter 5

Balance Between HSF1 and Hsp90 Attenuates the Acute Stress Response in Neurons

Introduction

Despite the ubiquitous expression of neurodegenerative disease causing proteins throughout the body, the most significant pathology occurs within the central nervous system (CNS). Disease-associated protein accumulation into visible aggregates called inclusion bodies (IBs), a bona fide sign of protein dyshomeostasis, is present within neurons in all of the major neurodegenerative disorders(Ross and Poirier, 2004). Although IBs are able to form in multiple cell types throughout the CNS and body, they show the highest prevalence in neurons. Neurons are a unique cell type because they are long lived, limited only by the lifespan of the organism(Magrassi et al., 2013), are postmitotic, and have high metabolic demands due to the energy required for their activity. If protein dyshomeostasis leads to neuron dysfunction or death, function cannot be restored through new cell production because there is little evidence for neurogenesis in most brain regions. Additionally, mature neurons cannot dilute transient or chronic accumulation of malformed protein through cell division. They must balance fluctuations in the state of the proteome with intrinsic homeostatic responses that keep protein levels within a functional window over an entire lifetime. This is particularly important for metastable, aggregation-prone proteins whose levels are tightly correlated with cellular toxicity.

All cells employ an evolutionarily conserved response pathway called the heat shock response (HSR) to monitor the state of their proteome and restore proteostasis when confronted with acute proteotoxic stresses(Lindquist, 1986; Morimoto, 1998; Powers and Balch, 2013). The HSR buffers cells against the potentially damaging effects of malformed proteins by upregulating a network of molecular chaperones (HSPs) to recognize exposed hydrophobic stretches of amino acids and catalyze refolding or degradation of the parent protein. It is orchestrated by a group of heat shock transcriptional activators (HSFs). Of these, HSF1 and HSF2 are the only two that target HSPs and are also expressed in the CNS in mammals(Akerfelt et al., 2007). We now know that the HSR and other homeostatic responses, including degradation through the ubiquitin proteasome system (UPS), are cell type specific(Prahlad et al., 2008; van Oosten-Hawle et al., 2013; Tsvetkov et al., 2013). Each cell type contains a unique proteome, which requires a similarly unique proteostasis network to ensure proper protein expression and function. As such, an understanding of how neurons specifically cope with disease-associated malformed proteins is best gained by studying the stress responses in neurons. This is even more important in postmitotic cells since HSF1 activity is coupled to the cell cycle(Mendillo et al., 2012). Conclusions obtained from the stress responses of other cell types, including actively dividing or transformed cells, can therefore be misleading if they are used to directly infer pathophysiological mechanisms of proteinopathies that differentially affect neurons.

In order to distinguish neuron specific stress responses, we compared neurons to astrocytes, a closely related cell type within the CNS. We chose astrocytes as a model system because, in contrast to neurons, they are mitotically active, have shorter lifetimes, and show decreased accumulation of malformed protein as judged by a decreased prevalence of IB formation. There is already evidence that neurons do not respond as expected when stressed. After heat shock, primary hippocampal neurons and motor neurons both failed to upregulate Hsp70, the major stress inducible chaperone, whereas glial cultures showed a robust response(Marcuccilli et al., 1996; Batulan et al., 2003). In hippocampal cells, this difference was attributed to lack of HSF1 expression since it is the principal transcriptional activator required for heat-induced gene expression. However, when similarly low expression of HSF1 was observed in the motor neurons, artificially increasing the expression of WT HSF1 did not rescue the response. Only a constitutively activated form of HSF1 was sufficient to induce Hsp70, which suggests that irrespective of expression level, there is either an unresponsive step in the activation cascade of HSF1 or other convergent inhibitory signal that mediates the deficient HSR.

Stress-dependent activation of HSF1 involves initial dissociation from the negative regulating chaperones Hsp90 and Hsp70(Zou et al., 1998). Subsequent HSF1 phosphorylation, structural rearrangement, trimerization, nuclear enrichment, DNA binding at heat shock element (HSE) sequence motifs, and recruitment of transcription machinery causes the transactivation of target genes(Anckar and Sistonen, 2011). The neuronal HSR could potentially be

71

regulated differently at any one of these steps. However, despite repeated reports of a profoundly diminished HSR in multiple neuronal subtypes, the mechanism by which this differential regulation occurs is not known. We therefore used primary murine cultures highly enriched in either neurons or astrocytes to deconvolve the HSR in these two major cell types of the CNS. We show, as in previous studies, that there is a dramatic difference between neurons and astrocytes in the induction of Hsp70 when heat shocked. We extend this finding to other known inducers of the HSR, namely proteasome and Hsp90 inhibition, and report a more detailed picture of how multiple constitutive and inducible chaperones are differentially regulated. We conclude that the deficient acute stress response in neurons results from negative regulation of the HSF1 monomer. High levels of Hsp90 and relatively low levels of HSF1 expression keep HSF1 bound and inactive in neurons. The response is further attenuated by high neuronal turnover of HSF2.

Results

Differential response of neurons and astrocytes to malformed protein

In order to understand how neurons and astrocytes might differ in the regulation of their acute stress response, we developed a culture system that could enrich for the desired cell type after dissection from mouse brains. This allowed us to carry out biochemical assays that minimized the confounding effects of cell type heterogeneity. We chose to dissect primary cortical neurons from mouse embryos because the cells are healthier than postnatally derived neurons and

continue to mature in culture, eventually forming synapses and spontaneous activity by day *in vitro* 12-14 (DIV12-14) (Ichikawa et al., 1993; Kamioka et al., 1996). Because glial cells make up only a small proportion of tissue in the embryonic brain, but increase during the first postnatal week, we isolated glial cells on postnatal day 3. As diagrammed in Fig. 19a, these cells were initially grown to confluency as P0 cultures, passaged twice to remove post-mitotic neurons, and then treated with LME to remove microglia(Hamby et al., 2006). The resulting pure astrocyte culture (Fig. 19b) shows almost no immunoreactivity for Map2 (Fig. 19c). The neuron culture (Fig. 19b) shows low, but detectable immunoreactivity for Gfap, indicating that these cultures have some contamination from glial cells despite being highly enriched for neurons. With these two distinct culture systems, we were able to test if neurons and astrocytes responded differently with their acute stress response to a disease-associated form of HTT with an abnormally expanded polyQ repeat (mHTT). We used mHTT as a model for malformed protein stress because, within a few days of being introduced into neurons, shows objective signs of misfolding by forming visible aggregates called inclusion bodies (IBs). Misfolding and IB formation is specific to the mutant version of HTT.

A

Embryonic day 18-19 → Primary neurons → Culture to 12 days in vitro → Assay

Postnatal day 3 → Primary astrocytes → 2 passages (remove neurons) → Leucine methyl ester (remove microglia) → 2 day recovery → Assay

B

Hoechst / Map2   Hoechst / Gfap

C
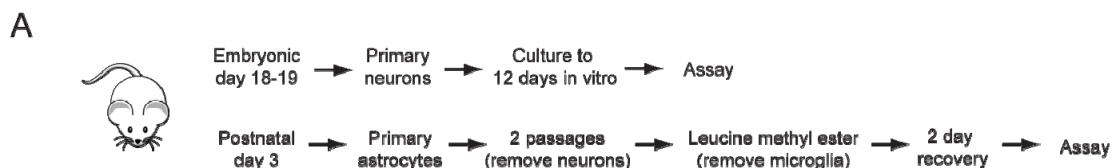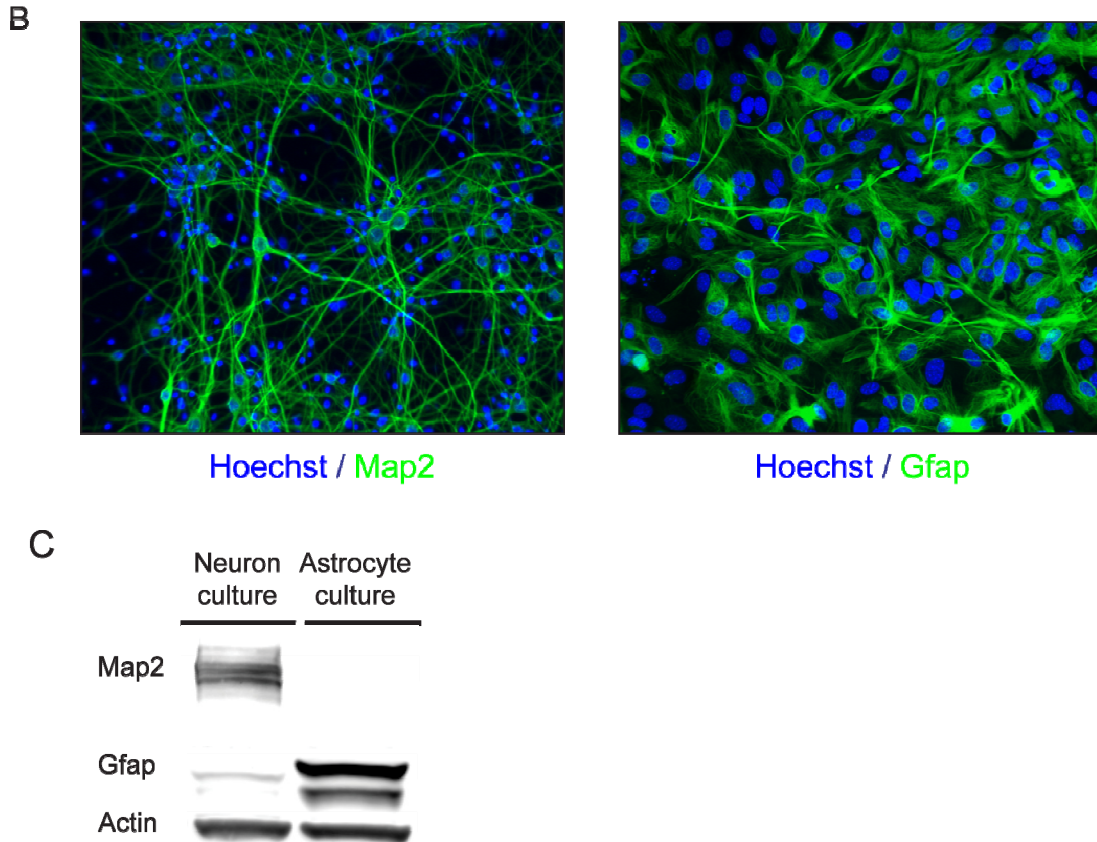
Figure 19. Primary Culture System. (A) Primary neurons and astrocytes were isolated from wild type C57BL/6 mice. Primary cortical neurons were dissected from E18 embryos and cultured until day in vitro 12 (DIV12), when the cultures have formed synapses and are spontaneously active. Primary astrocytes were dissected from postnatal day 3 pups and passaged twice to enrich for dividing cells. The heterogeneous glial cultures were further enriched for astrocytes by the administration of 50mM L-Leucine methyl ester to specifically ablate microglia contamination and recovered for 2 days in astrocyte growth medium. (B) Representative images of the two different culture systems at the time of assay. Cultures were fixed and stained with either Map2 (Millipre MAB3418) or Gfap (Dako Z0334) antibody. Hoechst stain was included in the wash step for the

secondary antibodies. (C) A western blot was performed to determine the amount of neuronal and astrocyte enrichment in the respective cultures. Quantification of the western blot showed a Map2 mean value normalized to loading control of 0.351 in the Neuron culture and 0.089 in the Astrocyte culture. (p=0.003). The Gfap value normalized to loading control was 1.978 for the Neuron culture and 14.483 for the Astrocyte culture (p=5.709e-5). Student's Two Sample t-test was used to test for the difference in means between the groups. This demonstrates that the two culture systems are distinct and highly enriched for the desired neural cell type.

We introduced either an EGFP control plasmid or a 586 aa fragment of HTT with a disease-associated $(Q)_{136}$ repeat fused to EGFP (HTT^{586}-Q_{136}-EGFP). The fragment corresponds to the N-terminal portion of HTT up to the Caspase-6 cleavage site, and is a known pathological fragment or precursor fragment of full length HTT produced *in vivo*(Graham et al., 2006). We then measured the response to the mutant protein by immunolabeling cells for endogenous Hsp70, the major inducible chaperone that is expressed in response to acute protetoxic stress. In astrocytes, 48 hours after transfection, there was no detectable expression of Hsp70 in response to EGFP alone, but in response to HTT^{586}-Q_{136}-EGFP, astrocytes showed a significant induction of Hsp70 (Fig. 20a,b). The response to mHTT was concentrated at local sites of misfolding within IBs, which suggested that the response was directed towards the malformed protein. Exposing cells to elevated temperatures also causes widespread protein

misfolding and activation of the acute stress response. We used a 42°C heat shock (HS) for 3 hours as a theoretical upper limit to Hsp70 induction. The response in astrocytes to mHTT was intermediate between EGFP and HS. When we stratified mHTT expressing astrocytes into cells with or without IBs, Hsp70 induction segregated almost perfectly with IB formation (Fig. 20c). The astrocytes that did not have IBs showed no significant difference in Hsp70 whereas those with IBs experessed Hsp70 to the same level as HS. Even though malformed monomeric and oligomeric species precede IB formation, these results indicate that either 1) the acute stress response is activated only when overt protein misfolding is present, perhaps at a time when cells can no longer cope with diffuse species, or 2) that the stress response itself promotes IB formation.

When we conducted the same experiment in neurons, however, we were surprised to find that they did not respond similarly (Fig. 20d,e). As expected, neurons had low Hsp70 expression in response to EGFP alone, but in contrast to astrocytes, neurons showed no induction of Hsp70 in response to HTT^{586}-Q$_{136}$-EGFP. Overall expression of Hsp70 did not increase and there was no concentration of Hsp70 at sites of IB formation. We were concerned that if the prevalence of IB formation was different between neurons and astrocytes, we could bias our results. We therefore stratified the neuron population into cells with or without IBs as we did for astrocytes (Fig. 20f). Neurons with IBs still had no significant induction of Hsp70. We therefore concluded that neurons have a deficient response to at least one type of disease-associated, malformed protein.

Neurons have a deficient chaperone response to thermal stress

We wondered if the difference we detected in neurons was unique to malformed protein, or if it was a more general principle of how neurons respond to acute proteotoxic stresses. We exposed neurons or astrocytes to either 37°C or a 42°C heat shock (HS) for 1, 2, or 3 hours and blotted for both constitutive and inducible chaperones that take part in the heat shock response (HSR) (Fig. 21a). We found that neurons had a significantly decreased response compared to astrocytes at Hsp70 and Hsp27, two highly inducible chaperones regulated by the HSR (Fig. 21b,c). No significant change was detected for either Hsp90 or Hsp40 (data not shown).

A

D

	EGFP	HTT^{586}-Q$_{136}$-EGFP
mApple/Composite		
Hoechst/EGFP		
Hoechst/Hsp70		

10μm
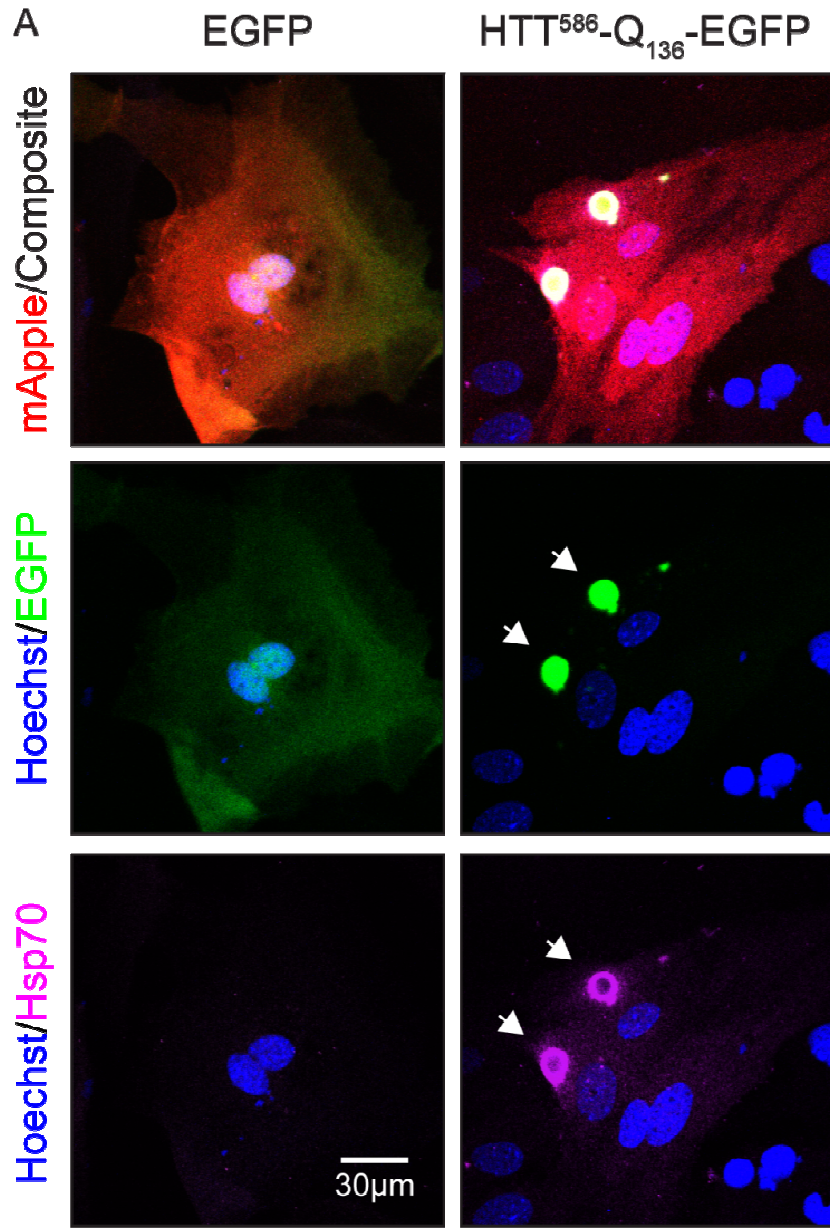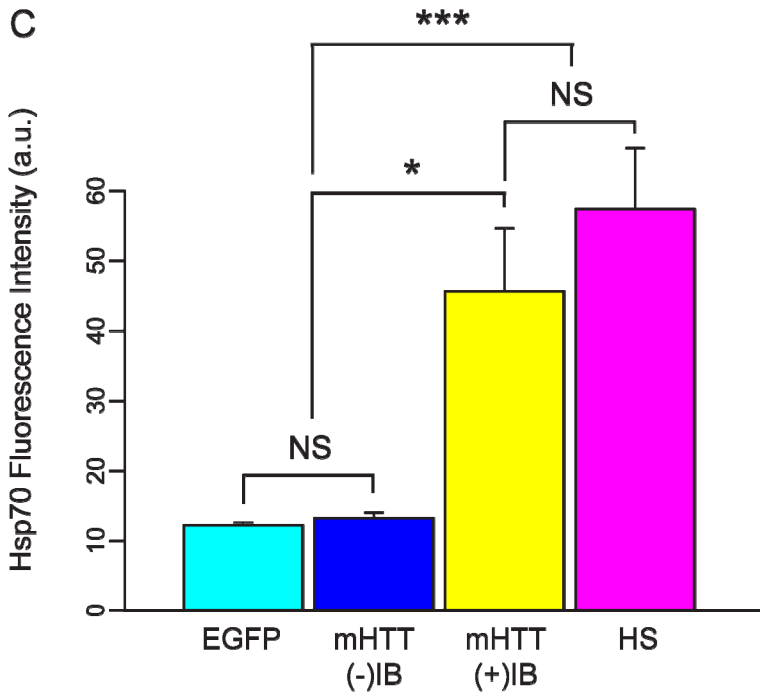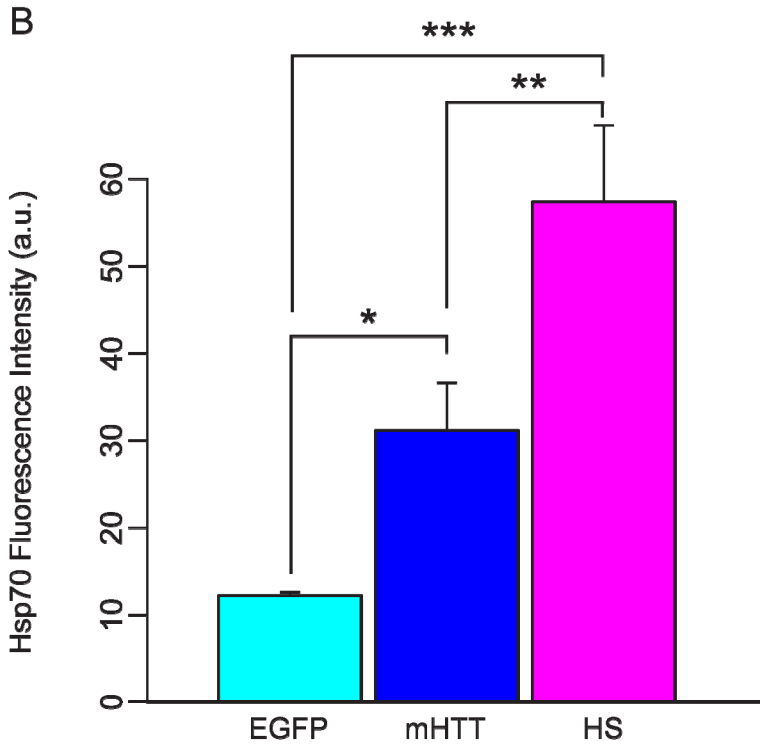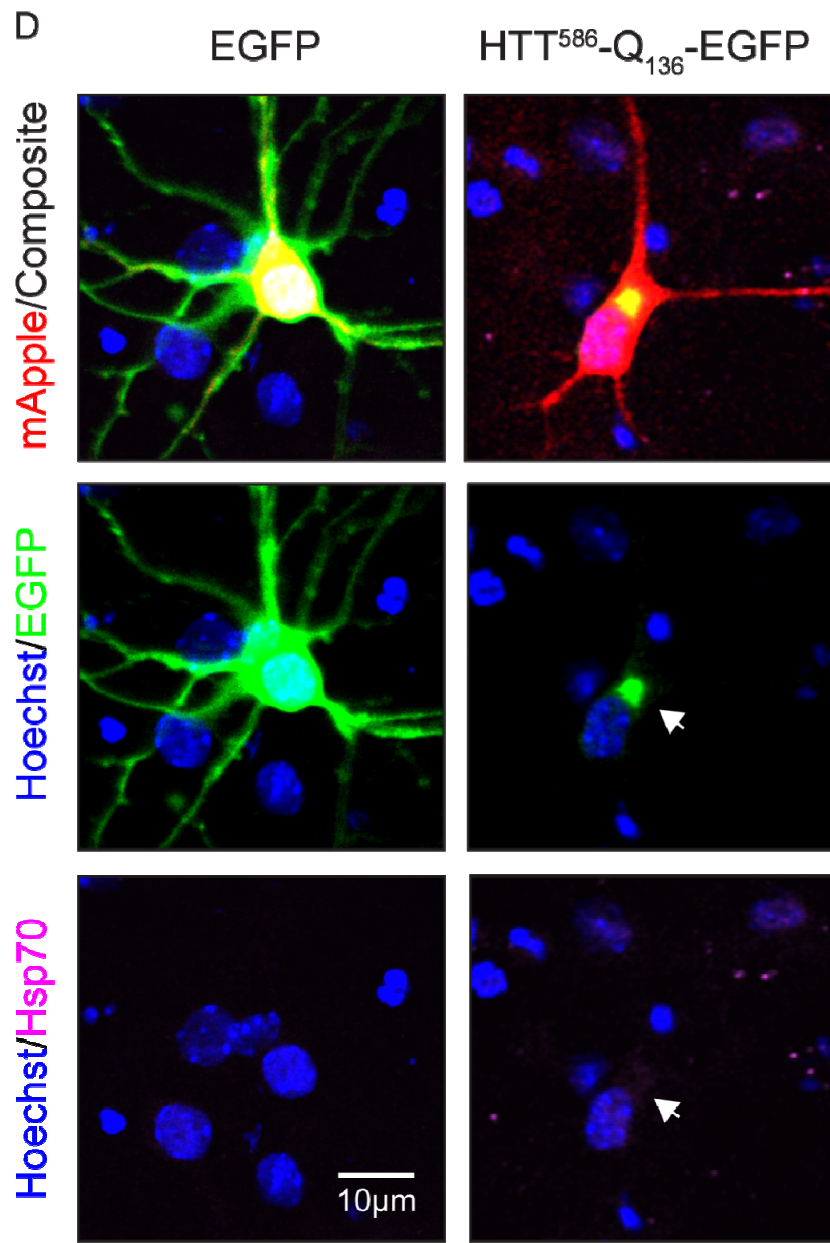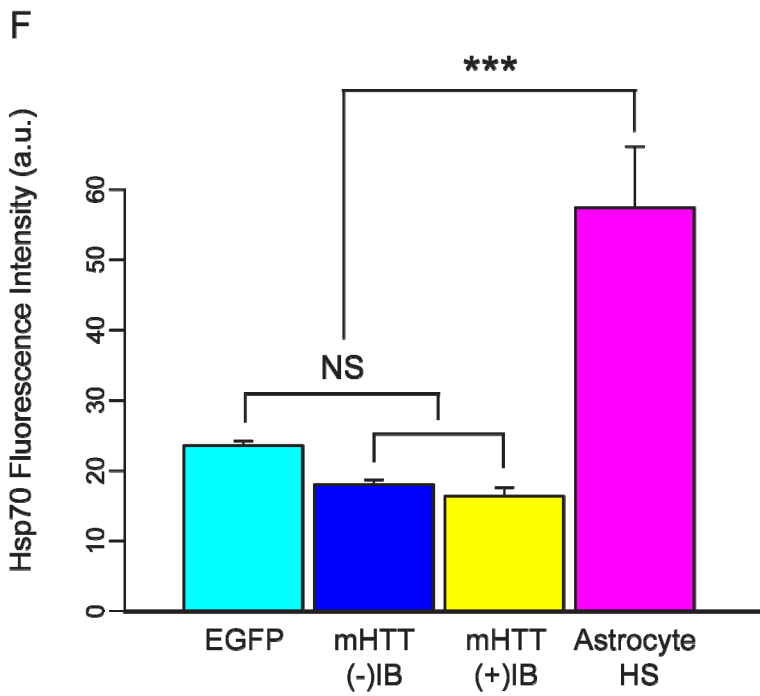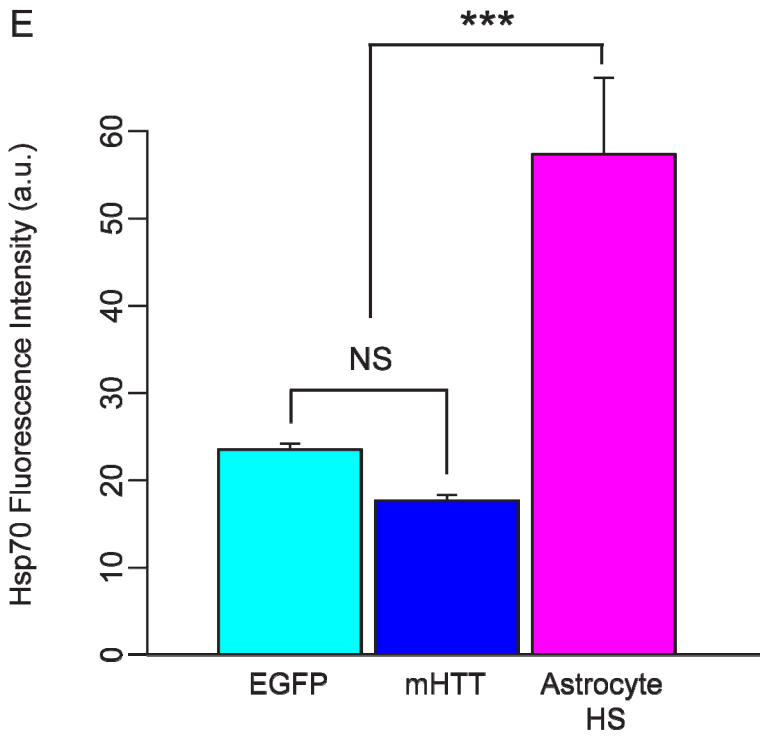
Figure 20. Neurons have a deficient Hsp70 response to disease-associated polyQ expanded HTT. (A) Primary astrocyte were cultured on coverslips and two days after treatment with LME, transfected with either a plasmid expressing

EGFP alone or a 586 amino acid fragment of HTT with a disease-associated polyQ expansion (Q_{136}) fused to EGFP (HTT^{586}-Q_{136}-EGFP). Transfected cells were labeled by a co-transfection plasmid expressing mApple (red). 48 hours post-transfection, the cultures were fixed and labeled for endogenous Hsp70 with Hsp70 primary antibody (Enzo SPA-810) and an Alexa-647 conjugated secondary antibody (magenta). Hoechst stain (blue) was added to the last wash. The cells were then imaged by confocal microscopy. The Hsp70 response in astrocytes is seen by the preferential labeling of Hsp70 in cells that have been transfected with HTT^{586}-Q_{136}-EGFP compared to cells transfected with EGFP alone. Ring enhancement of Hsp70 around sites where IBs have formed (white arrowheads) shows specific recognition of HTT^{586}-Q_{136}-EGFP by Hsp70. (B) The Hsp70 response was quantified by measuring mean Hsp70 signal within a boundary defined by the mApple transfection marker. 3 hour heat shock (HS) at 42°C was used as a positive control for Hsp70 induction. mHTT is short hand for HTT^{586}-Q_{136}-EGFP. (C) When the population was stratified by IB formation (visible aggregates), Hsp70 induction occurred specifically in those cells that formed IBs, and there was no longer a significant difference in Hsp70 expression between mHTT and HS. (D) Neuronal cultures were transfected, antibody labeled, and imaged in the same way. No visible induction of Hsp70 was seen, even at sites of IB formation (white arrowhead). (E) Quantification of mean Hsp70 signal within the cell boundary defined by the co-transfection marker. The Hsp70 signal from Astrocyte HS during the same experiment was used for reference. Neurons show no significant difference in Hsp70 expression when

compared to EGFP alone. (F) Even when stratified by IB formation, neurons show no detectable induction of Hsp70. For all plots, error bars indicate standard error of the mean (s.e.m). Significance calculated by pairwise t-test using the Holm correction method for multiple comparisons. $p < 0.001$ (***), $p < 0.01$ (**), $p < 0.05$ (*), $p > 0.05$ (NS). $n > 30$ for each of the conditions except when stratified.

After HS, a small, time-dependent increase in Hsp70 was observed within neurons. In order to determine if the increase was a result of an attenuated response in neurons or due to glial contamination within the culture, we performed immunocytochemistry to deconvolve the Hsp70 signal coming from neurons and astrocytes. At 37°C, both neurons and astrocytes within the culture had minimal Hsp70 immunofluorescence (Fig 21d). At 42°C, Hsp70 was induced in astrocytes, as determined by colocalization with the astrocyte specific marker Gfap, but not in surrounding Map2 labeled neurons. Measuring mean Hsp70 fluorescence from all Map2 labeled neurons and comparing them to Gfap labeled astrocytes revealed that neurons indeed had no significant induction of Hsp70 after HS, whereas astrocytes had an expected and highly significant response (Fig. 21d). We therefore concluded that a deficient Hsp70 response in neurons is not limited to malformed protein, but is also true in response to HS, one of the most robust activators of the HSR.

The HSR is a highly regulated system that includes negative feedback to attenuate the response once it is turned on. We reasoned that neurons might have a response, but we were missing it due to particularly strong negative

feedback within the system that would prevent appreciable levels of chaperones from accumulating. Thus, we performed quantitative real time PCR (qRT-PCR) on neurons and astrocytes to measure the immediate transcript response to HS. In agreement with Hsp70 protein levels, total Hsp70 transcript was only minimally induced in neurons, and despite no significant difference in Hsp70 at the normal temperature between neurons and astrocytes, large differences were detected for all durations of HS. The small increase in Hsp70 transcript starting at 2 hours HS is again likely due to the small amount of astrocyte contamination in the culture.

We further wondered if the deficit in transcript response was unique to the Hsp70 locus or existed at other known targets of the HSR. We performed qRT-PCR for Hsp40 (Dnajb1), Hsp27 (Hspb1) and Hsp90 (Hsp90aa1), three genes that are preferentially transcribed during acute thermal stress, and found that neurons showed deficits in induction of all of these genes when compared to astrocytes (Fig. 22a-c). Because neurons and astrocytes showed differences in expression of Hsp90 at 37°C, we normalized the relative transcript amounts in the two cell types to the starting amount in order to test for pure induction (Fig. 22d). When we did this, the difference between neurons and astrocytes was even more evident.

In general, we conclude that neurons have a deficient response to acute thermal stress as measured by lack of induction of multiple outputs of the inducible chaperone system including Hsp70, the major inducible chaperone of the HSR. The deficiency can be traced back to at least the step of transcription, which

suggests that neurons simply have low expression of heat shock transcriptional regulators, too low to effectively drive major outputs of the HSR, or that there are upstream regulatory differences in neurons that prevent the transduction of stimulus to response.

D

37°C 　　　3hr 42°C

Hoechst/Gfap/Map2/Hsp70

Hoechst/Gfap

Hoechst/Hsp70

30μm

E

Hsp70 Fluorescence Intensity (a.u.)

■ Neuron
■ Astrocyte

***

37°C 　　42°C
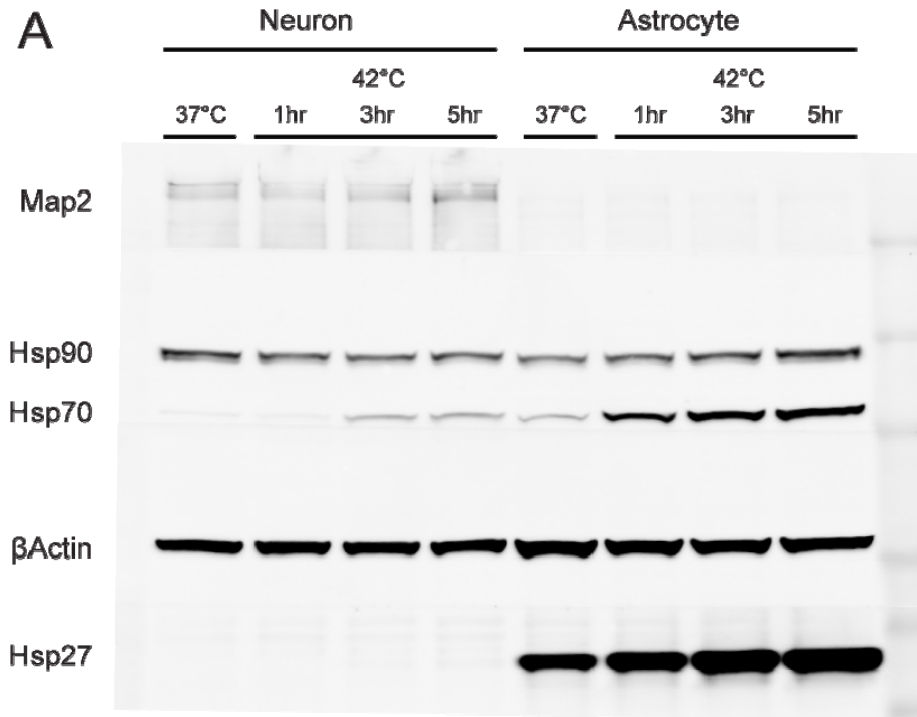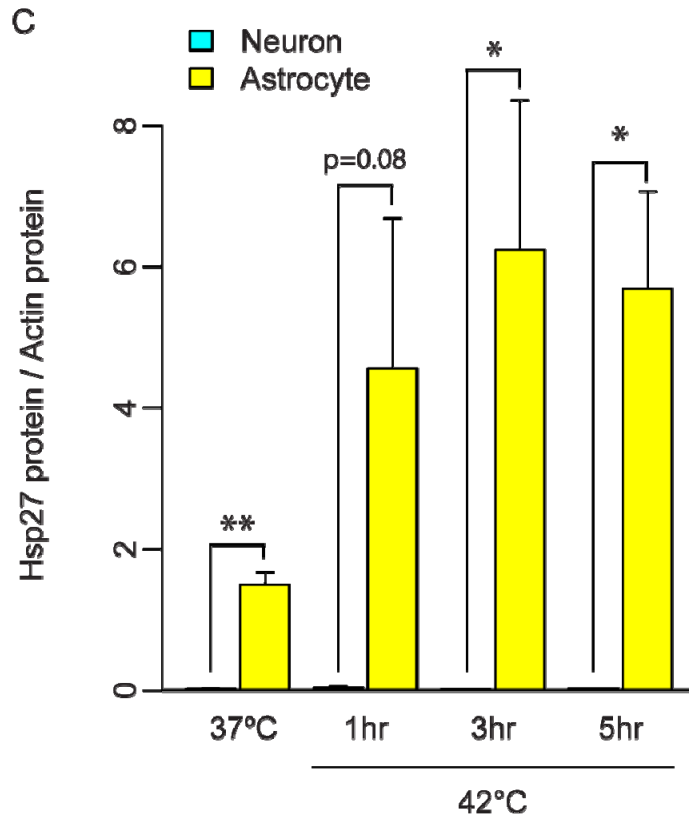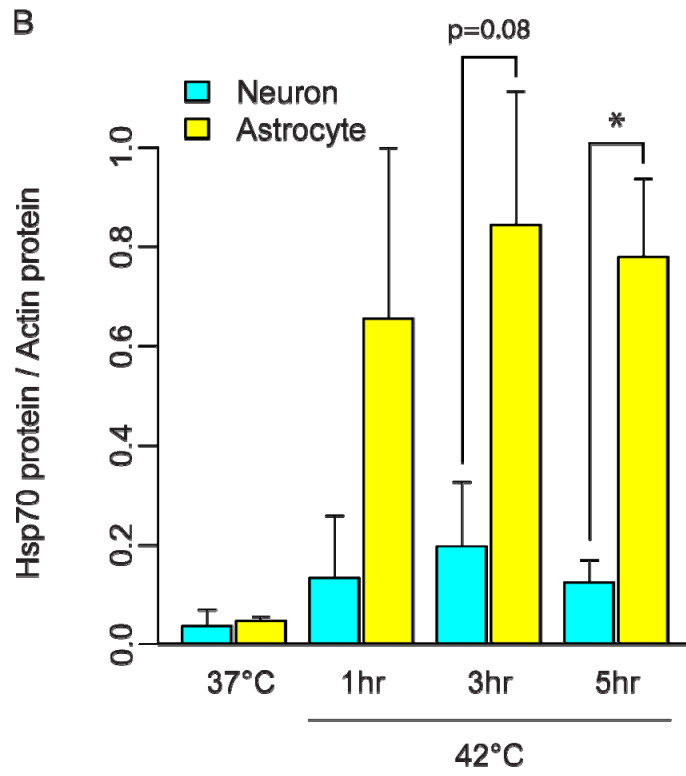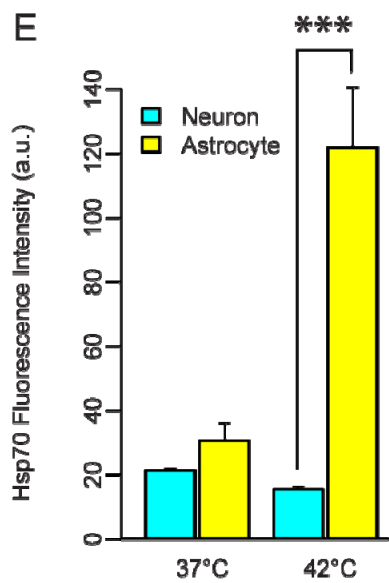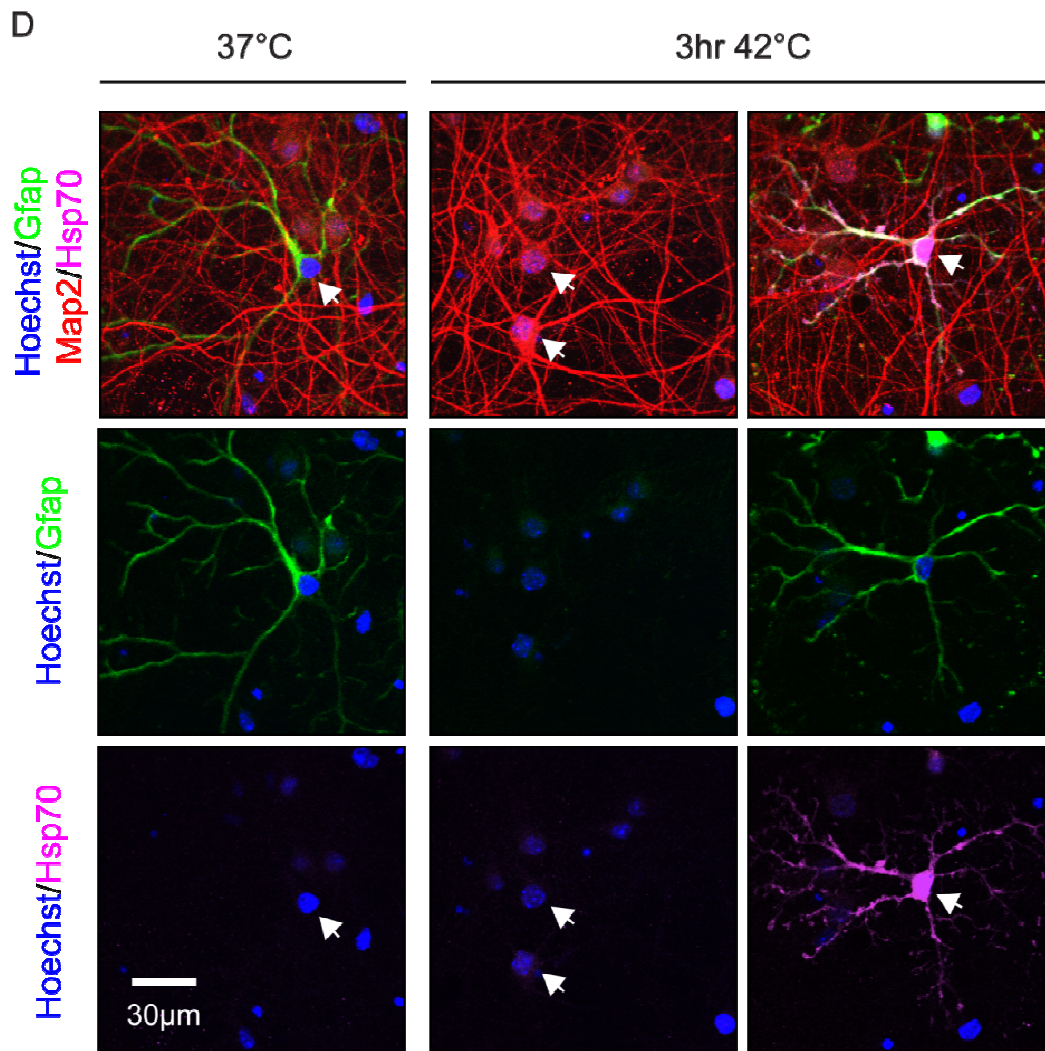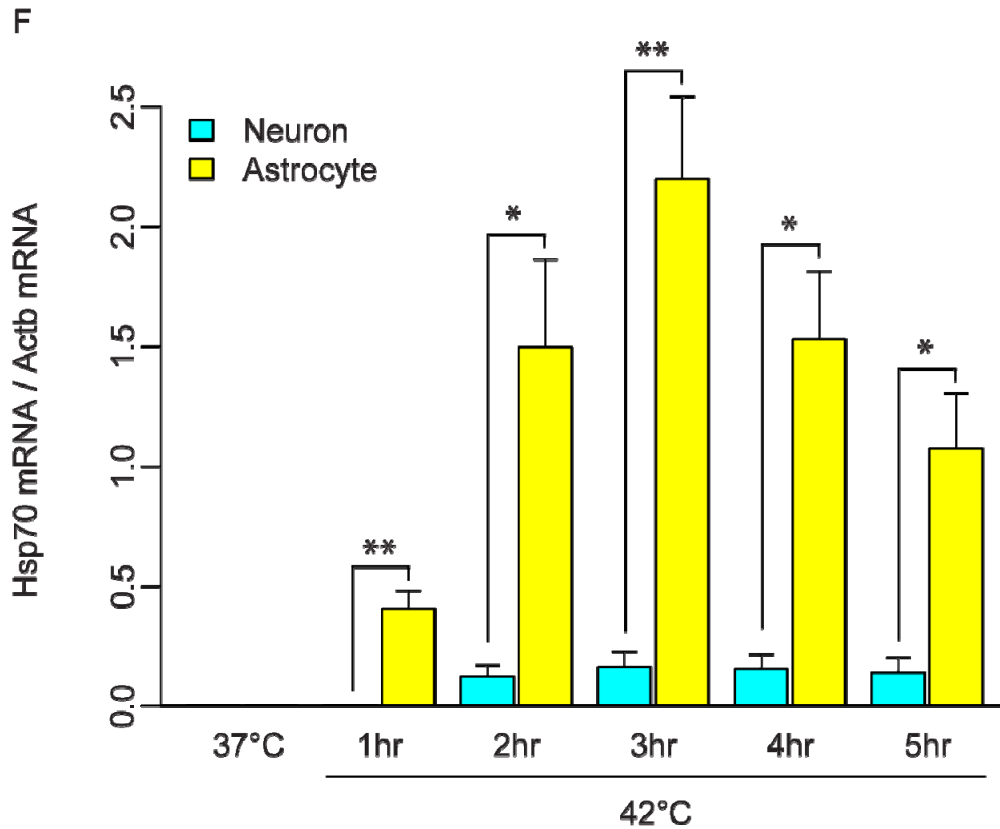
Figure 21. Neurons have an attenuated Hsp70 response to thermal stress.

(A) Neurons or astrocytes were exposed to 37°C or 42°C HS (1, 3, or 5 hours) and allowed to recover for 20 hours at 37°C. Cell extracts (30ug per lane) were blotted with antibodies against the constitutive chaperone Hsp90 and major inducible chaperones Hsp70 and Hsp27. Blotting with Map2 antibody was used to assess the purity of the cultures and βActin was used as a loading control. IRDye 800CW (Map2, Hsp70, Hsp27 and βActin) and IRDye 680LT (Hsp90) conjugated secondary antibodies were imaged on a Licor Odyssey CLx. (B) Astrocytes have a significantly greater levels of Hsp70 than neurons after 5 hours HS. (C) In contrast to astrocytes, neurons have no detectable expression of the small heat shock protein Hsp27 at 37°C or after prolonged HS. (D) Astrocytes within the neuron enriched culture are responsible for the Hsp70 response

detected by western blot (WB). Using immunocytochemistry to deconvolve the neuron culture Hsp70 response, neurons were exposed to 37°C or 3 hours at 42°C (HS) and allowed to recover for 20 hours at 37°C. Cells were fixed and subjected to immunocytochemistry using primary antibodies against Map2 (Aves #MAP) to label neurons, Gfap (Dako Z0334) to label astrocytes and Hsp70 (SPA-810). Fluorescence from Alexa 488 (green), Alexa 555 (red) and Alexa 647 (magenta) conjugated secondary antibodies to detect Gfap, Map2 and Hsp70 respectively was collected with confocal microscopy. At 37°C, neurons and astrocytes (white arrowhead) did not show Hsp70 immunofluorescence. After HS, Hsp70 immunofluorescence was specifically detected in astrocytes (white arrowheads pointing to Gfap positive cell), but not neurons (white arrowheads pointing to Map2 positive cells). (E) Mean Hsp70 fluorescence was measured from neurons and astrocytes (>30 cells each) as determined by Map2 and Gfap co-labeling. a.u., arbitrary units. (F) Transcript response at the Hsp70 locus (Hspa1a). Neurons or astrocytes were exposed to 37°C or 42°C (1, 2, 3, 4 or 5 hours) and cells were immediately lysed to extract total RNA. cDNA was prepared and followed with quantitative real time PCR (qRT-PCR). Ct values were averaged from three replicate wells, and the ΔΔCt method was used to quantify Hspa1a RNA relative to the reference gene β-actin (Actb). Similar results were obtained for Hspa1b (data not shown). Error bars represent 3 biological replicates for 37°C, 1 hr HS, and 3 hr HS. Error bars from 2, 4 and 5 hr HS represent 2 biological replicates. For all plots, error bars indicate s.e.m.

Significance calculated by Student's two sample t-test. p<0.001 (***), p<0.01 (**), p<0.05 (*).
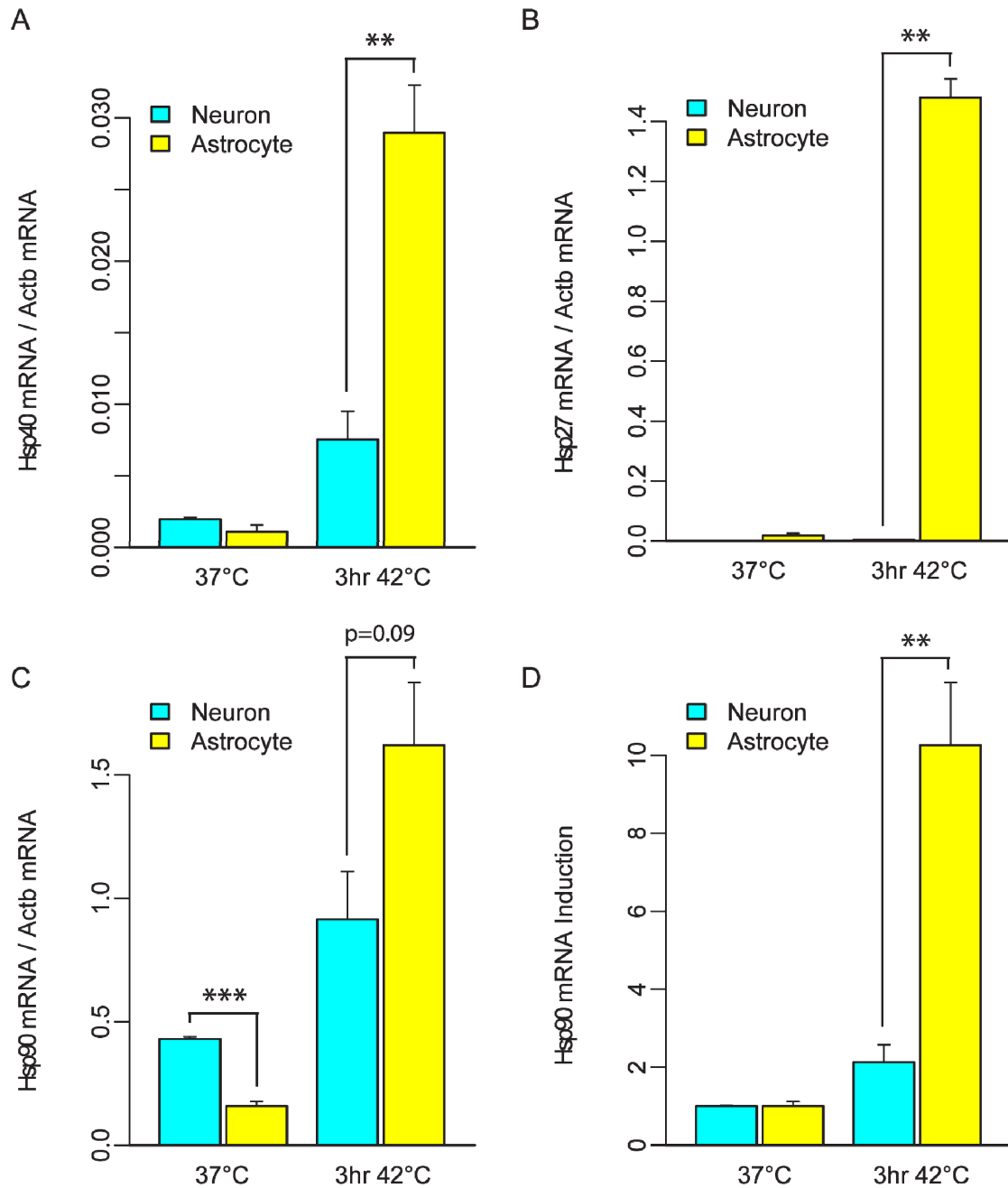
Figure 22. Neuron attenuated response to thermal stress occurs at multiple HSF1 target loci. (A-C) qRT-PCR was performed using the same cDNA as for

Hsp70. Primers for either Hsp40 (Dnajb1), Hsp27 (Hspb1), or Hsp90 (Hsp90aa1) were used in the reactions. Data represent three biological replicates. Error bars indicate s.e.m. Significance calculated by Student's two sample t-test. $p<0.001$ (***), $p<0.01$ (**), $p<0.05$ (*).

The differential stress response in neurons and astrocytes extends to Hsp90 inhibition

Another robust activator of the acute stress response is Hsp90 inhibition(Westerheide and Morimoto, 2005). Under non-stressed conditions, Hsp90 binds and inactivates HSF1, the major stress-responsive transcriptional regulator, preventing DNA binding and transactivation of HSF1 target genes. Small molecule inhibition of Hsp90 is thought to directly disrupt the Hsp90-HSF1 interaction, releasing HSF1 and enhancing its ability to be activated and initiate the HSR. Because Hsp90 binding agents (HBA) that activate the HSR have been pursued as potential therapeutics for neurodegenerative diseases of protein conformation, we were interested to see if our results could be extended to Hsp90 inhibition. We used tanespimycin (17-AAG), a potent analog of geldanamycin, that competes with nucleotide binding at the Hsp90 ATP-binding pocket. Similarly to HS, we exposed neurons or astrocytes to either DMSO or 1, 3, or 5 hours of 17-AAG and blotted for Hsp70 after overnight incubation to let protein accumulate (Fig. 23a). Indeed, when we quantified Hsp70 protein levels, neurons showed no significant response to 17-AAG, even after long incubation times with the drug (Fig. 23b). Astrocytes, however, showed a large and

significant response as expected. We again wanted to make sure that we were not missing a short-lived immediate transcript response. In agreement with protein levels, no transcript response was observed in neurons, but astrocytes showed a significant response starting at 3 hours, which continued to increase until the last time point tested (Fig. 23c).

A

| | Neuron | | | | Astrocyte | | | |

B
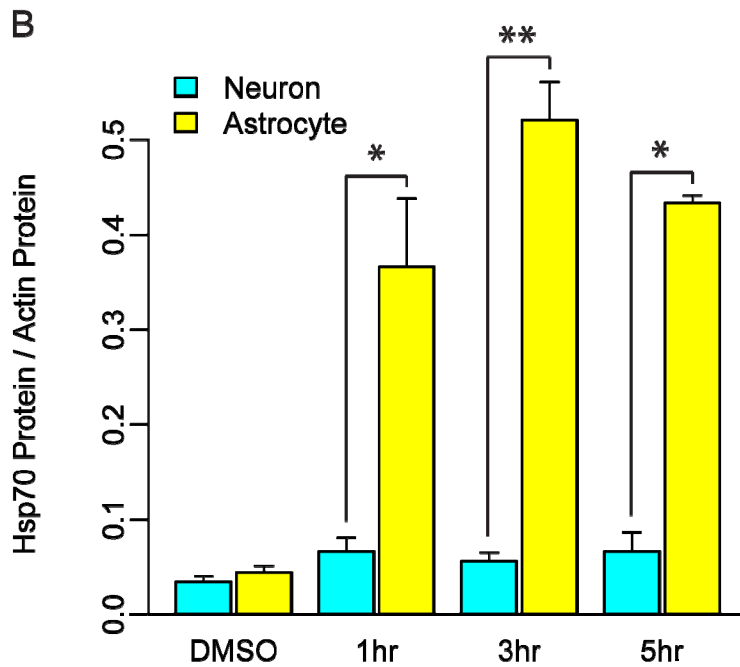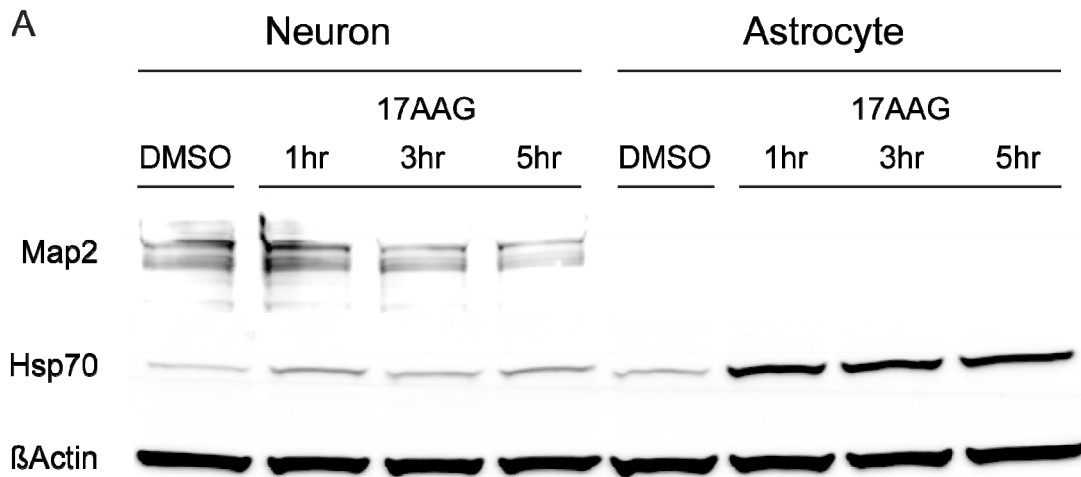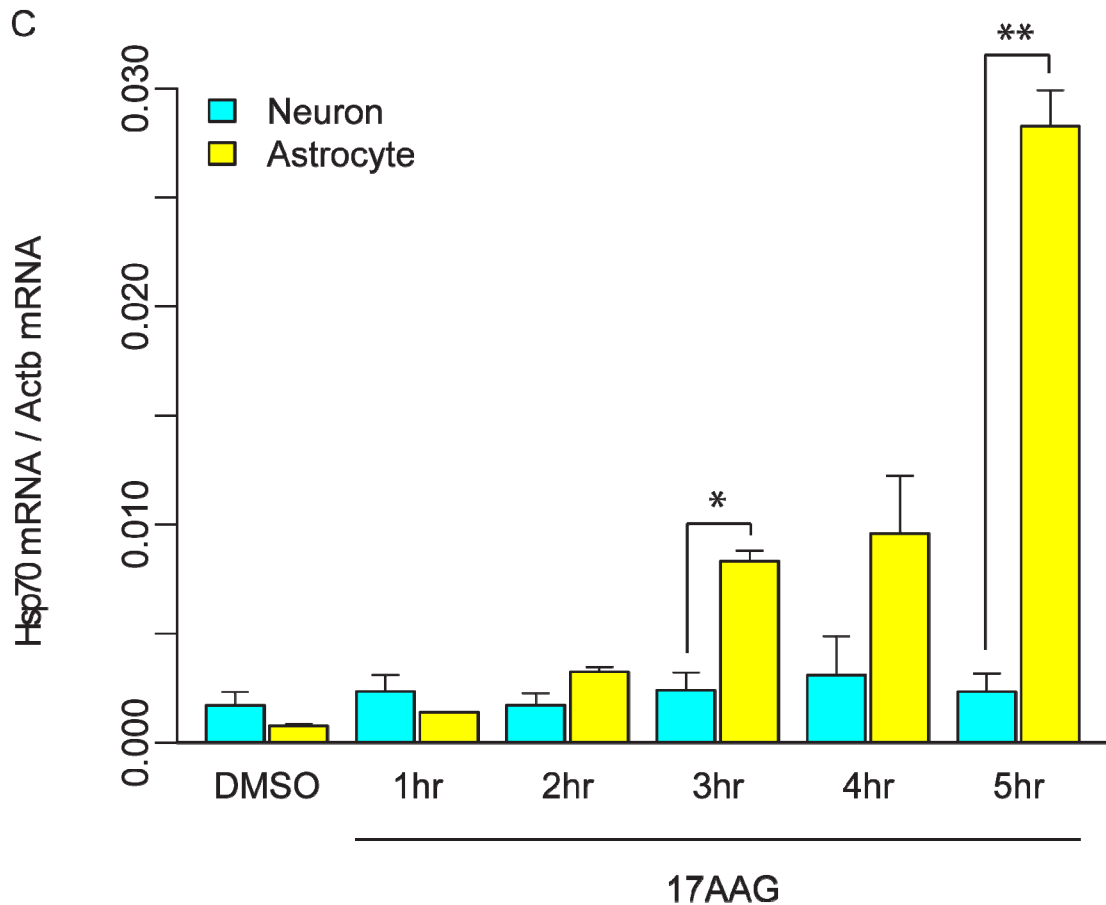
Figure 23. Neurons have deficient Hsp70 response to Hsp90 inhibition. (A) Neurons or astrocytes were incubated with either DMSO or 5uM 17-allylamino-17-demethoxygeldanamycin (17-AAG), a potent Hsp90 inhibitor (1, 3, or 5 hours) that activates HSF1. The cells were washed twice, replaced with conditioned medium and allowed to recover for 20 hours. Cell extracts (30ug per lane) were blotted with antibodies against Hsp70, Map2 to assess culture purity and βActin as a loading control. IRDye 800CW conjugated secondary was imaged on a Licor Odyssey CLx. (B) Neurons were completely deficient in inducing Hsp70 at all time points measured. (C) Neuron Hsp70 transcript response was also absent up to 5 hours after drug treatment. Neurons or astrocytes were treated with 17-AAG (1, 2, 3, 4, or 5 hours) and total RNA was collected immediately following drug

treatment. cDNA was prepared and qRT-PCR was performed. Hsp70 (Hspa1a) transcript abundance relative to β-Actin was calculated by the ΔΔCt method. Error bars indicate s.e.m from 2 biological replicates. Significance calculated by Student's two sample t-test. $p < 0.01$ (**), $p < 0.05$ (*).

Neurons have decreased expression of both HSF1 and HSF2

Because decreased expression of HSF1 has been proposed as a mechanism for cells that do not respond appropriately to acute proteotoxic stresses, we investigated expression levels of the two major heat-shock transcriptional regulators known to mediate the inducible chaperone response. We performed qRT-PCR to measure total transcript levels of HSF1 and HSF2 relative to the reference gene β-Actin. Neurons had lower levels of HSF1 compared to astrocytes, but higher levels of HSF2 (Fig. 24a). We sought to determine if these differences could be replicated when looking at protein levels of the heat shock factors. The difference seen in HSF1 protein levels followed a similar trend to that of the transcript, but the difference was amplified and became even more significant (Fig. 24b,c). However, we were surprised to find that HSF2 protein levels did not agree with HSF2 transcript. Neurons, despite having higher amounts of HSF2 transcript, had significantly lower expression of HSF2 protein (Fig. 24d,e). This is interesting because we know HSF1 and HSF2 are regulated very differently in cells. HSF1 is constitutively expressed and its activity is regulated by binding to Hsp90. In contrast, HSF2 is regulated by a balance of expression and degradation through the ubiquitin-proteasome system

94

(UPS)(Mathew et al., 1998). Higher transcript and lower protein therefore suggests that neurons have particularly high turnover of HSF2, which could be caused by higher global activity of the UPS in neurons or a specific destabilization of the molecule based on the neuronal set of ubiquitinating and deubiquitinating enzymes. Irrespective, the result is that neurons have a particularly low expression of HSF1 and HSF2, the two major stress-responsive factors that govern the sensitivity and magnitude of the inducible stress response within cells.
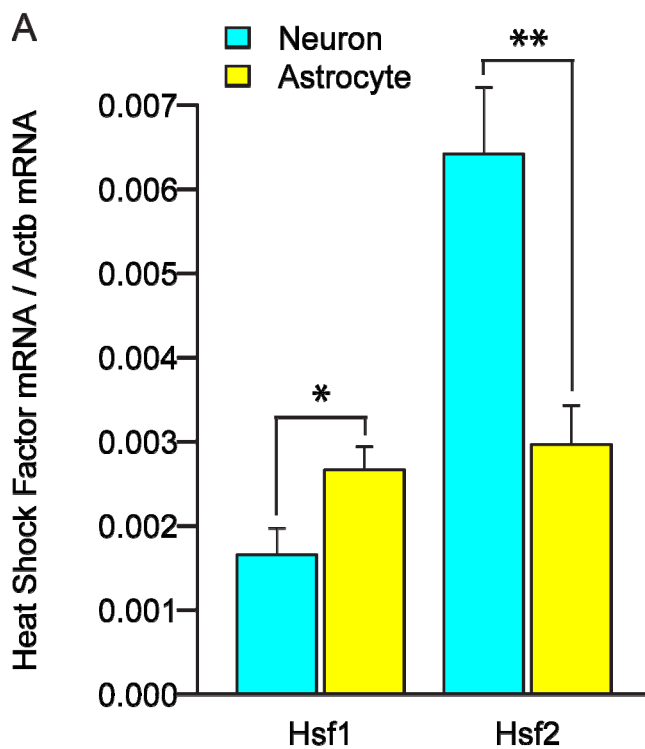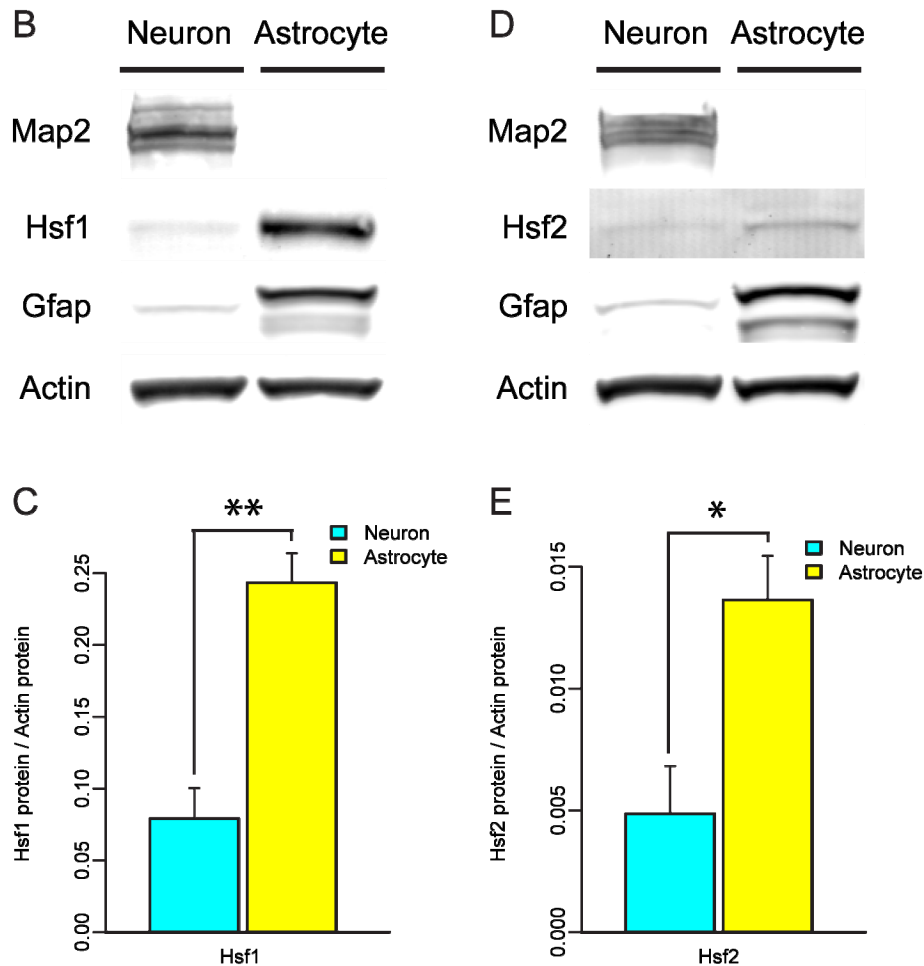
Figure 24. Heat shock factors are differentially expressed in neurons and astrocytes. (A) Compared to astrocytes, neurons have lower Hsf1 transcript, but higher Hsf2 transcript. Total RNA was collected from untreated samples and transcript abundance was calculated as previously described. Error bars indicate s.e.m. from 6 biological replicates. (B-E) Neurons have lower protein expression of both Hsf1 and Hsf2. Extracts from neurons or astrocytes (30ug per lane) were blotted for Hsf1 (clone 10H8) or Hsf2 (clone 3E2). Map2 and Gfap were used to assess culture purity and β-Actin was used as a loading control. Fluorescence from IRDye 800CW-conjugated secondary to Map2, Hsf1 and β-Actin and IRDye 680LT-conjugated secondary to Gfap was collected on a Licor Odyssey CLx.

Error bars indicate s.e.m from 3 biological replicates. Significance calculated by Student's two sample t-test. p<0.01 (**), p<0.05 (*).

Increasing HSF1 in neurons restores the inducible stress response and protects against malformed protein

Induction of heat shock factor target genes relies on a multistep cascade of activation, trimerization, DNA binding and transactivation. Although neurons have decreased heat shock factor expression, this might not be the rate limiting step or it could be one of a series of limiting steps that would need to be overcome to restore the response. Increasing expression could be sufficient, as one study proposed(Marcuccilli et al., 1996), or there could be additional inhibitory signaling that could repress the response(Batulan et al., 2003). We generated virus that expressed either HSF1 or a version of HSF1 that contained a single amino acid change within the N-terminal DNA binding domain to greatly decrease the DNA binding efficiency of the molecule (HSF1-R71G). We transduced the viruses into neurons and verified neuronal expression by immunocytochemistry (Fig. 25a). We then performed qRT-PCR to determine the relative amount of overexpression within our culture. Both HSF1and HSF1-R71G were expressed to a similar degree and were greatly enriched over endogenous levels of HSF1 (Fig. 25b).

We now had neurons that expressed HSF1 above the levels seen in astrocytes. We reasoned that if HSF1 expression was indeed a limiting factor of the response in neurons and the major difference between neurons and astrocytes, then we should see a robust response in the neurons that now had high HSF1.

We used the same concentration of 17-AAG as before and performed qRT-PCR to measure the response at the Hsp70 (Hspa1a) locus. Whereas we observed only a small increase in Hsp70 in neurons overexpressing HSF1 without 17-AAG treatment, there was a robust, roughly linear increase in Hsp70 transcript over the course of 5 hours with 17-AAG (Fig. 25c). The magnitude of the response in neurons was now approximately 10 fold higher than that seen in astrocytes with only endogenous HSF1. Importantly, this effect was specific to HSF1. HSF1-R71G did not show any gene induction over baseline, meaning that DNA binding was necessary for the effect, and it could not be attributed to non-specific stress augmentation resulting from the viral transduction.

Cells must maintain proteostasis for their proper function and survival. It is generally thought cells express a set of constitutive chaperones and regulate their inducible stress response to directly balance the cell-specific demands of the proteome. We wondered, then, what the functional consequence of perturbing the stress response was. In order to do this, we turned to our robotic microscope system that is able to longitudinally track individual cells over time and, coupled with powerful statistical models, can determine the extent to which various cellular risk factors identified throughout the lifetime of a cell predict cell fate(Arrasate and Finkbeiner, 2005). Using this technology, we asked whether neurons coping with a malformed protein could benefit from the enhanced ability of HSF1 expressing cells to respond to proteotoxic stresses and perhaps reinstate cellular proteostasis.

We transfected neurons with a 586 aa fragment of HTT that contained either a polyQ repeat within the normal range (Q_{17}) or a disease-associated abnormally expanded polyQ repeat (Q_{136}) fused to EGFP (mHTT). Along with the polyQ expanded protein, we co-transfected either HSF1 or the HSF1-R71G mutant in order to determine the effects of HSF1 on polyQ mediated toxicity. When we compared the survival of cells with or without mHTT, the cells with mHTT had a significantly higher risk of death as seen by the shift in the survival curve towards higher cumulative hazard (Fig. 25d). When we quantified the effect of HSF1, we found that HSF1 was able to completely abrogate the toxicity caused by mHTT. The risk of death was no longer distinguishable from neurons transfected with HTT containing a normal polyQ repeat. Furthermore, because HSF1-R71G had no apparent effect, we concluded that HSF1 required transcriptional activity to counteract the toxic effects of the malformed protein.

HSF1 has thousands of targets throughout the genome and influences a very diverse set of cellular functions. As such, the increased survival that we observed in neurons coping with mHTT could in theory be attributed to HSF1 action at any number of these genes. We therefore tested the effect of HSF1 on HTT with a normal polyQ repeat (Fig. 25e). In this case, we saw no added benefit to HSF1, indicating that the ability of HSF1 to promote neuron survival is contingent on neurons experiencing a concomitant stressful change to their proteome such as the introduction of an aggregation-prone metastable protein like mHTT. The result is therefore not likely explained by a non-specific trophic effect of HSF1.

One potential mechanism for the mitigating effects of HSF1 on mHTT toxicity is a reduction in mHTT expression. We know that mHTT expression is highly predictive of IB formation and neuron toxicity. Thus, we wondered if HSF1, through inducing chaperones that function in chaperone-mediated degradation or other means, could destabilize mHTT. Because we used HTT-EGFP fusion proteins in our longitudinal experiments, we were able to measure EGFP fluorescence and use it as a surrogate for HTT expression level. Mean EGFP fluorescence was extracted from individual cells whose boundaries had been outlined during our automated survival analysis (Fig. 25f). We used the single cell fluorescence data from the first time point, approximately 24 hours post-transfection, to generate a density function for each condition and tested the likelihood that the fluorescence data was drawn from the same distribution. This is the most sensitive way we know of to compare potentially non-gaussian distributed expression data. In this case, although expression differences were detected between normal and mHTT, as we would expect, HSF1 and HSF1-R71G had no effect on mHTT expression.

E
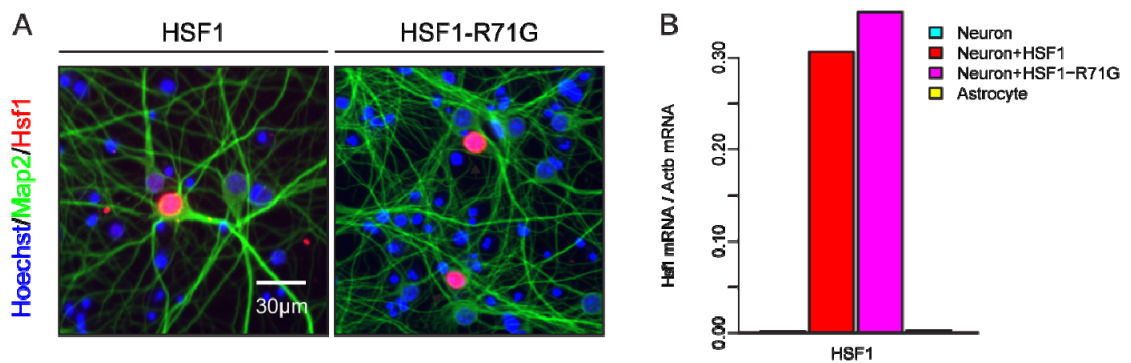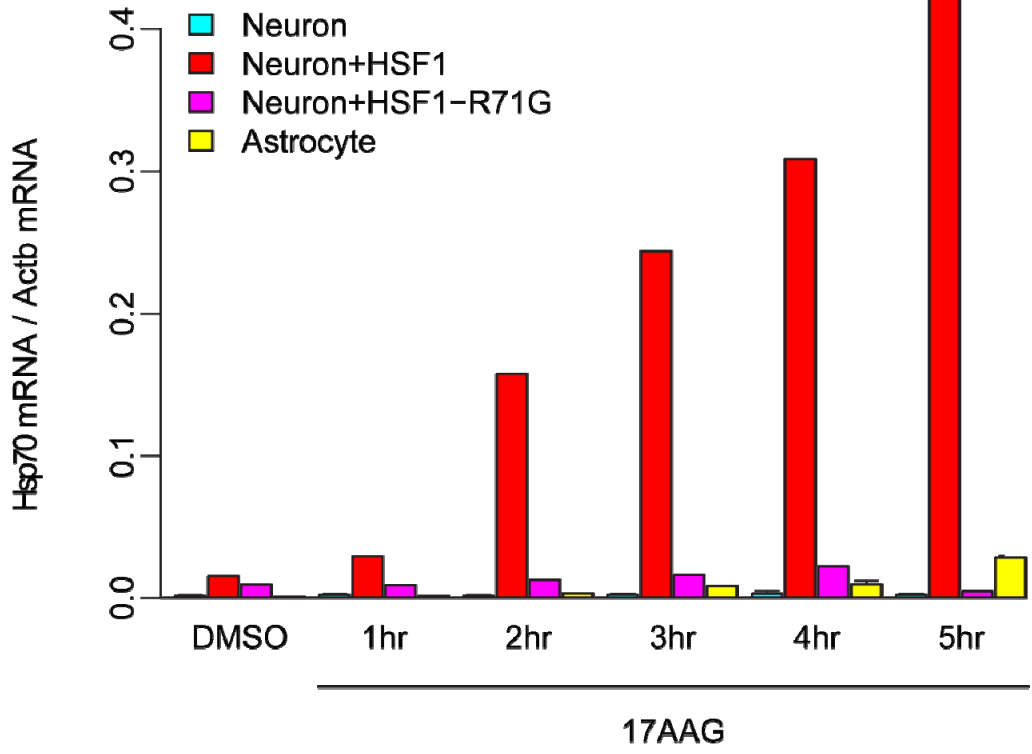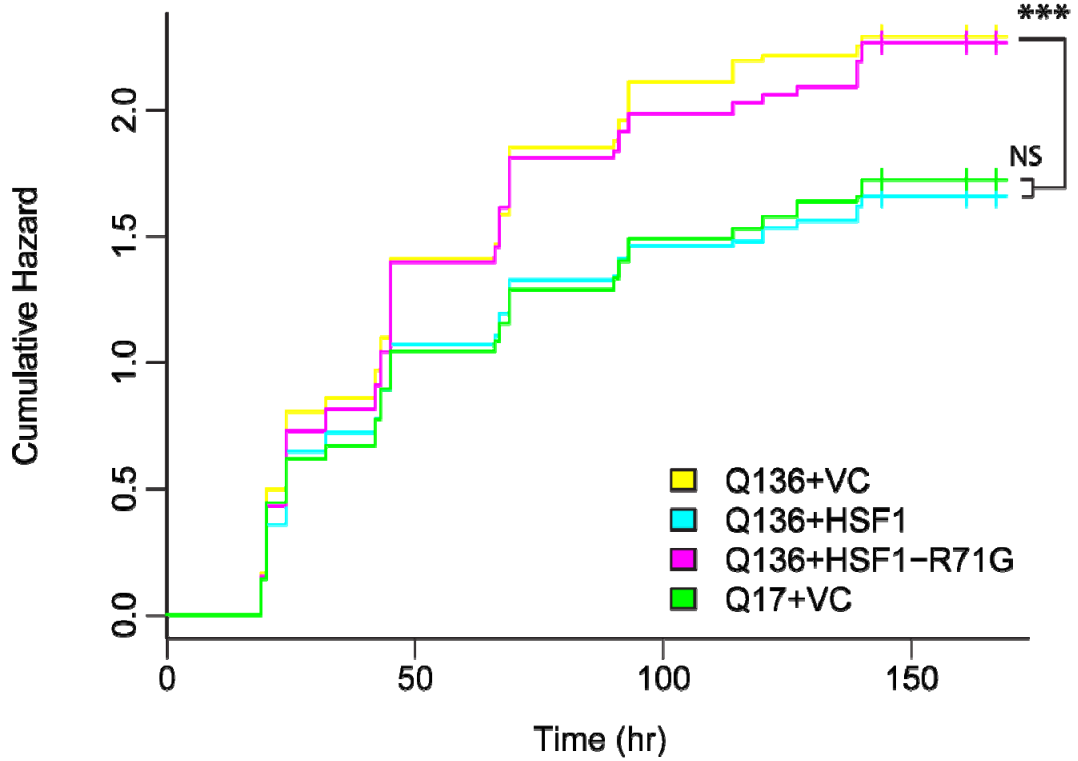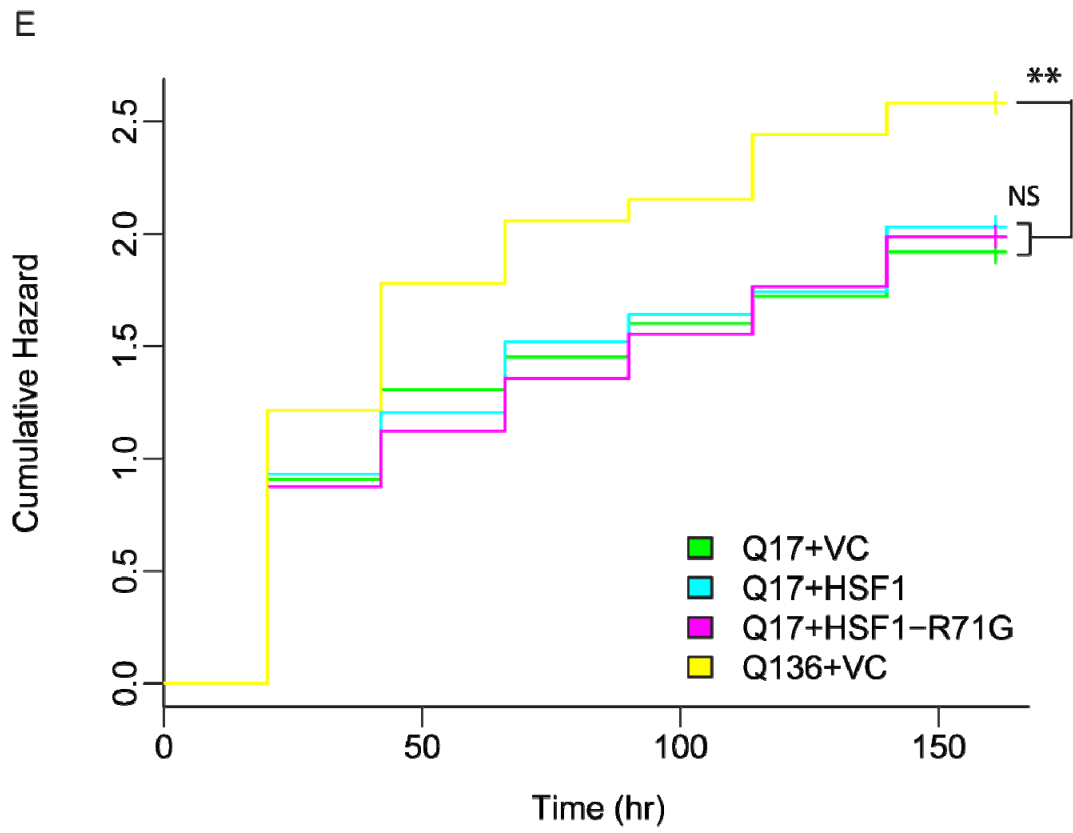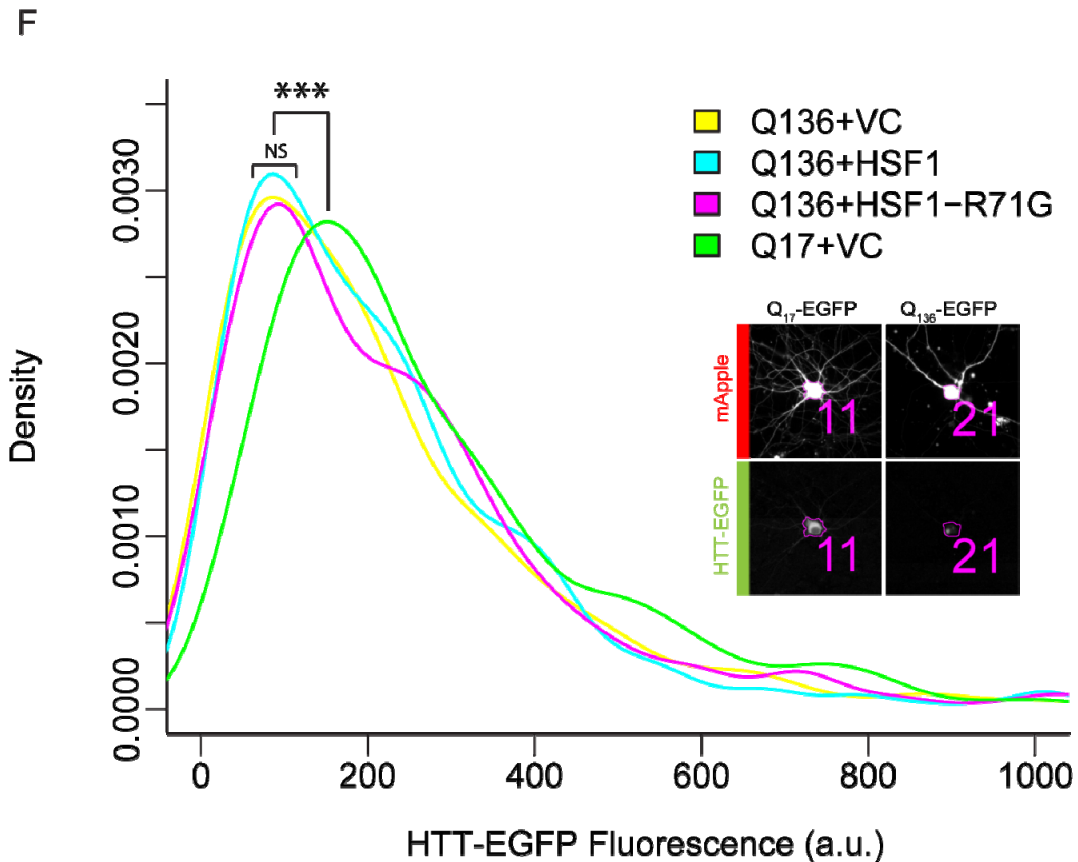
Figure 25. HSF1 restores the Hsp70 response in neurons and protects against malformed protein. (A) Viral overexpression (O.E.) of human HSF1 or a version of HSF1 (HSF1-R71G) that contains a single amino acid change in the DNA binding domain of the molecule, which renders it incompetent to bind to DNA, produce measurable levels of both versions of HSF1 in cortical neurons that are nuclear localized. Neurons were transduced on day *in vitro* 5 (DIV5) and subjected to immunocytochemistry on DIV12. Neurons were labeled with Hsf1 and Map2. Fluorescence from Alexa 555 and Alexa 488-conjugated secondary antibodies was collected with wide-field microscopy. (B) HSF1 and HSF1-R71G transcripts are largely increased compared to endogenous Hsf1 in neurons and astrocytes as measured by qRT-PCR. (C) O.E. of HSF1 restores the neuronal

endogenous Hsp70 (Hspa1a) response when treated with 17-AAG for 1, 2, 3, 4, or 5 hours. O.E. of HSF1-R71G had only a partial effect and experienced greater feedback inhibition. Total RNA was collected from cells immediately after drug treatment and cDNA was subjected to qRT-PCR as previously described. (D) HSF1 O.E. abrogates the toxicity of a 586 aa fragment of HTT with a disease-associated polyQ expansion (HTT^{586}-Q$_{136}$-EGFP). At DIV4, neurons were transfected with either HTT^{586}-Q$_{136}$-EGFP or a version of HTT with a polyQ repeat within the normal range (HTT^{586}-Q$_{17}$-EGFP) along with a co-transfection fluorescence marker (mApple). Either HSF1, HSF1-R71G or empty vector (VC) was co-transfected with HTT^{586}-Q$_{136}$-EGFP in order to assess the effect of HSF1 on cells coping with expanded polyQ HTT. Starting on DIV5, 24 hours after transfection, cells were subjected to longitudinal imaging on our robotic microcope. Cells were imaged in the red (mApple cell marker) channel and green (HTT) channel once every day for 7 days. The raw images were processed with a fully automated image analysis pipeline that longitudinally tracked cells and assigned each cell a time of death. Cumulative hazard curves were generated from the survival times of individual neurons (n>2000). A Cox Proportional Hazard (CPH) model was fit to the data and conditions were compared using HTT^{586}-Q$_{136}$-EGFP + VC as the reference. Hazard ratio (HR) ± 95% CI for Q$_{17}$+VC=0.745±0.097***, HR(Q$_{136}$+HSF1)=0.765±0.103*** and HR(Q$_{136}$+HSF1-R71G)=0.974±0.128^{NS}. (E) HSF1 O.E. has no effect on cells expressing HTT with a polyQ repeat within the normal range. As in (D), cumulative hazard curves were generated from individual neuron survival times (n=725). Using HTT^{586}-Q$_{17}$-

EGFP + VC as the reference, $HR(Q_{17}+HSF1)=1.024\pm0.227^{NS}$, $HR(Q_{17}+HSF1-R71G)=0.979\pm0.212^{NS}$ and $HR(Q_{136}+VC)=1.330\pm0.285^{**}$. Significance calculated from the coefficient of the covariate in the CPH model. (F) HSF1 abrogation of HTT^{586}-Q_{136}-EGFP toxicity cannot be attributed to destabilizing the mutant protein. EGFP fluorescence intensity was automatically extracted from cells at 24 hours post-transfection and used as a surrogate for HTT expression. Density plots were generated from fluorescence and a two-sample Kolmogorov-Smirnov (KS) test was used to compare conditions. P-values were adjusted by the holm method for multiple comparisons. $KS_D(Q_{136}, Q_{17})=0.1664^{***}$, $KS_D(Q_{136}, Q_{136}+HSF1)=0.040^{NS}$ and $KS_D(Q_{136}, Q_{136}+HSF1-R71G)=0.061^{NS}$. $p<0.001$ (***), $p<0.01$ (**), $p>0.05$ (NS).

HSF1 is not activated appreciably in neurons

From these data, we knew that increasing HSF1 levels was sufficient to restore a deficient stress response in neurons. We reasoned that this meant all the necessary activating machinery is present in neurons to induce HSF1 targets in response to stress, including the requirement for DNA accessibility, histone displacement and recruitment of elongation factors. However, this does not preclude the existence of negative regulation in neurons that could inhibit the already low levels of HSF1 and further attenuate the response. One sign of HSF1 activation is nuclear enrichment. We tested whether neurons and astrocytes showed differences at this upstream step of the acute stress response by exposing cells to either 37°C or 42°C HS and subjected them to

immunocytochemistry to quantify HSF1 in the nucleus (Fig. 26a). Astrocytes showed the expected accumulation of HSF1 within the nucleus after HS, however, neurons did not show similar enrichment (Fig. 26b). Since the major source of negative HSF1 regulation is binding to Hsp90, which keeps HSF1 in an inactivating complex, we thought that high levels of Hsp90 in neurons might make it particularly challenging to activate HSF1, especially when combined with low HSF1 expression. We performed qRT-PCR to measure transcript levels of Hsp90 (Hsp90aa1) in neurons and astrocytes and blotted cell extracts to measure Hsp90 protein. We found that neurons had significantly higher levels of Hsp90 for both transcript and protein (Fig. 26c,d). We therefore conclude that the distinct balance between high expression of Hsp90 and low expression of Hsf1 makes it particularly challenging for neurons to increase the concentration of inducible chaperones in a stress-dependent manner as part of the acute stress response. Neurons might rely instead on high expression of constitutive chaperones, such as Hsp90 and Hsc70, to buffer both transient and chronic cellular stresses.

A

	Neuron (Map2)	Astrocyte (Gfap)

Hoechst\Hsf1

Hsf1

20μm   20μm

B

Hsf1 Nuclear Intensity / Nuclear Intensity at 37°C

- Neuron
- Astrocyte

***

***

37°C   42°C
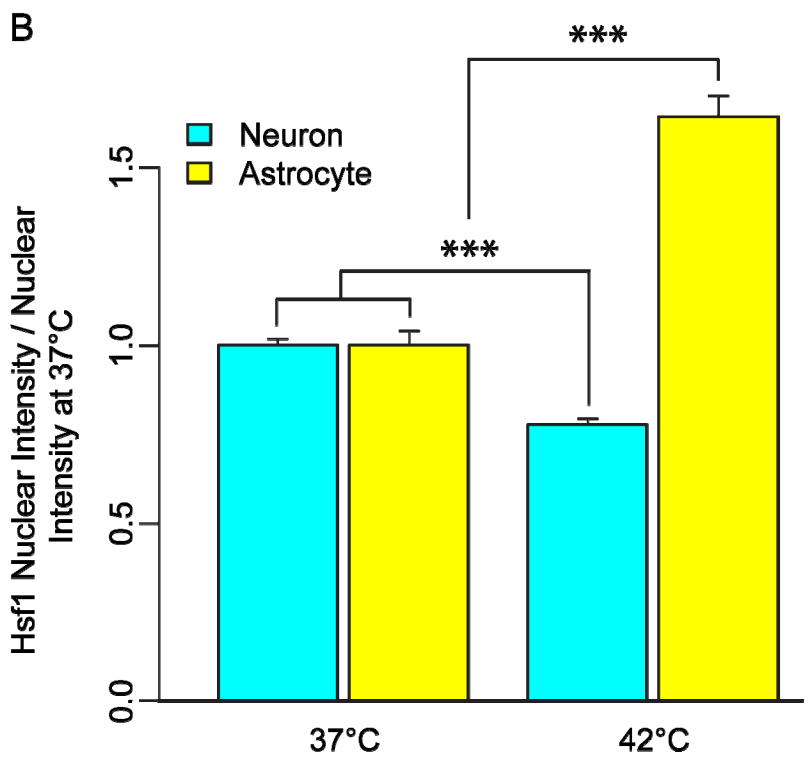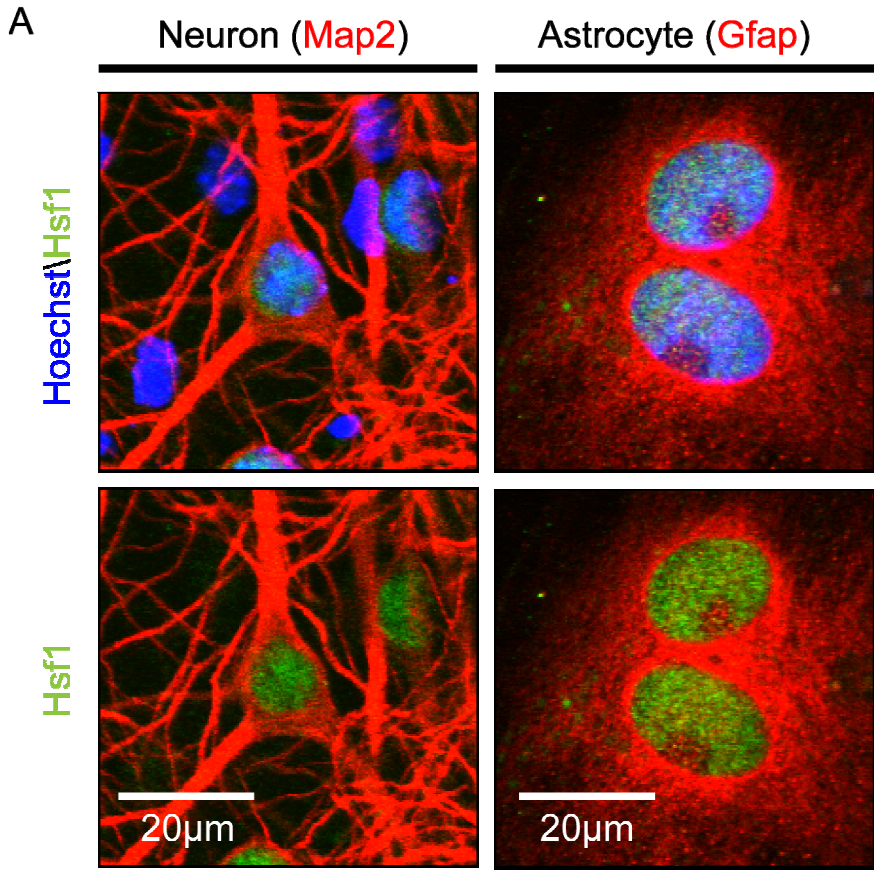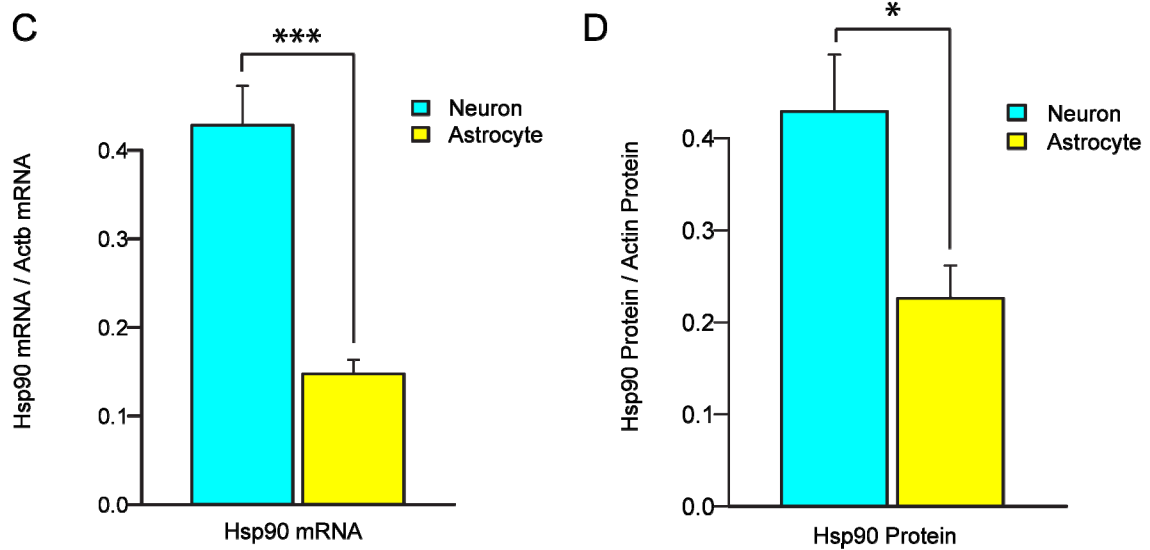
Figure 26. In neurons, HSF1 does not accumulate in the nucleus after thermal stress. Cortical neurons at 12DIV or Astrocytes 2 days post-LME treatment were exposed to either 37°C or 42°C HS for 3 hours. The cells were immediately fixed and subjected to immunocytochemistry. Fluorescence from Alexa 647 (green) and Alexa 555 (red) conjugated secondary antibodies to detect Hsf1 (Cell Signaling #4356) and either Map2 for neurons or Gfap for astrocytes was collected with confocal microscopy. Hoechst stain (blue) was used to detect nuclei. (A) Representative image of nuclear Hsf1 staining at 37°C in neurons and astrocytes. The nuclear compartment was identified by Hoechst stain and mean Hsf1 fluorescence was measured (n>30 for each condition). (B) Hsf1 fluorescence at 37°C and 42°C HS was normalized to the mean fluorescence for each cell type at 37°C. Nuclear enrichment after HS, a sign of HSF1 activation, occurs in astrocytes, but not in neurons. (C-D) Expression of Hsp90, a negative regulator of Hsf1 activation, was compared between the two cell types. (C) Hsp90 (Hsp90aa1) transcript abundance was measured relative to

β-Actin (Actb) by qRT-PCR. Error bars indicate s.e.m for 6 biological replicates. (D) The higher Hsp90 expression seen at the transcript level also occurs for Hsp90 protein. Error bars indicate s.e.m for 3 biological replicates. For all plots, significance was calculated by Student's two sample t-test. $p < 0.001$ (***), $p < 0.05$ (*).

Chapter 6

Conclusion

In the preceding work, we have described the novel construction of an automated microscope system that is capable of capturing longitudinal, multi-wavelength fluorescence data from thousands of cells and extracting dynamic, multi-parametric information to build predictive models of neurodegenerative disease. No prior system had the throughput and automated analysis capabilities to seamlessly link the process from start to finish. As a result, we have been able to complete, for the first time, image based drug screens in our lab. Through acquisition scripts, the system uses a robotic arm to load microtiter plates onto the microscope stage. The plate is registered using a fiduciary mark etched into the bottom of each plate, and fluorescence from 1-4 non-overlapping spectral bands or channels is captured consecutively from each well of a 96-well plate. Within each well, a grid of contiguous images is acquired for each channel. The system is capable of acquiring ~25,000 images, corresponding to ~45,000 neurons in 2 channels, in a single day. Subsequent automated analysis routines perform background correction on the images, stitch them together into larger montage images and align all time points. Cells are then tracked and longitudinal fluorescence data is extracted from single cells. Our current analysis pipeline can process a full longitudinal experiment with 2 channels and 7 time points in about 12 hours on an Intel Xeon 2.4GHz Dual quad core data analysis workstation. In order to validate the system, we compared the cumulative hazard curves generated from the unaltered output of the automated analysis to manual cell

counting and tracking. For an example experiment involving Nrf2 rescue of α-synuclein toxicity, the automated analysis was able to replicate the hazard ratio between α-synuclein+Nrf2 and α-synuclein+empty vector. In subsequent validation steps that tested the feasibility of using automated analysis for a screen, positive and negative controls were reliably identified with a PPV=91% and NPV=97%.

One of the primary goals in this work was to monitor the acute stress response in neurons and determine how this response might differ from other closely related cell types. Neurodegenerative disorders including AD, PD, HD and ALS show the most striking pathological features, including cell loss and dysfunction, in neurons. Despite widespread expression of the disease-associated protein, why are neurons differentially affected? One explanation is that the homeostatic responses in neurons are less adept at managing the metastable, aggregation-prone proteins present in these diseases. Previous studies have shown that neurons have decreased basal flux through the UPS and an attenuated Hsp70 response to thermal stress compared to glial cells (Tydlacka et al., 2008; Marcuccilli et al., 1996). These deficiencies may account for the specific accumulation of malformed protein within neurons. However, our data do not allow us to conclude that the responses in neurons are universally deficient. Cellular proteostasis is maintained by a dynamic and highly regulated system with many sensors and effectors. The existence of multiple forms of crosstalk between refolding and degradation pathways brings up the possibility that neurons have a different response, not a universally deficient response(Pandey

et al., 2007; Korolchuk et al., 2010; Lecomte et al., 2010; Vos et al., 2010). Indeed, there is evidence that cell type specific regulation of cellular proteostasis pathways has co-evolved with the unique proteome that each cell has to maintain(Powers and Balch, 2013).

In order to study the acute stress response in neurons, we isolated primary neurons or astrocytes from mouse brains. We showed that neurons have no significant Hsp70 response to mHTT, whereas astrocytes showed Hsp70 induction along with specific Hsp70 enrichment around sites of IB formation. We then performed a series of experiments to show that neurons have a deficient HSR when subjected to thermal stress. Importantly, we measured induction of mRNA and protein at multiple known targets of the HSR including Hsp70, Hsp40, Hsp90 and Hsp27. In each case, neurons showed decreased induction when compared to astrocytes, suggesting that the deficiency in neurons cannot be attributed to a regulatory difference at the Hsp70 locus alone. It rather pointed to a difference in the master HSR transcriptional regulator, HSF1. The deficiency also extended to other known proteotoxic stresses including Hsp90 and proteasome inhibition, suggesting that the measured differences represent a more fundamental difference in how neurons respond to stress, irrespective of the particular stimulus.

Until this work, the mechanism for the reduced HSR in neurons has been controversial and unresolved. One study concluded that hippocampal neurons lacked appreciable Hsp70 induction after exposure to thermal stress because they had low expression of HSF1(Marcuccilli et al., 1996). However, this

112

hypothesis was not tested by HSF1 overexpression (O.E.). We also showed that cortical neurons have low expression of HSF1, and we were further able to rescue the HSR using viral O.E. of HSF1. We demonstrated the functional significance of restoration of HSF1 expression levels in neurons by showing that HSF1 was able to abrogate neuronal mHTT toxicity. These data indicate that with sufficient levels of HSF1, neurons have the intracellular machinery necessary to respond to various stressors and generate HSF1-mediated responses, which require HSF1 activation, DNA-binding and transactivation of target genes.

In contrast to our findings, a second study could only rescue the response in motor neurons with a constitutively active form of HSF1, but not normal HSF1(Batulan et al., 2003). The constitutively active form of HSF1 had been created by deletion of a region within HSF1 corresponding to amino acids 202-316. This stretch contains multiple serine residues, including S230, S303 and S307, whose posttranslational modification state influences activation of HSF1(Knauf et al., 1996; Kline and Morimoto, 1997; Chu et al., 1996; Hietakangas et al., 2003). Under non-stressed conditions, phosphorylation at S307 by mitogen-activated protein kinase (MAPK) promotes phosphorylation at S303 by glycogen synthase kinase 3 β. Within HSF1, S303 is located within a phosphorylation dependent sumoylation motif (PDSM), where P-S303 promotes sumoylation of HSF1 at K298, which ultimately inhibits the transactivation potential of HSF1. Because the neuronal HSR was rescued by deletion of this inhibitory region within HSF1, the authors postulated that the deficiency was explained by a difference in regulation of HSF1 at these serine residues. We

used mass spectrometry to detect posttranslational modifications of endogenous HSF1 in neurons and astrocytes and showed that P-S303 and P-S307 exist in both cell types under non-stressed conditions, suggesting that the difference in the HSR in neurons and astrocytes can not be attributed to constitutive differences in HSF1 phosphorylation at these residues. We are therefore pursuing the hypothesis that lack of disinhibition in neurons may be responsible for the deficient HSR.

Our data showing that HSF1 O.E. rescues the HSR in neurons does not exclude differences in regulation of HSF1. We showed that neurons have high expression of the constitutive chaperone Hsp90 leading to increased sequestration of HSF1 into an inactive monomer. Through O.E. we are likely overwhelming negative regulation of HSF1 by Hsp90 and other endogenous signaling pathways such as the MAPK/ERK pathway and Ubc9, which sumoylates HSF1. If indeed there are regulatory differences in neurons involving kinase signaling, it would lead to the exciting possibility of targeted therapeutics that directly address the HSR deficit in neurons.

In conclusion, we have proposed a mechanism for the attenuated HSR in neurons as a combination between high levels of Hsp90 and relatively low levels of the major stress responsive transcriptional regulator HSF1 (Fig. 27). In addition to low levels of HSF1, neurons show decreased levels of HSF2, another heat shock factor that coordinates with HSF1 to influence the HSR. The contribution of HSF2 is most notable when the UPS is impaired(Mathew et al., 1998; Ostling et al., 2007). Neurons, however, seemingly have high basal

homeostatic buffering capability due to the high expression of two major constitutive chaperons, Hsp90 and Hsc70. This might better protect neurons from chronic stresses, including coping with malformed protein over the course of their lifetime. However, it decreases the ability of neurons to respond acutely to transient stresses that overwhelm their constitutive chaperoning capabilities. This may explain why neurodegenerative diseases are late onset. Neurons are able to cope under most conditions with disease-associated, metastable proteins. However, during acute cell-intrinsic or environmental stresses, neurons are perturbed outside of their homeostatic envelope. If this state persists, neurons may become dysfunctional or die, or they may institute other coping strategies such as IB formation. This agrees well with the one-hit theory for neurodegenerative disease, which says that neurons have a very similar risk of death throughout their lifetime when coping with the disease-associated protein (e.g. disease does not result from cumulative toxicity)(Clarke et al., 2000). Disease manifests in the affected individual only when the number of cells experiencing cellular death and dysfunction, perhaps due to protein dyshomeostasis, have increased above a certain threshold leading to more global network dysfunction. We conclude that enhancing proteostasis in neurons through increasing their ability to cope with acute proteotoxic stresses is a valid therapeutic approach in HD and other neurodegenerative disorders of protein conformation.
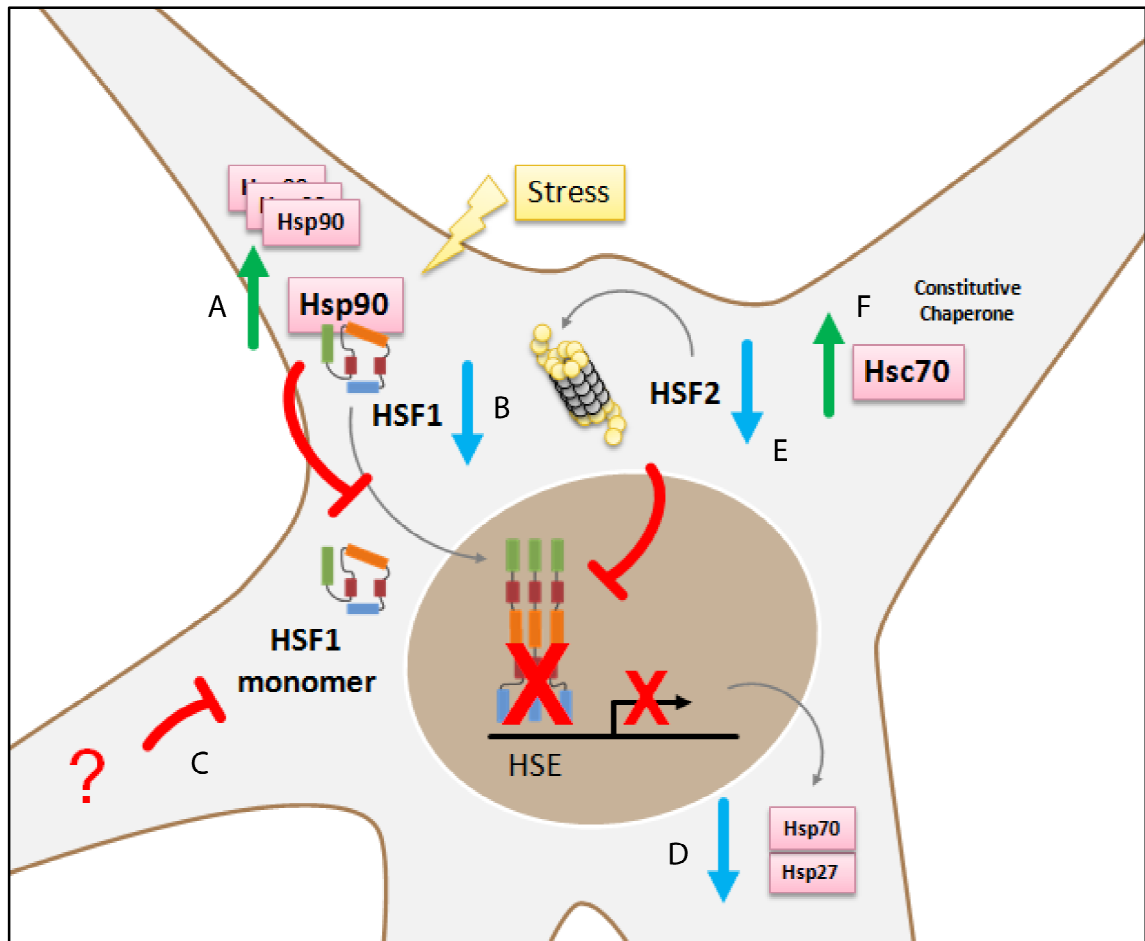
Figure 27. Proposed mechanisms for the attenuated HSR in neurons. (A) High expression of Hsp90, a constitutive chaperone that sequesters monomeric HSF1 in an inactivating complex. (B) Decreased expression of HSF1, the major stress-responsive transcriptional regulator. (C) Inability of HSF1 monomer to be activated through posttranslational modification changes, potentially including decreased disinhibition by persistent phosphorylation at S303 and S307. (D) The attenuated HSR results in decreased expression of Hsp70 and Hsp27, two major inducible chaperones. (E) Increased turnover of HSF2 through the UPS. (F) High expression of the constitutive chaperone Hsc70, which increases chronic

chaperone activity, but can also inhibit HSF1, although to a lesser extent than Hsp90.

References

Abraham VC, Towne DL, Waring JF, Warrior U, Burns DJ (2008) Application of a high-content multiparameter cytotoxicity assay to prioritize compounds based on toxicity potential in humans. J Biomol Screen 13:527-37.

Adams CP, Brantner VV (2006) Estimating the cost of new drug development: Is it really 802 million dollars? Health Affairs (Project Hope) 25:420-8.

Ai H, Shaner NC, Cheng Z, Tsien RY, Campbell RE (2007) Exploration of new chromophore structures leads to the identification of improved blue fluorescent proteinsâ€ . Biochemistry 46:5904-5910.

Akerfelt M, Morimoto RI, Sistonen L (2010) Heat shock factors: Integrators of cell stress, development and lifespan. Nat Rev Mol Cell Biol 11:545-55.

Akerfelt M, Trouillet D, Mezger V, Sistonen L (2007) Heat shock factors at a crossroad between stress and development. Ann N Y Acad Sci 1113:15-27.

Allan C et al (2012) OMERO: Flexible, model-driven data management for experimental biology. Nat Methods (United States) 9:245-253.

Altar CA, Cai N, Bliven T, Juhasz M, Conner JM, Acheson AL, Lindsay RM, Wiegand SJ (1997) Anterograde transport of brain-derived neurotrophic factor and its role in the brain. Nature 389:856-860.

Anckar J, Sistonen L (2011) Regulation of HSF1 function in the heat stress response: Implications in aging and disease. Annual Review of Biochemistry 80:1089-1115.

Andrew S, Goldberg Y, Kremer B, Telenius H, Theilmann J, Adam S, Starr E, Squitieri F, Lin B, Kalchman M (1993) The relationship between trinucleotide (CAG) repeat length and clinical features of huntington's disease. Nature Genetics 4:398-403.

Arrasate M, Finkbeiner S (2005) Automated microscope system for determining factors that predict neuronal fate. Proc Natl Acad Sci U S A 102:3840-5.

Arrasate M, Mitra S, Schweitzer ES, Segal MR, Finkbeiner S (2004) Inclusion body formation reduces levels of mutant huntingtin and the risk of neuronal death. Nature 431:805-10.

Aubin JE (1979) Autofluorescence of viable cultured mammalian cells. J Histochem Cytochem (UNITED STATES) 27:36-43.

Baquet ZC, Gorski JA, Jones KR (2004) Early striatal dendrite deficits followed by neuron loss with advanced age in the absence of anterograde cortical brain-derived neurotrophic factor. The Journal of Neuroscience 24:4250-4258.

Batulan Z, Shinder GA, Minotti S, He BP, Doroudchi MM, Nalbantoglu J, Strong MJ, Durham HD (2003) High threshold for induction of the stress response in

motor neurons is associated with failure to activate HSF1. J Neurosci 23:5789-98.

Bauer PO, Goswami A, Wong HK, Okuno M, Kurosawa M, Yamada M, Miyazaki H, Matsumoto G, Kino Y, Nagai Y, Nukina N (2010) Harnessing chaperone-mediated autophagy for the selective degradation of mutant huntingtin protein. Nat Biotechnol .

Bennett EJ, Bence NF, Jayakumar R, Kopito RR (2005) Global impairment of the ubiquitin-proteasome system by nuclear or cytoplasmic protein aggregates precedes inclusion body formation. Mol Cell 17:351-65.

Bennett EJ, Shaler TA, Woodman B, Ryu KY, Zaitseva TS, Becker CH, Bates GP, Schulman H, Kopito RR (2007) Global changes to the ubiquitin system in huntington's disease. Nature 448:704-8.

Bhattacharyya A, Thakur AK, Chellgren VM, Thiagarajan G, Williams AD, Chellgren BW, Creamer TP, Wetzel R (2006) Oligoproline effects on polyglutamine conformation and aggregation. J Mol Biol 355:524-35.

Borowiak M, Maehr R, Chen S, Chen AE, Tang W, Fox JL, Schreiber SL, Melton DA (2009) Small molecules efficiently direct endodermal differentiation of mouse and human embryonic stem cells. Cell Stem Cell 4:348-58.

Cattaneo E, Zuccato C, Tartari M (2005) Normal huntingtin function: An alternative approach to huntington's disease. Nature Reviews 6:919-30.

Charles AC, Merrill JE, Dirksen ER, Sanderson MJ (1991) Intercellular signaling in glial cells: Calcium waves and oscillations in response to mechanical stimulation and glutamate. Neuron (UNITED STATES) 6:983-992.

Chen X, Zhou X, Wong ST (2006) Automated segmentation, classification, and tracking of cancer cell nuclei in time-lapse microscopy. Biomedical Engineering, IEEE Transactions On 53:762-766.

Chu B, Soncin F, Price BD, Stevenson MA, Calderwood SK (1996) Sequential phosphorylation by mitogen-activated protein kinase and glycogen synthase kinase 3 represses transcriptional activation by heat shock factor-1. J Biol Chem 271:30847-30857.

Ciechanover A, Brundin P (2003) The ubiquitin proteasome system in neurodegenerative diseases: Sometimes the chicken, sometimes the egg. Neuron 40:427-46.

Clarke G, Collins RA, Leavitt BR, Andrews DF, Hayden MR, Lumsden CJ, McInnes RR (2000) A one-hit model of cell death in inherited neuronal degenerations. Nature 406:195-9.

Cohen AA, Geva-Zatorsky N, Eden E, Frenkel-Morgenstern M, Issaeva I, Sigal A, Milo R, Cohen-Saidon C, Liron Y, Kam Z, Cohen L, Danon T, Perzov N, Alon U (2008) Dynamic proteomics of individual cancer cells in response to a drug. Science 322:1511-1516.

Daub A, Sharma P, Finkbeiner S (2009) High-content screening of primary neurons: Ready for prime time. Current Opinion in Neurobiology 19:537-543.

Davies S, Turmaine M, Cozens B, DiFiglia M, Sharp A, Ross C, Scherzinger E, Wanker E, Mangiarini L, Bates G (1997) Formation of neuronal intranuclear inclusions underlies the neurological dysfunction in mice transgenic for the HD mutation. Cell 90:537-548.

Dehay B, Bertolotti A (2006) Critical role of the proline-rich region in huntingtin for aggregation and cytotoxicity in yeast. J Biol Chem 281:35608-15.

Di Giorgio FP, Carrasco MA, Siao MC, Maniatis T, Eggan K (2007) Non-cell autonomous effect of glia on motor neurons in an embryonic stem cell-based ALS model. Nature Neuroscience 10:608-14.

DiFiglia M (1997) Aggregation of huntingtin in neuronal intranuclear inclusions and dystrophic neurites in brain. Science 277:.

Dimos JT, Rodolfa KT, Niakan KK, Weisenthal LM, Mitsumoto H, Chung W, Croft GF, Saphier G, Leibel R, Goland R, Wichterle H, Henderson CE, Eggan K (2008) Induced pluripotent stem cells generated from patients with ALS can be differentiated into motor neurons. Science (New York, N Y 321:1218-21.

Doil C, Mailand N, Bekker-Jensen S, Menard P, Larsen DH, Pepperkok R, Ellenberg J, Panier S, Durocher D, Bartek J, Lukas J, Lukas C (2009) RNF168

binds and amplifies ubiquitin conjugates on damaged chromosomes to allow accumulation of repair proteins. Cell 136:435-46.

Duff K, Paulsen JS, Beglinger LJ, Langbehn DR, Stout JC (2007) Psychiatric symptoms in huntington's disease before diagnosis: The predict-HD study. Biol Psychiatry 62:1341-1346.

Duyao M, Ambrose C, Myers R, Novelletto A, Persichetti F, Frontali M, Folstein S, Ross C, Franz M, Abbott M (1993) Trinucleotide repeat length instability and age of onset in huntington's disease. Nat Genet 4:387-392.

Ebert AD, Yu J, F. RF,Jr, Mattis VB, Lorson CL, Thomson JA, Svendsen CN (2009) Induced pluripotent stem cells from a spinal muscular atrophy patient. Nature 457:277-80.

Eglen RM, Gilchrist A, Reisine T (2008) An overview of drug screening using primary and embryonic stem cells. Combinatorial Chemistry & High Throughput Screening 11:566-72.

Erfle H, Neumann B, Liebel U, Rogers P, Held M, Walter T, Ellenberg J, Pepperkok R (2007) Reverse transfection on cell arrays for high content screening microscopy. Nature Protocols 2:392-9.

Erfle H, Neumann B, Rogers P, Bulkescher J, Ellenberg J, Pepperkok R (2008) Work flow for multiplexing siRNA assays by solid-phase reverse transfection in multiwell plates. J Biomol Screen 13:575-580.

Fernandes M, Xiao H, Lis JT (1994) Fine structure analyses of the drosophila and saccharomyces heat shock factor--heat shock element interactions. Nucleic Acids Res 22:167-73.

Francis OW (2007) Huntington's disease. The Lancet 369:.

Friedman A, Perrimon N (2007) Genetic screening for signal transduction in the era of network biology. Cell 128:225-31.

Gafni J, Hermel E, Young JE, Wellington CL, Hayden MR, Ellerby LM (2004) Inhibition of calpain cleavage of huntingtin reduces toxicity: Accumulation of calpain/caspase fragments in the nucleus. J Biol Chem 279:20211-20.

Gauthier LR, Charrin BC, Borrell-Pagès M, Dompierre JP, Rangone H, Cordelières FP, De Mey J, MacDonald ME, Leßmann V, Humbert S (2004) Huntingtin controls neurotrophic support and survival of neurons by enhancing BDNF vesicular transport along microtubules. Cell 118:127-138.

Ghosh A, Carnahan J, Greenberg ME (1994) Requirement for BDNF in activity-dependent survival of cortical neurons. Science 263:1618-1623.

Giepmans BNG, Adams SR, Ellisman MH, Tsien RY (2006) The fluorescent toolbox for assessing protein location and function. Science 312:217-224.

Giuliano KA, Taylor DL (1998) Fluorescent-protein biosensors: New tools for drug discovery. Trends in Biotechnology 16:135-40.

Giuliano KA, DeBiasio RL, Dunlay RT, Gough A, Volosky JM, Zock J, Pavlakis GN, Taylor DL (1997) High-content screening: A new approach to easing key bottlenecks in the drug discovery process. J Biomol Screen 2:249-259.

Glory E, Murphy RF (2007) Automated subcellular location determination and high-throughput microscopy. Developmental Cell 12:7-16.

Goldberg Y, Kalchman M, Metzler M, Nasir J, Zeisler J, Graham R, Koide H, O'Kusky J, Sharp A, Ross C (1996) Absence of disease phenotype and intergenerational stability of the CAG repeat in transgenic mice expressing the human huntington disease transcript. Hum Mol Genet 5:177-185.

Graham RK, Deng Y, Slow EJ, Haigh B, Bissada N, Lu G, Pearson J, Shehadeh J, Bertram L, Murphy Z, Warby SC, Doty CN, Roy S, Wellington CL, Leavitt BR, Raymond LA, Nicholson DW, Hayden MR (2006) Cleavage at the caspase-6 site is required for neuronal dysfunction and degeneration due to mutant huntingtin. Cell 125:1179-1191.

Halterman MW, Giuliano R, Dejesus C, Schor NF (2009) In-tube transfection improves the efficiency of gene transfer in primary neuronal cultures. J Neurosci Methods (Netherlands) 177:348-354.

Hamby M, Uliasz T, Hewett S, Hewett J (2006) Characterization of an improved procedure for the removal of microglia from confluent monolayers of primary astrocytes. Journal of Neuroscience Methods 150:128-137.

Harder N, Mora-Bermudez F, Godinez WJ, Wunsche A, Eils R, Ellenberg J, Rohr K (2009) Automatic analysis of dividing cells in live cell movies to detect mitotic delays and correlate phenotypes in time. Genome Research .

Hawkins KR, Yager P (2003) Nonlinear decrease of background fluorescence in polymer thin-films - a survey of materials and how they can complicate fluorescence detection in microTAS. Lab Chip (England) 3:248-252.

Hay DG, Sathasivam K, Tobaben S, Stahl B, Marber M, Mestril R, Mahal A, Smith DL, Woodman B, Bates GP (2004) Progressive decrease in chaperone protein levels in a mouse model of huntington's disease and induction of stress proteins as a therapeutic approach. Hum Mol Genet 13:1389-405.

Hietakangas V, Ahlskog J, Jakobsson A, Hellesuo M, Sahlberg N, Holmberg C, Mikhailov A, Palvimo J, Pirkkala L, Sistonen L (2003) Phosphorylation of serine 303 is a prerequisite for the stress-inducible SUMO modification of heat shock factor 1. Molecular and Cellular Biology 23:2953-2968.

Hipp MS, Patel CN, Bersuker K, Riley BE, Kaiser SE, Shaler TA, Brandeis M, Kopito RR (2012) Indirect inhibition of 26S proteasome activity in a cellular model of huntington's disease. J Cell Biol 196:573-87.

Humbert S, Bryson EA, Cordelieres FP, Connors NC, Datta SR, Finkbeiner S, Greenberg ME, Saudou F (2002) The IGF-1/akt pathway is neuroprotective in huntington's disease and involves huntingtin phosphorylation by akt. Developmental Cell 2:831-7.

Huntington G (2004) On chorea. Landmarks in Medical Genetics: Classic Papers with Commentaries 51:4.

Ichikawa M, Muramoto K, Kobayashi K, Kawahara M, Kuroda Y (1993) Formation and maturation of synapses in primary cultures of rat cerebral cortical cells: An electron microscopic study. Neurosci Res 16:95-103.

Ivanova N, Dobrin R, Lu R, Kotenko I, Levorse J, DeCoste C, Schafer X, Lun Y, Lemischka IR (2006) Dissecting self-renewal in stem cells with RNA interference. Nature 442:533-8.

Jeong H, Then F, J. MT,Jr, Mazzulli JR, Cui L, Savas JN, Voisine C, Paganetti P, Tanese N, Hart AC, Yamamoto A, Krainc D (2009) Acetylation targets mutant huntingtin to autophagosomes for degradation. Cell 137:60-72.

Jervis GA (1963) Huntington's chorea in childhood. Arch Neurol 9:244.

Jones TR, Carpenter AE, Lamprecht MR, Moffat J, Silver SJ, Grenier JK, Castoreno AB, Eggert US, Root DE, Golland P, Sabatini DM (2009) Scoring diverse cellular morphologies in image-based screens with iterative feedback and machine learning. Proceedings of the National Academy of Sciences of the United States of America 106:1826-31.

Kaji K, Norrby K, Paca A, Mileikovsky M, Mohseni P, Woltjen K (2009) Virus-free induction of pluripotency and subsequent excision of reprogramming factors. Nature 458:771-5.

Kamioka H, Maeda E, Jimbo Y, Robinson HP, Kawana A (1996) Spontaneous periodic synchronized bursting during formation of mature patterns of connections in cortical cultures. Neurosci Lett 206:109-112.

Kim M, Chelliah Y, Kim S, Otwinowski Z, Bezprozvanny I (2009) Secondary structure of huntingtin amino-terminal region. Structure (London, England : 1993) 17:1205-1212.

Klein J, Moeschberger M (2003) Survival analysis: Techniques for censored and truncated data. 2003.

Kline M, Morimoto R (1997) Repression of the heat shock factor 1 transcriptional activation domain is modulated by constitutive phosphorylation. Molecular and Cellular Biology 17:2107-2115.

Knauf U, Newton EM, Kyriakis J, Kingston RE (1996) Repression of human heat shock factor 1 activity at control temperature by phosphorylation. Genes Dev 10:2782-2793.

Kola I, Landis J (2004) Can the pharmaceutical industry reduce attrition rates? Nature Reviews 3:711-5.

Korolchuk VI, Menzies FM, Rubinsztein DC (2010) Mechanisms of cross-talk between the ubiquitin-proteasome and autophagy-lysosome systems. FEBS Lett 584:1393-8.

Korolchuk VI, Mansilla A, Menzies FM, Rubinsztein DC (2009) Autophagy inhibition compromises degradation of ubiquitin-proteasome pathway substrates. Mol Cell 33:517-27.

Krausz E (2007) High-content siRNA screening. Molecular bioSystems 3:232-40.

Labbadia J, Cunliffe H, Weiss A, Katsyuba E, Sathasivam K, Seredenina T, Woodman B, Moussaoui S, Frentzel S, Luthi-Carter R, Paganetti P, Bates GP (2011) Altered chromatin architecture underlies progressive impairment of the heat shock response in mouse models of huntington disease. J Clin Invest .

Lang P, Yeow K, Nichols A, Scheer A (2006) Cellular imaging in drug discovery. Nature Reviews 5:343-56.

Lecomte S, Desmots F, Le Masson F, Le Goff P, Michel D, Christians E, Le Dréan Y (2010) Roles of heat shock factor 1 and 2 in response to proteasome inhibition: Consequence on p53 stability. Oncogene 29:4216-4224.

Lee SU, Yoon Chung S, Park RH (1990) A comparative performance study of several global thresholding techniques for segmentation. Computer Vision, Graphics, and Image Processing 52:171-190.

Lindquist S (1986) The heat-shock response. Annu Rev Biochem 55:1151-91.

Linkert M, Rueden CT, Allan C, Burel JM, Moore W, Patterson A, Loranger B, Moore J, Neves C, Macdonald D, Tarkowska A, Sticco C, Hill E, Rossner M,

Eliceiri KW, Swedlow JR (2010) Metadata matters: Access to image data in the real world. J Cell Biol 189:777-82.

Loh SH, Francescut L, Lingor P, Bahr M, Nicotera P (2008) Identification of new kinase clusters required for neurite outgrowth and retraction by a loss-of-function RNA interference screen. Cell Death and Differentiation 15:283-98.

Loo LH, Wu LF, Altschuler SJ (2007) Image-based multivariate profiling of drug responses from single cells. Nature Methods 4:445-53.

Lu B (2003) BDNF and activity-dependent synaptic modulation. Learning & Memory 10:86-98.

Lu B, Zheng S, Quach BQ, Tai YC (2010) A study of the autofluorescence of parylene materials for microTAS applications. Lab Chip (England) 10:1826-1834.

Luo S, Vacher C, Davies JE, Rubinsztein DC (2005) Cdk5 phosphorylation of huntingtin reduces its cleavage by caspases: Implications for mutant huntingtin toxicity. J Cell Biol 169:647-56.

MacDonald ME et al (1993) A novel gene containing a trinucleotide repeat that is expanded and unstable on huntington's disease chromosomes. Cell 72:971-983.

Magrassi L, Leto K, Rossi F (2013) Lifespan of neurons is uncoupled from organismal lifespan. Proceedings of the National Academy of Sciences of the United States of America 110:4374-4379.

Mangiarini L, Sathasivam K, Seller M, Cozens B, Harper A, Hetherington C, Lawton M, Trottier Y, Lehrach H, Davies S, Bates G (1996) Exon 1 of the HD gene with an expanded CAG repeat is sufficient to cause a progressive neurological phenotype in transgenic mice. Cell 87:493-506.

Marcuccilli C, Mathur S, Morimoto R, Miller R (1996) Regulatory differences in the stress response of hippocampal neurons and glial cells after heat shock. The Journal of Neuroscience : The Official Journal of the Society for Neuroscience 16:478-485.

Martinez-Vicente M, Talloczy Z, Wong E, Tang G, Koga H, Kaushik S, de Vries R, Arias E, Harris S, Sulzer D, Cuervo AM (2010) Cargo recognition failure is responsible for inefficient autophagy in huntington's disease. Nat Neurosci 13:567-76.

Mathew A, Mathur S, Morimoto R (1998) Heat shock response and protein degradation: Regulation of HSF2 by the ubiquitin-proteasome pathway. Molecular and Cellular Biology 18:5091-5098.

Meijering E, Smal I, Danuser G (2006) Tracking in molecular bioimaging. Signal Processing Magazine, IEEE 23:46-53.

Mendillo M, Santagata S, Koeva M, Bell G, Hu R, Tamimi R, Fraenkel E, Ince T, Whitesell L, Lindquist S (2012) HSF1 drives a transcriptional program distinct from heat shock to support highly malignant human cancers. Cell 150:549-562.

Miller J et al (2011) Identifying polyglutamine protein species in situ that best predict neurodegeneration. Nat Chem Biol .

Miller J, Arrasate M, Shaby BA, Mitra S, Masliah E, Finkbeiner S (2010a) Quantitative relationships between huntingtin levels, polyglutamine length, inclusion body formation, and neuronal death provide novel insight into huntington's disease molecular pathogenesis. J. Neurosci. 30:10541-10550.

Miller J, Arrasate M, Shaby B, Mitra S, Masliah E, Finkbeiner S (2010b) Quantitative relationships between huntingtin levels, polyglutamine length, inclusion body formation, and neuronal death provide novel insight into huntington's disease molecular pathogenesis. The Journal of Neuroscience : The Official Journal of the Society for Neuroscience 30:10541-10550.

Mitra S, Tsvetkov AS, Finkbeiner S (2009) Single neuron ubiquitin-proteasome dynamics accompanying inclusion body formation in huntington disease. J. Biol. Chem. 284:4398-4403.

Moeschberger ML, Klein JP (2003) Survival analysis: Techniques for censored and truncated data. Springer.

Morimoto RI (2008) Proteotoxic stress and inducible chaperone networks in neurodegenerative disease and aging. Genes Dev 22:1427-38.

Morimoto RI (1998) Regulation of the heat shock transcriptional response: Cross talk between a family of heat shock factors, molecular chaperones, and negative regulators. Genes Dev 12:3788-96.

Muchowski P, Schaffar G, Sittler A, Wanker E, Hayer-Hartl M, Hartl F (2000) Hsp70 and hsp40 chaperones can inhibit self-assembly of polyglutamine proteins into amyloid-like fibrils. Proceedings of the National Academy of Sciences of the United States of America 97:7841-7846.

Neumann B, Held M, Liebel U, Erfle H, Rogers P, Pepperkok R, Ellenberg J (2006) High-throughput RNAi screening by time-lapse imaging of live human cells. Nat Meth 3:385-390.

Nixon M, Aguado AS (2008) Feature extraction & image processing. Access Online via Elsevier.

Nolan GP (2007) What's wrong with drug screening today. Nature Chemical Biology 3:187-91.

Nopoulos PC, Aylward EH, Ross CA, Johnson HJ, Magnotta VA, Juhl AR, Pierson RK, Mills J, Langbehn DR, Paulsen JS (2010) Cerebral cortex structure in prodromal huntington disease. Neurobiol Dis 40:544-554.

Okita K, Nakagawa M, Hyenjong H, Ichisaka T, Yamanaka S (2008) Generation of mouse induced pluripotent stem cells without viral vectors. Science 322:949-953.

Orr H, Zoghbi H (2007) Trinucleotide repeat disorders. Annual Review of Neuroscience 30:575-621.

Ostling P, Bjork JK, Roos-Mattjus P, Mezger V, Sistonen L (2007) Heat shock factor 2 (HSF2) contributes to inducible expression of hsp genes through interplay with HSF1. J Biol Chem 282:7077-86.

Pan C, Kumar C, Bohl S, Klingmueller U, Mann M (2009) Comparative proteomic phenotyping of cell lines and primary cells to assess preservation of cell type-specific functions. Mol Cell Proteomics 8:443-50.

Pandey UB, Nie Z, Batlevi Y, McCray BA, Ritson GP, Nedelsky NB, Schwartz SL, DiProspero NA, Knight MA, Schuldiner O, Padmanabhan R, Hild M, Berry DL, Garza D, Hubbert CC, Yao TP, Baehrecke EH, Taylor JP (2007) HDAC6 rescues neurodegeneration and provides an essential link between autophagy and the UPS. Nature 447:859-63.

Paulsen JS, Hayden M, Stout JC, Langbehn DR, Aylward E, Ross CA, Guttman M, Nance M, Kieburtz K, Oakes D (2006) Preparing for preventive clinical trials: The predict-HD study. Arch Neurol 63:883.

Peters-Libeu C, Miller J, Rutenber E, Newhouse Y, Krishnan P, Cheung K, Hatters D, Brooks E, Widjaja K, Tran T, Mitra S, Arrasate M, Mosquera L, Taylor D, Weisgraber K, Finkbeiner S (2012) Disease-associated polyglutamine stretches in monomeric huntingtin adopt a compact structure. Journal of Molecular Biology 421:587-600.

Powers ET, Morimoto RI, Dillin A, Kelly JW, Balch WE (2009) Biological and chemical approaches to diseases of proteostasis deficiency. Annu Rev Biochem 78:959-91.

Powers E, Balch W (2013) Diversity in the origins of proteostasis networks - a driver for protein function in evolution. Nature Reviews. Molecular Cell Biology .

Prahlad V, Cornelius T, Morimoto RI (2008) Regulation of the cellular heat shock response in caenorhabditis elegans by thermosensory neurons. Science 320:811-4.

Preibisch S, Saalfeld S, Tomancak P (2009) Globally optimal stitching of tiled 3D microscopic image acquisitions. Bioinformatics (England) 25:1463-1465.

Price JH, Gough DA (1994) Comparison of phase-contrast and fluorescence digital autofocus for scanning microscopy. Cytometry (UNITED STATES) 16:283-297.

Rabut G, Ellenberg J (2004) Automatic real-time three-dimensional cell tracking by fluorescence microscopy. J Microsc 216:131-137.

Ravikumar B, Vacher C, Berger Z, Davies JE, Luo S, Oroz LG, Scaravilli F, Easton DF, Duden R, O'Kane CJ, Rubinsztein DC (2004) Inhibition of mTOR induces autophagy and reduces toxicity of polyglutamine expansions in fly and mouse models of huntington disease. Nat Genet 36:585-95.

Rocchi MB, Sisti D, Albertini MC, Teodori L (2007) Current trends in shape and texture analysis in neurology: Aspects of the morphological substrate of volume and wiring transmission. Brain Research Reviews 55:97-107.

Ross CA, Poirier MA (2004) Protein aggregation and neurodegenerative disease. Nat Med 10 Suppl:S10-7.

Rubin LL (2008) Stem cells and drug discovery: The beginning of a new era? Cell 132:549-52.

Sarkar S, Davies JE, Huang Z, Tunnacliffe A, Rubinsztein DC (2007) Trehalose, a novel mTOR-independent autophagy enhancer, accelerates the clearance of mutant huntingtin and alpha-synuclein. J Biol Chem 282:5641-52.

Saudou F, Finkbeiner S, Devys D, Greenberg ME (1998) Huntingtin acts in the nucleus to induce apoptosis but death does not correlate with the formation of intranuclear inclusions. Cell 95:55-66.

Schilling B, Gafni J, Torcassi C, Cong X, Row RH, LaFevre-Bernt MA, Cusack MP, Ratovitski T, Hirschhorn R, Ross CA, Gibson BW, Ellerby LM (2006) Huntingtin phosphorylation sites mapped by mass spectrometry. modulation of cleavage and toxicity. J Biol Chem 281:23686-97.

Shaner NC, Patterson GH, Davidson MW (2007) Advances in fluorescent protein technology. J Cell Sci 120:4247-4260.

Shaner NC, Lin MZ, McKeown MR, Steinbach PA, Hazelwood KL, Davidson MW, Tsien RY (2008) Improving the photostability of bright monomeric orange and red fluorescent proteins. Nat Meth 5:545-551.

Sharma P, Ando DM, Daub A, Kaye JA, Finkbeiner S (2012) High-throughput screening in primary neurons. Methods Enzymol 506:331-60.

Shcherbo D, Merzlyak EM, Chepurnykh TV, Fradkov AF, Ermakova GV, Solovieva EA, Lukyanov KA, Bogdanova EA, Zaraisky AG, Lukyanov S, Chudakov DM (2007) Bright far-red fluorescent protein for whole-body imaging. Nat Meth 4:741-746.

Simmons DA, Rex CS, Palmer L, Pandyarajan V, Fedulov V, Gall CM, Lynch G (2009) Up-regulating BDNF with an ampakine rescues synaptic plasticity and memory in huntington's disease knockin mice. Proceedings of the National Academy of Sciences 106:4906-4911.

Smalheiser NR (2002) Informatics and hypothesis-driven research. EMBO Reports 3:702.

Soldner F, Hockemeyer D, Beard C, Gao Q, Bell GW, Cook EG, Hargus G, Blak A, Cooper O, Mitalipova M, Isacson O, Jaenisch R (2009) Parkinson's disease patient-derived induced pluripotent stem cells free of viral reprogramming factors. Cell 136:964-77.

Soto C (2003) Unfolding the role of protein misfolding in neurodegenerative diseases. Nat Rev Neurosci 4:49-60.

Stadtfeld M, Nagaya M, Utikal J, Weir G, Hochedlinger K (2008) Induced pluripotent stem cells generated without viral integration. Science (New York, N Y 322:945-9.

Steffan JS, Agrawal N, Pallos J, Rockabrand E, Trotman LC, Slepko N, Illes K, Lukacsovich T, Zhu YZ, Cattaneo E, Pandolfi PP, Thompson LM, Marsh JL (2004) SUMO modification of huntingtin and huntington's disease pathology. Science 304:100-4.

Subramaniam S, Sixt KM, Barrow R, Snyder SH (2009) Rhes, a striatal specific protein, mediates mutant-huntingtin cytotoxicity. Science 324:1327-30.

Swedlow JR, Goldberg IG, Eliceiri KW (2009) Bioimage informatics for experimental biology. Annual Review of Biophysics 38:327-46.

Takahashi K, Yamanaka S (2006) Induction of pluripotent stem cells from mouse embryonic and adult fibroblast cultures by defined factors. Cell 126:663-76.

Takahashi K, Tanabe K, Ohnuki M, Narita M, Ichisaka T, Tomoda K, Yamanaka S (2007) Induction of pluripotent stem cells from adult human fibroblasts by defined factors. Cell 131:861-72.

Thevenaz P, Ruttimann UE, Unser M (1998) A pyramid approach to subpixel registration based on intensity. IEEE Trans Image Process (United States) 7:27-41.

Thompson LM et al (2009) IKK phosphorylates huntingtin and targets it for degradation by the proteasome and lysosome. J Cell Biol 187:1083-99.

Tsvetkov AS, Arrasate M, Barmada S, Ando DM, Sharma P, Shaby BA, Finkbeiner S (2013) Proteostasis of polyglutamine varies among neurons and predicts neurodegeneration. Nature Chemical Biology .

Turcu FER, Ventii KH, Wilkinson KD (2009) Regulation and cellular roles of ubiquitin-specific deubiquitinating enzymes. Annu Rev Biochem 78:363.

Tydlacka S, Wang C, Wang X, Li S, Li X (2008) Differential activities of the ubiquitin-proteasome system in neurons versus glia may account for the preferential accumulation of misfolded proteins in neurons. The Journal of Neuroscience : The Official Journal of the Society for Neuroscience 28:13285-13295.

van Oosten-Hawle P, Porter R, Morimoto R (2013) Regulation of organismal proteostasis by transcellular chaperone signaling. Cell 153:1366-1378.

Vos MJ, Zijlstra MP, Kanon B, van Waarde-Verhagen MA, Brunt ER, Oosterveld-Hut HM, Carra S, Sibon OC, Kampinga HH (2010) HSPB7 is the most potent

polyQ aggregation suppressor within the HSPB family of molecular chaperones. Hum Mol Genet .

Wellington CL, Ellerby LM, Gutekunst CA, Rogers D, Warby S, Graham RK, Loubser O, van Raamsdonk J, Singaraja R, Yang YZ, Gafni J, Bredesen D, Hersch SM, Leavitt BR, Roy S, Nicholson DW, Hayden MR (2002) Caspase cleavage of mutant huntingtin precedes neurodegeneration in huntington's disease. J Neurosci 22:7862-72.

Westerheide SD, Morimoto RI (2005) Heat shock response modulators as therapeutic tools for diseases of protein conformation. J Biol Chem 280:33097-100.

Wexler N (2012) Huntington's disease: Advocacy driving science. Annual Review of Medicine 63:1-22.

Xiaobo Z, Wong STC (2006) Informatics challenges of high-throughput microscopy. Signal Processing Magazine, IEEE 23:63-72.

Yamamoto A, Lucas JJ, Hen R (2000) Reversal of neuropathology and motor dysfunction in a conditional model of huntington's disease. Cell 101:57-66.

Young DW, Bender A, Hoyt J, McWhinnie E, Chirn GW, Tao CY, Tallarico JA, Labow M, Jenkins JL, Mitchison TJ, Feng Y (2008) Integrating high-content screening and ligand-target prediction to identify mechanism of action. Nature Chemical Biology 4:59-68.

Zeitelhofer M, Vessey JP, Xie Y, Tubing F, Thomas S, Kiebler M, Dahm R (2007) High-efficiency transfection of mammalian neurons via nucleofection. Nat Protoc (England) 2:1692-1704.

Zeitlin S, Liu J, Chapman D, Papaioannou V, Efstratiadis A (1995) Increased apoptosis and early embryonic lethality in mice nullizygous for the huntington's disease gene homologue. Nature Genetics 11:155-163.

Zhang JH, Chung TD, Oldenburg KR (1999) A simple statistical parameter for use in evaluation and validation of high throughput screening assays. J Biomol Screen 4:67-73.

Zhang L, Yu J, Pan H, Hu P, Hao Y, Cai W, Zhu H, Yu AD, Xie X, Ma D, Yuan J (2007a) Small molecule regulators of autophagy identified by an image-based high-throughput screen. Proceedings of the National Academy of Sciences of the United States of America 104:19023-8.

Zhang Y, Zhou X, Degterev A, Lipinski M, Adjeroh D, Yuan J, Wong ST (2007b) Automated neurite extraction using dynamic programming for high-throughput screening of neuron-based assays. NeuroImage 35:1502-15.

Zimmer C, Bo Z, Dufour A, Thebaud A, Berlemont S, Meas-Yedid V, Marin JCO (2006) On the digital trail of mobile cells. Signal Processing Magazine, IEEE 23:54-62.

Zimmermann T (2005) Spectral imaging and linear unmixing in light microscopy. Advances in Biochemical Engineering/Biotechnology 95:245-65.

Zitova B, Flusser J (2003) Image registration methods: A survey. Image Vision Comput 21:977-1000.

Zou J, Guo Y, Guettouche T, Smith D, Voellmy R (1998) Repression of heat shock transcription factor HSF1 activation by HSP90 (HSP90 complex) that forms a stress-sensitive complex with HSF1. Cell 94:471-480.

Zuccato C, Tartari M, Crotti A, Goffredo D, Valenza M, Conti L, Cataudella T, Leavitt BR, Hayden MR, Timmusk T (2003) Huntingtin interacts with REST/NRSF to modulate the transcription of NRSE-controlled neuronal genes. Nat Genet 35:76-83.

Zuccato C, Ciammola A, Rigamonti D, Leavitt B, Goffredo D, Conti L, MacDonald M, Friedlander R, Silani V, Hayden M, Timmusk T, Sipione S, Cattaneo E (2001) Loss of huntingtin-mediated BDNF gene transcription in huntington's disease. Science (New York, N.Y.) 293:493-498.

Appendix 1: Destabilizing mutant huntingtin through the UPS abrogates toxicity

A

HTT^{586}-Q$_{136}$-EGFP   HTT^{586}-Q$_{136}$-EGFP-CL

144
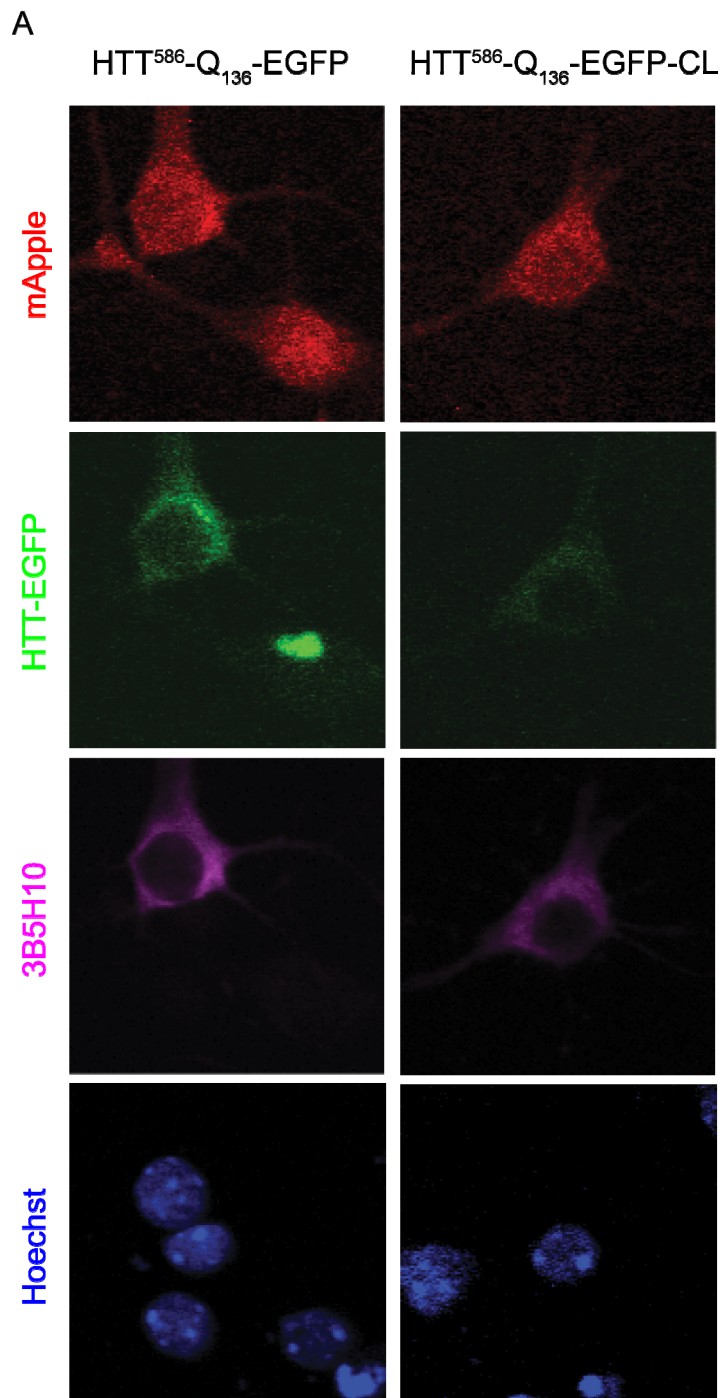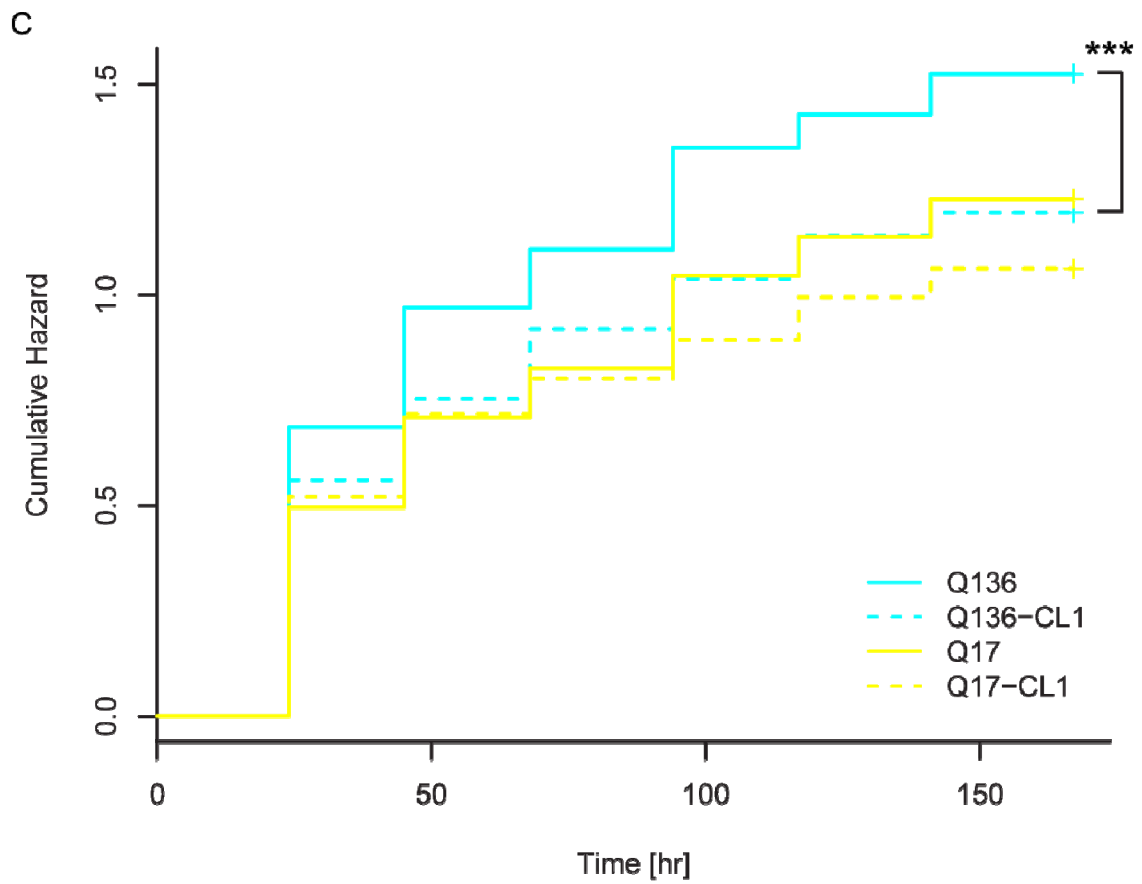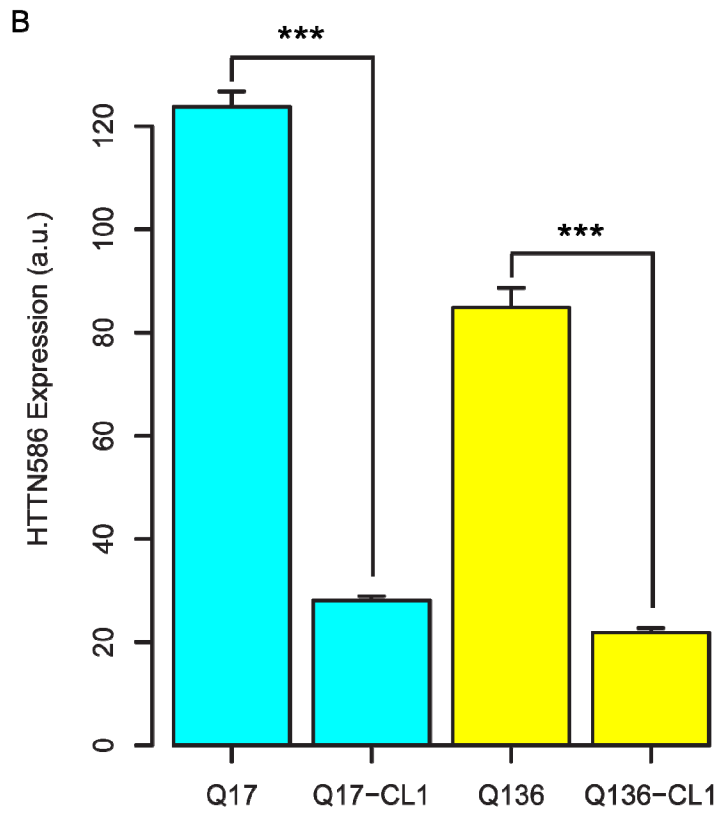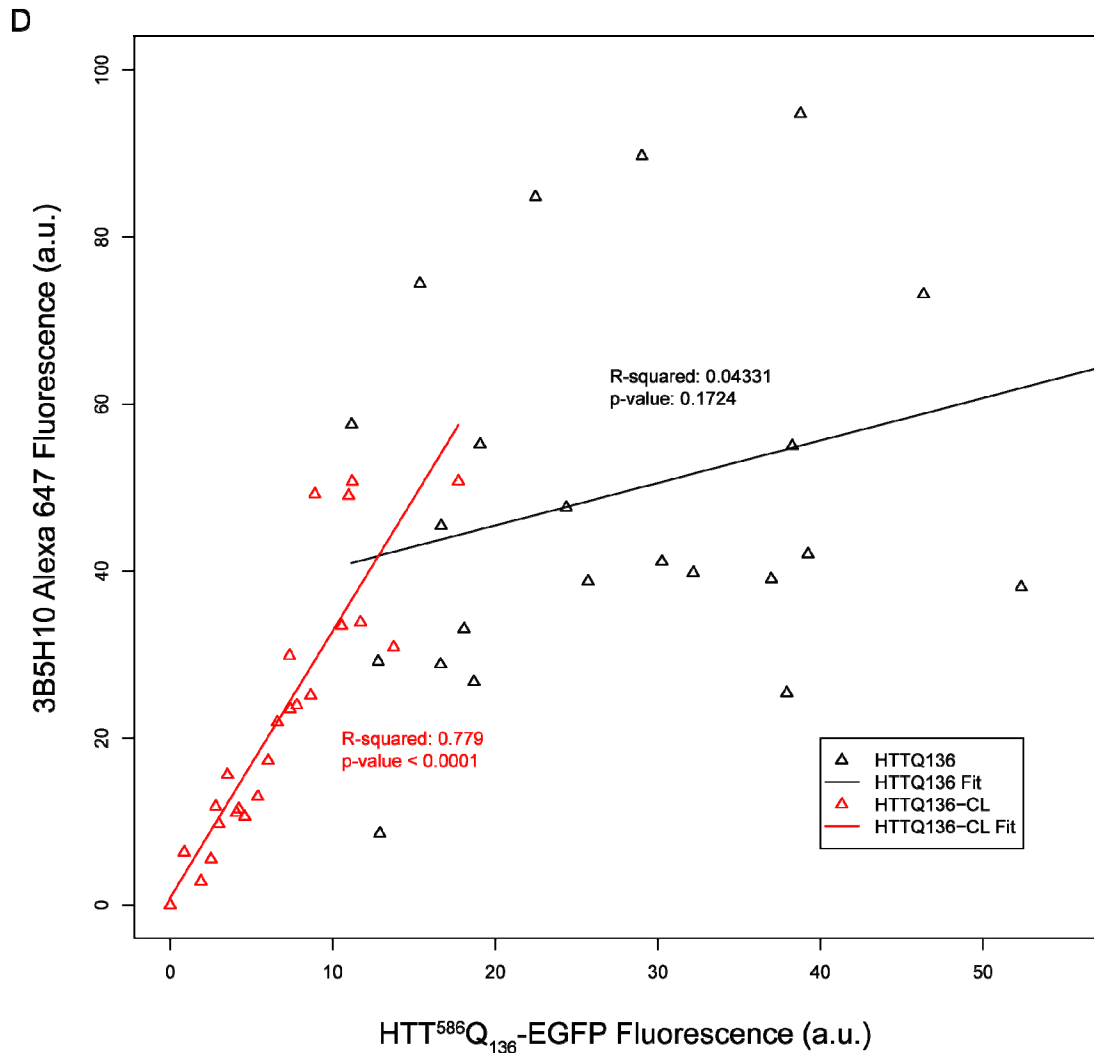
Figure 27. Destabilizing mHTT through the UPS abrogates toxicity. (A) A degron sequence (CL1: ACKNWFSSLSHFVIHL) was inserted at the N-terminus of HTT^{586}-Q$_{136}$-EGFP to destabilize the fusion protein. The stretch of hydrophobic amino acids in the sequence is recognized in cells, polyubiquitinated and targeted to the 26S proteasome for degradation. Mouse cortical neurons were transfected at DIV4 with HTT^{586}-Q$_{136}$-EGFP or HTT^{586}-Q$_{136}$-EGFP-CL1 along with mApple as the transfection marker. The cells were fixed 48 hours post-transfection and subjected to immunocytochemistry. The cells were labeled with 3B5H10 and Alexa 647-conjugated secondary antibody. Fluorescence of EGFP

was obtained by confocal microscopy and used as a surrogate for HTT expression level. (B) Quantification of EGFP fluorescence comparing protein expression of HTT[586]-EGFP with or without destabilization. Significance calculated by Student's two-sample t-test. $p<0.01$(**) (C) Survival of neurons transfected with the respective HTT constructs. Cortical neurons were transfected at DIV4 and subjected to longitudinal imaging by robotic microscopy. Cells were first imaged 24 hours post-transfection and thereafter imaged once per day for up to a week. Cell death was recorded and used to generate cumulative hazard curves. (D) Destabilization through the UPS changes the relationship between mHTT expression and 3B5H10 staining. Fluorescence from EGFP and Alexa 647-conjugated secondary antibody were captured by confocal microscopy for each neuron. Regression analysis was then performed between 3B5H10 label fluorescence and EGFP fluorescence.

Appendix 2: A heat shock response (HSR) reporter to monitor dynamic stress responses in neurons

A

CTAGAATGTTCTAGATCTAGAACATTCTAGCTAGAATGTTCTAGA

B

Vector (VC) HSF1 HSF2

mApple

HSE-mCitrine

C

D
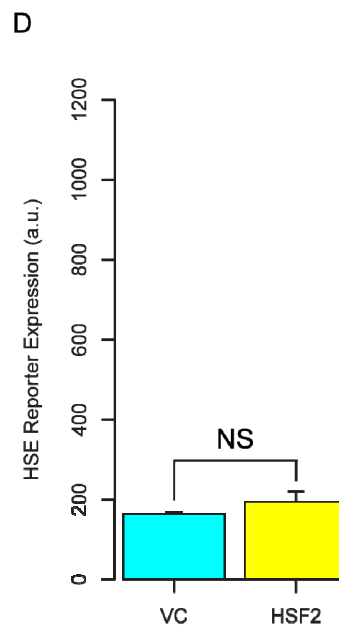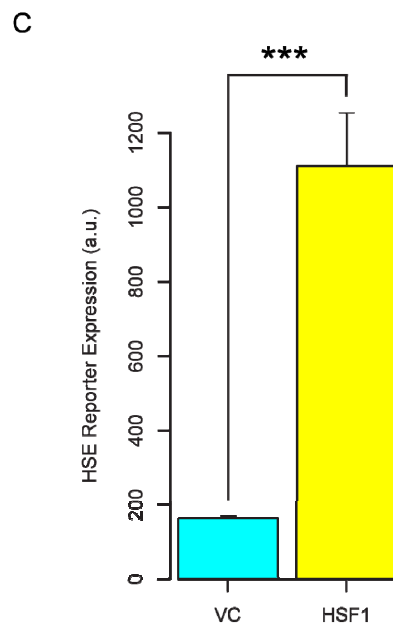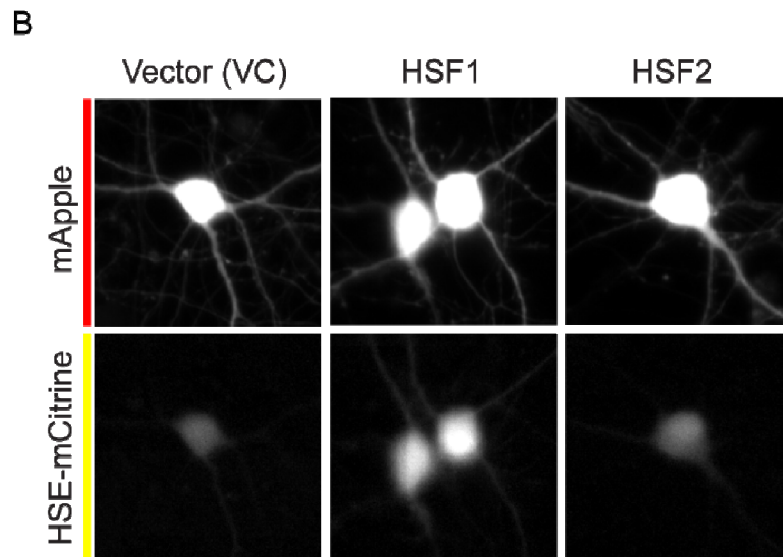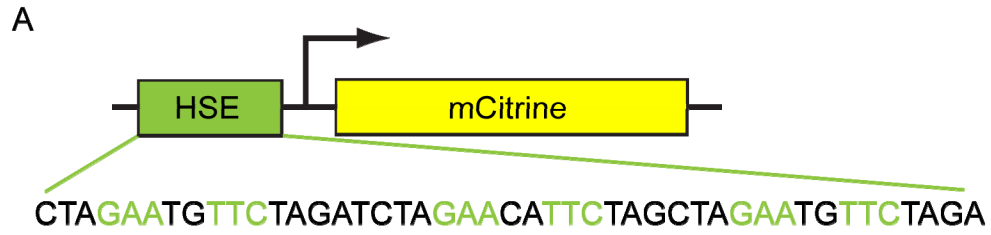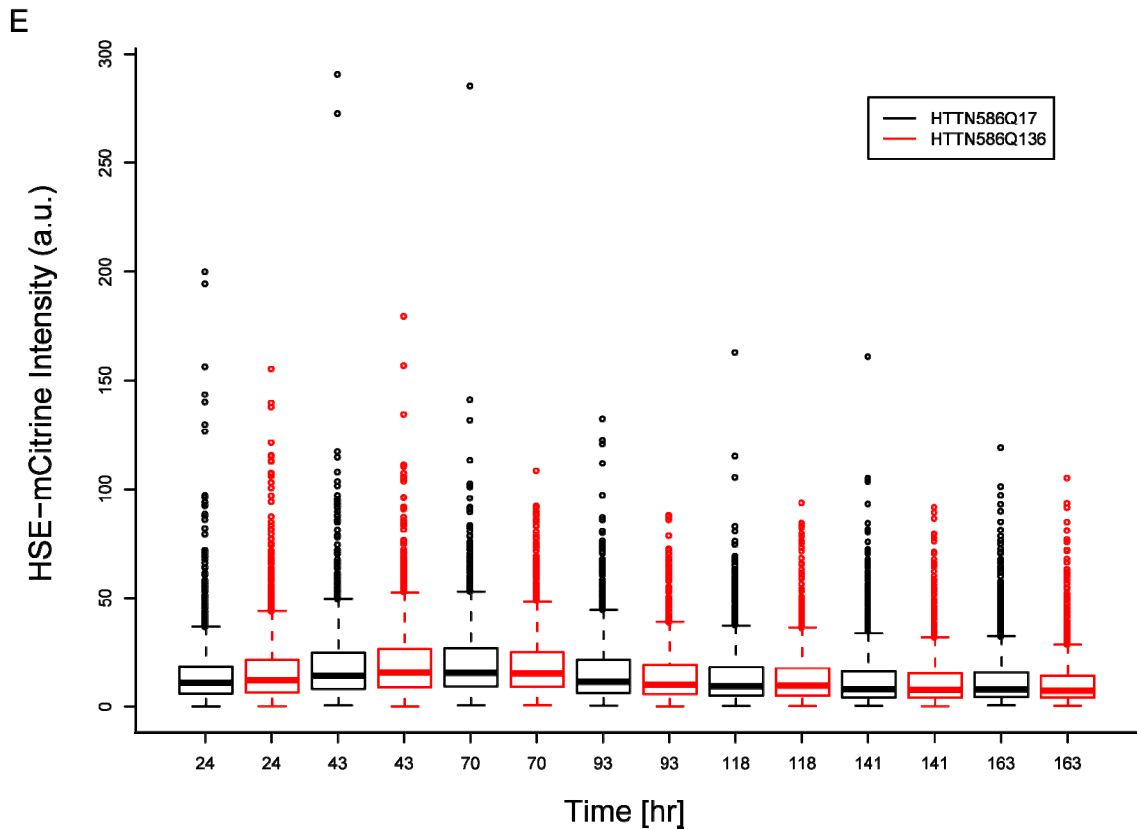
Figure 28. Neurons do not activate the HSR in response to mHTT. (A)

Construction of a fluorescent reporter with 6 nGAAn heat shock elements (HSE)

arranged in alternating orientations preceding mCitrine, a bright yellow

fluorescent protein. mCitrine was sub-cloned into pHSE (Clontech) to replace the

original luciferase reporter system. (B) Neurons containing the HSE reporter that

were co-transfected with either empty vector, HSF1, or HSF2. The reporter is

only activated by HSF1 and is not responsive to HSF2. (C-D) Quantification of

reporter activation for HSF1 and HSF2. (E) At DIV4, cortical neurons were co-

transfected with either HTT^{586}-Q$_{17}$-EGFP or HTT^{586}-Q$_{136}$-EGFP along with the

HSR reporter and mApple as a transfection marker. 24 hours after transfection,

the cells were subjected to automated microscopy and imaged once a day for a

week. Neurons were identified, tracked, and mCitrine intensity was extracted

from single cells using automated image analysis and used as a surrogate for

activation of the HSR. At all the time points measured, there was no significant

difference in HSR activation between Q_{17} cells and Q_{136} cells.

Appendix 3: ImageJ Stitching and Alignment Scripts

```
Text0 := 'dim = 2';
#n := NumberInGroup;
#dim := sqrt(#n);
#iw := @'Image Width';
#ih := @'Image Height';
#io := @'Overlap';
#aiw := #iw-#io;
#aih := #ih-#io;
#x := 0;
#y := #aih*#dim;
#xi := -1;
Resize(#img_loc,#n);


FOR #i IN 1 .. #n
LOOP
     IF mod(#i,#dim)==1 THEN
          #y -= #aih;
          #xi *= -1;
     ELSE
          #x := #x + #xi*#aiw;
     END IF;
     #img_loc[#i] := '('.String(#x).','.String(#y).')';

     Property('Text'.String(#i)) :=
property('/SciTegic.data.GroupNode/generic['.String(#i).']/
Path').'; ; '.#img_loc[#i];
END LOOP;
```

Table 7. PilotScript to calculate montage coordinates.

```
# Define the number of dimensions we are working on
dim = 2

# Define the image coordinates
D:\PP\Aaron\20130613_HSFKD\BackgroundSubtract\GFP\PID201306
13_HSFKD_T1_24_D12_1_GFP.tif; ; (0.0, 1930.0)
D:\PP\Aaron\20130613_HSFKD\BackgroundSubtract\GFP\PID201306
13_HSFKD_T1_24_D12_2_GFP.tif; ; (1317.0, 1930.0)
D:\PP\Aaron\20130613_HSFKD\BackgroundSubtract\GFP\PID201306
```

```
13_HSFKD_T1_24_D12_3_GFP.tif; ; (2634.0, 1930.0)
D:\PP\Aaron\20130613_HSFKD\BackgroundSubtract\GFP\PID201306
13_HSFKD_T1_24_D12_4_GFP.tif; ; (2634.0, 965.0)
D:\PP\Aaron\20130613_HSFKD\BackgroundSubtract\GFP\PID201306
13_HSFKD_T1_24_D12_5_GFP.tif; ; (1317.0, 965.0)
D:\PP\Aaron\20130613_HSFKD\BackgroundSubtract\GFP\PID201306
13_HSFKD_T1_24_D12_6_GFP.tif; ; (0.0, 965.0)
D:\PP\Aaron\20130613_HSFKD\BackgroundSubtract\GFP\PID201306
13_HSFKD_T1_24_D12_7_GFP.tif; ; (0.0, 0.0)
D:\PP\Aaron\20130613_HSFKD\BackgroundSubtract\GFP\PID201306
13_HSFKD_T1_24_D12_8_GFP.tif; ; (1317.0, 0.0)
D:\PP\Aaron\20130613_HSFKD\BackgroundSubtract\GFP\PID201306
13_HSFKD_T1_24_D12_9_GFP.tif; ; (2634.0, 0.0)
```

Table 8. Example of output file with calculated coordinates used by ImageJ.

The following macros are dynamically created by Pipeline Pilot and then called

by ImageJ in batch mode.

```
args = getArgument;
if (args=="") exit ("No argument!");
argArray = split(args, ",");
inputPathname = argArray[0];
outputPathname = argArray[1];
run("Stitch Collection of Images",
"layout=D:\\PP\\Aaron\\20130613_HSFKD\\BackgroundSubtract\\
TileConfiguration.txt channels_for_registration=[Red, Green
and Blue] rgb_order=rgb fusion_method=[Linear Blending]
fusion=1.50 regression=0.30 max/avg=2.50 absolute=3.50");
saveAs("Tiff",outputPathname);
```

Table 9. ImageJ macro for stitching multiple images without alignment

correction (Rigid).

```
args = getArgument;
if (args=="") exit ("No argument!");
argArray = split(args, ",");
inputPathname = argArray[0];
outputPathname = argArray[1];
run("Stitch Collection of Images",
```

```
"layout=D:\\PP\\Aaron\\20130613_HSFKD\\BackgroundSubtract\\
TileConfiguration.txt compute_overlap
channels_for_registration=[Red, Green and Blue]
rgb_order=rgb fusion_method=[Linear Blending] fusion=1.50
regression=0.30 max/avg=2.50 absolute=3.50");
saveAs("Tiff",outputPathname);
```

Table 10. ImageJ macro for stitching multiple images with alignment

correction (Flexible).

```
args = getArgument;
if (args=="") exit ("No argument!");
argArray = split(args, ",");
inputPathname = argArray[0];
outputPathname = argArray[1];
setBatchMode(true);
open(inputPathname);
rename("20130613_HSFKD");
run("MultiStackReg", "stack_1=20130613_HSFKD action_1=Align
file_1=D:\\PP\\Aaron\\20130613_HSFKD\\Montaged\\RFP\\TMatri
ces.txt stack_2=None action_2=Ignore file_2=[]
transformation=Translation save");
saveAs("Tiff",outputPathname);
close();
```

Table 11. ImageJ macro for calculating transformations and aligning a

stack of images.

```
args = getArgument;
if (args=="") exit ("No argument!");
argArray = split(args, ",");
inputPathname = argArray[0];
outputPathname = argArray[1];
setBatchMode(true);
open(inputPathname);
rename("20130613_HSFKD");
run("MultiStackReg", "stack_1=20130613_HSFKD action_1=[Load
Transformation File]
file_1=D:\\PP\\Aaron\\20130613_HSFKD\\Montaged\\RFP\\TMatri
ces.txt stack_2=None action_2=Ignore file_2=[]
transformation=Translation");
saveAs("Tiff",outputPathname);
close();
```

Table 12. ImageJ macro for calculating transformations and aligning a stack of images.

Appendix 4: Script to reassign cell labels during tracking

```
@ChildObjectList :=
%'/SciTegic.data.GroupNode/generic/CoLocalizedChildLabels';
#ParentLabels :=
%'/SciTegic.data.GroupNode/generic/ParentObjectLabelsFound'
;
#ChildLabels :=
%'/SciTegic.data.GroupNode/generic/ChildObjectLabelsFound';

Resize(@ParentObjectList,0);

/* Define replacement labels for colocalized children */
FOR #i IN 1 ..
NumValues(%'/SciTegic.data.GroupNode/generic/NumberOfCoLoca
lizedChildren') LOOP

    /* Print out the Parent Label the number of times
specified */
    FOR #j IN 1 ..
%'/SciTegic.data.GroupNode/generic/NumberOfCoLocalizedChild
ren'[#i] LOOP
        Append(@ParentObjectList,#ParentLabels[#i]);
    END LOOP;

END LOOP;

/* Append values for children that have not been
colocalized starting from the total number of neurons
onward */
FOR #i IN 1 .. NumValues(#ChildLabels) LOOP
    IF NOT (Contains(@ChildObjectList,#ChildLabels[#i]))
THEN
        Append(@ChildObjectList,#ChildLabels[#i]);
        Append(@ParentObjectList,++@TotalNumNeurons);
    END IF;
END LOOP;
```

Table 13. Tracking algorithm to reassign cell labels in adjacent timepoints.

Appendix 5: R script to create survival data from HCA_DATA.csv

```r
# Load libraries
library(splines)
library(survival)
library(reshape)
library(lattice)

# User-defined Parameters
root.dir <- "C:\\Users\\acdaub\\Desktop\\Alignment_Fig\\"
#Root directory where the data file exists
HCA.file <- "HCA_DATA.csv" #Data file that is output from
Pipeline Pilot
plate.file <- "PlateLayout.csv" #Plate layout file
timepoint.file <- "Timepoints.csv" #File that holds the
timepoints and corresponding hours
prim.channel <- "RFP" #Label of the primary channel used to
compute the survival time
time.dep.var <- "BlobCentroidX" #The variable you want to
tabulate over time

# Import the data file and configuration files
surv.data <-
unique(read.csv(paste(root.dir,HCA.file,sep="")))
p.layout <- read.csv(paste(root.dir,plate.file,sep=""))
df.times <- read.csv(paste(root.dir,timepoint.file,sep=""))

# Get the primary survival channel
surv.data.t1 <- subset(surv.data,Timepoint==1)
surv.data.c1 <-
subset(surv.data,MeasurementTag==prim.channel)

# Make a data.frame to hold survival data
sd <- data.frame()
md <- data.frame()
id <- data.frame()

# Factor the data.frame by the Well ID
surv.data.t1$Sci_WellID <- factor(surv.data.t1$Sci_WellID)
wells <- levels(surv.data.t1$Sci_WellID)

for (i in seq(from=1,to=length(wells),by=1)) {

  # Get a subset of the data that only contains neurons
existing in the first timepoint
  surv.data.well <- subset(surv.data,Sci_WellID==wells[i])
```

155

```r
  surv.data.well.t1 <- subset(surv.data.well,Timepoint==1)
  surv.data.well.t1.neurons <-
subset(surv.data.well,ObjectLabelsFound<=nrow(subset(surv.d
ata.well.t1,MeasurementTag==prim.channel)))

  # Put data in survival based format
  sd.well <-
aggregate(Timepoint~ObjectLabelsFound+Sci_WellID,surv.data.
well.t1.neurons,max)
  sd.well$Censored <-
sd.well$Timepoint==max(surv.data.c1$Timepoint)
  sd.well$Event <- !sd.well$Censored

  # Reformat the table to extract time-dependent data of
interest
  melt.data <- melt(surv.data.well.t1.neurons,
id=c('ObjectLabelsFound','Sci_WellID','MeasurementTag','Tim
epoint'))
  melt.data.intmean <-
subset(melt.data,variable==time.dep.var)

  # Cast data for easy interpretation
  intmean.bytime <-
cast(melt.data.intmean,ObjectLabelsFound+Sci_WellID+Measure
mentTag~Timepoint)

  # Append the dataframes from each individual well
  sd <- rbind(sd,sd.well)
  md <- rbind(md,melt.data.intmean)
  id <- rbind.fill(id,intmean.bytime)
}

# Merge Plate Layout onto survival data
sd <- merge(sd,p.layout)
sd <- merge(sd,df.times,sort=FALSE)
sd <-
sort_df(sd,vars=c('Sci_WellID','ObjectLabelsFound','Time'))
sd <-
sd[,c('ObjectLabelsFound','Sci_WellID','Sci_SampleID','Time
point','Time','Censored','Event','Date')]

# Merge plate layout onto melt data
md <- merge(md,p.layout)
md <- merge(md,p.layout)
md <- merge(md,df.times,sort=FALSE)
md <-
sort_df(md,vars=c('Sci_WellID','ObjectLabelsFound','Time'))
```

```
# Specify the column names of the resulting data frames and
merge plate data
names(id) <-
c('ObjectLabelsFound','Sci_WellID','MeasurementTag',paste(d
f.times$Time,sep=','))
id <- merge(id,p.layout)
id <-
sort_df(id,vars=c('Sci_WellID','ObjectLabelsFound','Measure
mentTag'))
id <-
id[,c('ObjectLabelsFound','Sci_WellID','Sci_SampleID','Meas
urementTag',paste(df.times$Time,sep=','))]

# Create a combined file with survival and intensity data
sd.id <-
merge(sd,id,by=c('Sci_WellID','ObjectLabelsFound','Sci_Samp
leID'))
sd.id <-
sort_df(sd.id,vars=c('Sci_WellID','ObjectLabelsFound','Time
'))

# Write out the csv files
write.csv(sd.id,file=paste(root.dir,"SurvivalWithIntensityD
ata.csv",sep=""))
```

Table 14. PPToSurvivalAndIntensityData.R. root.dir and HCA.file specify the

directory and file name of the data file exported by Pipeline Pilot.

```
# Load libraries
library(splines)
library(survival)
library(reshape)
library(lattice)
library(plyr)

# Parameters -------------------------------------------------
-------------------------------------------------------#
# Directory
root.dir <-
"G:\\Epifluorescence\\HSF1_Rescues_mHtt_Tox_Combined\\"
# Data files
data.file <- c(
  "20121031_SurvivalWithIntensityData.csv",
  "20130130_SurvivalWithIntensityData.csv",
  "20130206_SurvivalWithIntensityData.csv"
```

```r
)
prim.channel <- "RFP"
meas.channel <- "GFP"
filter.by.area <- FALSE
area.threshold <- 0.6
plot.title <- "HTT 586aa Fragment Toxicity"
pdf.file.name <- "Hsf1_WTHtt_FigureQuality.pdf"
c.order <-
c("Q136_VC","Q136_HSF1","Q136_HSF1R71G","Q17_VC")
c.label <- c("Q136+VC","Q136+HSF1","Q136+HSF1-
R71G","Q17+VC")
ref.cond <- "Q136_VC"
bg.invert <- FALSE

# Plot parameters ------------------------------------------
-----------------------------------------------------#
if (bg.invert) {
  pdf.bg <- "black"
  pdf.fg <- "white"
  pdf.col <- "white"
} else {
  pdf.bg <- "white"
  pdf.fg <- "black"
  pdf.col <- "black"
}
pdf.width <- 6
pdf.height <- 5
pdf.mar <- c(5,6,4,2)+0.1 #mar=c(bottom, left, top, right)
pdf.mgp <- c(3,0.5,0) #mgp=(axis title, axis labels and
axis line)
l.color <- c("green","purple","plum","red")
# ----------------------------------------------------------
-----------------------------------------------------#

# Import data files
surv.int.data <- data.frame()
for (i in seq(from=1,to=length(data.file),by=1)) {
  surv.int.data <-
rbind.fill(surv.int.data,read.csv(paste(root.dir,data.file[
i],sep="")))
}

# Select samples from the plate that you want to plot
sample.list <- c(
  "Q136_VC",
  "Q136_HSF1",
  "Q136_HSF1R71G",
```

```
    "Q17_VC"
    )
surv.int.data <-
surv.int.data[surv.int.data$Sci_SampleID%in%sample.list,]
# Refactor
surv.int.data$Sci_SampleID <-
factor(surv.int.data$Sci_SampleID,levels=c.order)
surv.int.data$Sci_SampleID <-
relevel(surv.int.data$Sci_SampleID,ref=ref.cond)
surv.int.data$Sci_WellID <-
factor(surv.int.data$Sci_WellID)

# Get individual channels
prim.data <-
subset(surv.int.data,MeasurementTag==prim.channel)
meas.data <-
subset(surv.int.data,MeasurementTag==meas.channel)
time.pts <- sort(unique(prim.data$Time))

if (filter.by.area) {
  # Get individual cell intensities
  y.val <- prim.data[,10:(10+length(time.pts)-1)]
  new.surv.time <- array()
  # Correct survival times from changes in area
  for (i in seq(from=1,to=nrow(prim.data),by=1)) {
    norm.diff <- c(prim.data[i,11:(11+length(time.pts)-
2)],0)/prim.data[i,10:(10+length(time.pts)-1)]
    new.surv.time[i] <-
max(time.pts[c(TRUE,norm.diff>area.threshold)],na.rm=TRUE)
  }
  # Add corrected times as a new column of the primary
channel data frame
  prim.data$Time.Corrected <- new.surv.time
}

# Create Kaplan Meier model and plot
pdf(paste(root.dir,pdf.file.name,sep=""),width=pdf.width,he
ight=pdf.height)
par(bg=pdf.bg,fg=pdf.fg,col=pdf.col,lwd=1.5,mar=pdf.mar,mgp
=pdf.mgp,col.lab=pdf.col,col.main=pdf.col,col.axis=pdf.col)
if (filter.by.area) {
  kmfit.sd <-
survfit(Surv(Time.Corrected,Event)~Sci_SampleID,data=prim.d
ata)
} else {
  kmfit.sd <-
survfit(Surv(Time,as.logical(Event))~Sci_SampleID,data=prim
```

```r
.data)
}
plot(kmfit.sd,col=l.color,fun='cumhaz',xlab='Time
[hr]',ylab='Cumulative
Hazard',main=plot.title,bty='l',lwd=1.5)
legend('bottomright',legend=c.label,fill=l.color,bty='n',bo
rder=pdf.col)
dev.off()

# Get intensity data from the measurement channel at T1 (or
any other time point of interest)
prim.data$gfp.t2 <-
rowMeans(meas.data[,c("X32","X42","X45")],na.rm=TRUE)
prim.data$gfp.t1 <-
rowMeans(meas.data[,c("X19","X20","X24")],na.rm=TRUE)

# Plot intensity distributions
pdf(file=paste(root.dir,"HttIntensityDistribution.pdf",sep=
""),width=pdf.width,height=pdf.height)
par(bg=pdf.bg,fg=pdf.fg,col=pdf.col,lwd=1.5,mar=pdf.mar,mgp
=pdf.mgp,col.lab=pdf.col,col.main=pdf.col,col.axis=pdf.col)
# Iterate through all the conditions
first.object <- TRUE
for (i in seq(from=1,to=length(c.order),by=1)) {
  # Choose one condition
  int.meas.cond <-
subset(prim.data,Sci_SampleID==c.order[i])
  if (first.object) {
      # Plot the first cell

plot(density(int.meas.cond$gfp.t1),na.rm=TRUE,n=100,xlim=c(
0,1000),ylim=c(0,0.0035),xlab='Intensity
(a.u.)',ylab='Density',main="Mutant Huntingtin
Expression",col=l.color[i],lwd=1.5,bty='l')
      first.object <- FALSE
    } else {
      # Plot each subsequent cell

lines(density(int.meas.cond$gfp.t1),na.rm=TRUE,n=100,col=l.
color[i],lwd=1.5,bty='l')
    }

legend('topright',legend=c.label,fill=l.color,bty='n',borde
r=pdf.col)
}
# Close the pdf
dev.off()
```

```
# Fit a CPH model
prim.data$Sci_SampleID <- factor(prim.data$Sci_SampleID)
prim.data$Sci_SampleID <-
relevel(prim.data$Sci_SampleID,ref=ref.cond)
cpfit <-
coxph(Surv(Time,as.logical(Event))~Sci_SampleID+strata(Date
),data=prim.data)
```

Table 15. SurvivalPlotFromSurvivalData.R. root.dir and data.file specify the

directory and file name of the data file exported by

PPToSurvivalAndIntensityData.R.

Appendix 6: Automated Microscope Acquisition Code

```vb
Attribute VB_Name = "Module1"
Option Explicit

'***********************************************************
************
' Filename:   Run96WellPlate.ipm
'
' Created:          11/12/07
' Modified:         11/12/07
' Author:           Aaron Daub
' Application:      IPWin
' Version:          6.3
' Change History:
'***********************************************************
************

'------------------------------------------------------------
-----------------------------------------------------'
'                                           Declarations for the
KiNEDx robot                                             '
'------------------------------------------------------------
-----------------------------------------------------'

'Inp and Out declarations for port I/O using inpout32.dll.
Private Declare Function Inp Lib "inpout32.dll" Alias
"Inp32" _
    (ByVal PortAddress As Integer) _
    As Integer

Private Declare Sub Out Lib "inpout32.dll" Alias "Out32" _
    (ByVal PortAddress As Integer, _
    ByVal Value As Integer)

'Port Address (Decimal) Address (Hex)
'Data Lines 888 378h
'Control Lines 890 37Ah
'Status Lines 889 379h

'Reads system clock
Private Declare Function timeGetTime Lib "winmm.dll" () As
Long

'Pauses execution
Private Declare Sub Sleep Lib "kernel32" (ByVal
```

```vb
dwMilliseconds As Long)

'-------------------------------------------------------------
------------------------------------------------------'
'                                          Declarations for
Plate Initialization                                       '
'-------------------------------------------------------------
------------------------------------------------------'

' Objective information
Private gNames() As String, gNA() As Single, gMag() As
Single, gRI() As Single
Private gDOF As Single
Private gMatchObj As Integer
Private gNumPlanes As Integer

' Baseline offsets
Private gFiducial(0 To 2) As Single
Private g24Fiducial(0 To 2) As Single
Private gWell(0 To 2) As Single
Private g24Well(0 To 2) As Single
Private gbIsInit As Boolean
Private gPixelsPerMM As Single
Private gA1Center(0 To 2) As Single
Private gOffsetCenter(0 To 2) As Single
Private gLoopNum As Single

' Working Z offset for the fiducial marker
Private gZFiducialFlag As Boolean

' Focus settings
Private Const FOCAL_DISTANCE = 0.100       ' Number of mm
range for AF
Private Const FRACTION_DOF = 1.0           ' Fraction of
DOF for focus step size
Private Const OFFSET_FILE_VERSION = 2      ' Version
number for offset files

' Plate identification
Private gstrPlateID As String


'-------------------------------------------------------------
------------------------------------------------------'
'                                          Declarations for
Plate Position                                           '
'-------------------------------------------------------------
------------------------------------------------------'
```

```vb
Private gCurrPosX As Single, gCurrPosY As Single

Private Const X_INTERWELL_DIST_24W = 18.6
Private Const Y_INTERWELL_DIST_24W = 18.6
Private Const X_INTERWELL_DIST = 9.0
Private Const Y_INTERWELL_DIST = 9.0
Private Const X_WELL_OFFSET = 0 'Default = 0
Private Const Y_WELL_OFFSET = 0 'Default = 0
Private Const NUM_COL_24WELL = 6 'Default = 6
Private Const NUM_ROW_24WELL = 4 'Default = 4
Private Const NUM_COL_96WELL = 12 'Default = 12
Private Const NUM_ROW_96WELL = 8 'Default = 8
Private Const HEIGHT_PIXELS = 1040 'Default = 1040
Private Const WIDTH_PIXELS = 1392 'Default = 1392
Private Const MONTAGE_OVERLAP_PIXELS = 75 'Default = 75
Private Const IS_LOOP = 0 'Binary variable indicating if
you want to loop run, Default = 0

'----------------------------------------------------------
---------------------------------------------------'
'                                          Declarations for
Acquisition                                               '
'----------------------------------------------------------
---------------------------------------------------'

'Turret Positions:
'C/Y/R -> 1
'D/F/T -> 0
'ET-CY5 -> 3
'Sedat -> 2
Private Const TURRET_POS = 0

'Objective Positions:
'Plan Fluor 20X (Air) -> 2
'Plan Fluor 40X (Air) -> 3
Private Const OBJECTIVE_POS = 2

' Channels
Private Const PHOTOSWITCHFLAG = 0
Private Const BFFLAG = 0
Private Const BFPFLAG = 0
Private Const CFPFLAG = 0
Private Const GFPFLAG = 1
Private Const YFPFLAG = 0
Private Const RFPFLAG = 1
Private Const CY5FLAG = 0
```

```vb
' Montage Settings
Private Const NUM_TILES_Y = 3 'Default = 3
Private Const NUM_TILES_X = 3 'Default = 3

' Exposures
Private Const EXP_FILE As String =
"D:\IPWIN70\Exposure\ANDOR_1000MS_EXP.vpf"

Private Sub OutPort(PortAddress As Integer, OutNum As
Integer, State As Boolean)

    Dim PortState As Integer
    Dim NewState As Integer

    'Get the current states of all bits
    PortState = Inp(PortAddress)

    'Check if bit is already high
    NewState = PortState
    If (PortState And 2 ^ (OutNum - 1)) = 2 ^ (OutNum - 1)
Then NewState = PortState - (2 ^ (OutNum - 1))

    If State = True Then NewState = PortState + (2 ^
(OutNum - 1))

    Out PortAddress, NewState

End Sub

Function BitStatus(PortAddress As Integer, Bit As Integer)
As Integer

    Dim i As Integer
    Dim NumOfBits As Integer
    Dim PortNum As Integer

    NumOfBits = 4
    If PortAddress = 888 Then NumOfBits = 8
    If PortAddress = 889 Then NumOfBits = 8

    ReDim PortBits(NumOfBits) As Integer
    PortNum = Inp(PortAddress)

    For i = 1 To NumOfBits
        PortBits(i) = PortNum Mod 2
        PortNum = Fix(PortNum / 2)
    Next
```

```vbnet
    BitStatus = PortBits(Bit)

End Function

Private Sub SetDataBit0_ON() 'LPT pin 2 -> Serial DSR pin
6, Unload Microscope

    OutPort 888, 1, True

End Sub

Private Sub SetDataBit0_OFF()

    OutPort 888, 1, False

End Sub

Private Sub SetDataBit1_ON() 'LPT pin 3 -> Serial CTS pin
8, Reset Plate Count

    OutPort 888, 2, True

End Sub

Private Sub SetDataBit1_OFF()

    OutPort 888, 2, False

End Sub

Private Sub SetDataBit2_ON() 'LPT pin 4 -> Serial DCD pin
1, Load Microscope

    OutPort 888, 3, True

End Sub

Private Sub SetDataBit2_OFF()

    OutPort 888, 3, False

End Sub

Private Sub SetDataBit3_ON() 'LPT pin 5 -> Serial RI pin 9,
Unassigned
```

```vb
    OutPort 888, 4, True

End Sub

Private Sub SetDataBit3_OFF()

    OutPort 888, 4, False

End Sub

Private Sub SetBUSY_OFF()

    OutPort 888, 8, False

End Sub

Function ReadACK() As Integer 'LPT pin 10 -> Serial DTR pin 4, Unassigned

    Dim State As Integer

    'Read ACK
    State = BitStatus(889, 7)

    ReadACK = State

End Function

Function WaitForACK(DesiredState As Integer, TimeoutMsec As Long) As Integer

    Dim State As Integer
    Dim StartTime As Long

    StartTime = timeGetTime
    State = -1

    While timeGetTime - StartTime < TimeoutMsec And DesiredState <> State
        State = ReadACK()
        DoEvents
    Wend


    'Return the actual state
    WaitForACK = State
```

```vb
End Function

Function ReadBUSY() As Integer 'LPT pin 11 -> Serial RTS
pin 7, Command Complete

    Dim State As Integer

    'Read BUSY
    State = BitStatus(889, 8)

    ReadBUSY = State

End Function

Function WaitForBUSY(DesiredState As Integer, TimeoutMsec
As Long) As Integer

    Dim State As Integer
    Dim StartTime As Long

    StartTime = timeGetTime
    State = -1

    While timeGetTime - StartTime < TimeoutMsec And
DesiredState <> State
        State = ReadBUSY()
        DoEvents
    Wend

    'Return the actual state
    WaitForBUSY = State

End Function

Function WaitLoad

    WaitForBUSY(0,10000)
    WaitForBUSY(1,60000)

End Function

Function WaitUnload

    WaitForACK(1,10000)
    WaitForACK(0,60000)

End Function
```

```vba
Sub LoadScope

    Dim bStat As Integer, ackStat As Integer

    'Initialize Robot
    SetDataBit0_OFF
    SetDataBit1_OFF
    SetDataBit2_OFF

    'Load Microscope
    SetDataBit2_ON
    'IpOutputShow(1)
    'IpOutputClear()
    WaitLoad()
    'IpOutput("Robot Loading Complete")

End Sub

Sub UnloadScope

    Dim bStat As Integer, ackStat As Integer

    'Initialize Robot
    SetDataBit0_OFF
    SetDataBit1_OFF
    SetDataBit2_OFF

    'Unload Microscope
    SetDataBit0_ON
    'IpOutputShow(1)
    'IpOutputClear()
    WaitUnload()
    'IpOutput("Robot Unloading Complete")

End Sub

Sub Run24WellPlate

    Dim absXYZ(0 To 2) As Single, PFOffset As Single

    'Initialization
    Call InitSettings()

    ret =
IpAcqSettings("D:\IPWIN70\Exposure\ANDOR_33MS_EXP.vpf",0)
    ret = IpScopeSettings("D:\IPWIN70\ScpConfig\20X
```

```
Brightfield (Camera).scp",SCP_LOAD)
    ret = IpScopeSetPosition(SCP_LAMP1, 3)

    'Register fiducial point on plate and make relative
move to Well A,1
    'Move to the Z Absolute Position
    GoToFiducial_24Well()
    ret = IpMacroStop("Confirm Fiducial Alignment", 0)
    UpdateCurrPos()

    'Acquire the reference image for subsequent alignments
    AcquireRefImage()

    PerfectFocusOFF()
    ret = IpScopeSettings("D:\IPWIN70\ScpConfig\20X
Brightfield (Camera).scp",SCP_LOAD)
    ret = IpScopeSetPosition(SCP_LAMP1, 150)
    MoveOriginToA1Center_24Well()

    'Set perfect focus settings
    PerfectFocusON()
    PFOffset = 4722
    ret = IpScopeControl(SCP_SET_CONTFOC_POS,
SCP_CONTINUOUSFOCUS, 4, "", PFOffset)
    ret = IpMacroStop("Confirm A1 Focus", 0)
    UpdateCurrPos()

    'Take images of 96 well plate
    PlateAcquire_24BRG()

    'Move stage to its lower right limit so that robot can
load a plate (large values in mm so that stage hits limits)
    PerfectFocusOFF()
    ret = IpStageXY(1000,1000)

End Sub

Sub Run96WellPlate

    Dim absXYZ(0 To 2) As Single, PFOffset As Single
    Dim FiducialOffset As POINTAPI, xOffsetMM As Single,
yOffsetMM As Single, ipStgSpd As Single

    'Initialization
    Call InitSettings()

    'Change stage speed to maximum
```

170

```
    ipStgSpd = 100
    ret = IpStageControl(STG_SET_XY_SPEED, ipStgSpd)

    'Move stage to its lower right limit so that robot can
load a plate (large values in mm so that stage hits limits)
    'ret = IpStageXY(1000,1000)
    'Load plate from stack 1 onto the stage
    'Call LoadScope()

    ret =
IpAcqSettings("D:\IPWIN70\Exposure\ANDOR_33MS_EXP.vpf",0)
    ret = IpScopeSettings("D:\IPWIN70\ScpConfig\20X
Brightfield (Camera).scp",SCP_LOAD)
    ret = IpScopeSetPosition(SCP_LAMP1, 333)

    'Close the stage secure gate
    SecureGate(1)

    'Register fiducial point on plate and make relative
move to Well A,1
    'Move to the Z Absolute Position
    GoToFiducial()
    ret = IpMacroStop("Open reference image and focus on
fiducial marker.", 0)
    UpdateCurrPos()

    'Acquire the reference image for subsequent alignments
    AcquireRefImage()
    FiducialOffset = CalculateAlignment()
    xOffsetMM = FiducialOffset.x/gPixelsPerMM
    yOffsetMM = FiducialOffset.y/gPixelsPerMM
    IpStageXY(gCurrPosX+xOffsetMM, gCurrPosY-yOffsetMM)
    ret = IpMacroStop("Confirm calculated alignment.", 0)
    UpdateCurrPos()

    PerfectFocusOFF()
    ret = IpScopeSettings("D:\IPWIN70\ScpConfig\20X
Brightfield (Camera).scp",SCP_LOAD)
    ret = IpScopeSetPosition(SCP_LAMP1, 150)
    MoveOriginToA1Center()

    'Move Offset if indicated
    'PerfectFocusOFF()
    'ret =
IpStageXY(gCurrPosX+X_WELL_OFFSET*X_INTERWELL_DIST,gCurrPos
Y+Y_WELL_OFFSET*Y_INTERWELL_DIST)
    'UpdateCurrPos()
```

```vba
    'Set perfect focus settings
    PerfectFocusON()
    PFOffset = 4750 'YFP
    ret = IpScopeControl(SCP_SET_CONTFOC_POS,
SCP_CONTINUOUSFOCUS, 4, "", PFOffset)
    ret = IpMacroStop("Confirm A1 Focus", 0)
    UpdateCurrPos()

    'Take images of 96 well plate
    PlateAcquire_96BRG()

    'Move stage to its lower right limit so that robot can
load a plate (large values in mm so that stage hits limits)
    PerfectFocusOFF()
    ret = IpStageXY(1000,1000)
    'Open the stage secure gate
    SecureGate(0)
    'Unload plate from stage
    'Call UnloadScope()

End Sub

' Read all baseline settings
Private Sub InitSettings()

    Dim strTmp As String * 64

    '--- Coordinates for TPP 96 Well Fiducial Marker '
    ret = IpIniFile(INICMD_GETFLOAT, "Stage Align general
Fiducial X", gFiducial(0))
    ret = IpIniFile(INICMD_GETFLOAT, "Stage Align general
Fiducial Y", gFiducial(1))
    ret = IpIniFile(INICMD_GETFLOAT, "Stage Align general
Fiducial Z", gFiducial(2))
    '--- Coordinates for TPP 24 Well Fiducial Marker '
    ret = IpIniFile(INICMD_GETFLOAT, "Stage Align general
24 Fiducial X", g24Fiducial(0))
    ret = IpIniFile(INICMD_GETFLOAT, "Stage Align general
24 Fiducial Y", g24Fiducial(1))
    ret = IpIniFile(INICMD_GETFLOAT, "Stage Align general
24 Fiducial Z", g24Fiducial(2))
    '--- Coordinates for TPP 96 Well A1 Center with respect
to Fiducial Marker '
    ret = IpIniFile(INICMD_GETFLOAT, "Stage Align general
Well X", gWell(0))
    ret = IpIniFile(INICMD_GETFLOAT, "Stage Align general
```

```vba
Well Y", gWell(1))
    ret = IpIniFile(INICMD_GETFLOAT, "Stage Align general
Well Z", gWell(2))
    '--- Coordinates for TPP 96 Well A1 Center with respect
to Fiducial Marker '
    ret = IpIniFile(INICMD_GETFLOAT, "Stage Align general
24 Well X", g24Well(0))
    ret = IpIniFile(INICMD_GETFLOAT, "Stage Align general
24 Well Y", g24Well(1))
    ret = IpIniFile(INICMD_GETFLOAT, "Stage Align general
24 Well Z", g24Well(2))


    ' Determine which objective is being used
    ret = IpIniFile(INICMD_GETFLOAT, "Pixels per MM 20X",
gPixelsPerMM)

    UpdateCurrPos()
    'ret = CheckObj()

    ' Name the plate
    ret = IpStGetString("Enter the plate ID", strTmp, 64)
    gstrPlateID = "PID" + IpTrim(strTmp)

    gbIsInit = True

End Sub

' Save baseline settings
Private Sub SaveSettings()
    ret = IpIniFile(INICMD_SETFLOAT, "Stage Align general
Fiducial X", gFiducial(0))
    ret = IpIniFile(INICMD_SETFLOAT, "Stage Align general
Fiducial Y", gFiducial(1))
    ret = IpIniFile(INICMD_SETFLOAT, "Stage Align general
Well X", gWell(0))
    ret = IpIniFile(INICMD_SETFLOAT, "Stage Align general
Well Y", gWell(1))
    ret = IpIniFile(INICMD_SETFLOAT, "Stage Align general
Well Z", gWell(2))

End Sub

Private Sub Set_Plate_Origin()
    Dim offsetX As Single, offsetY As Single, offsetZ As
Single
    Dim appDir As String*255, fName As String
    Dim plateIm As String, plateOffset As String
```

```vba
    Dim xFid As Single, yFid As Single
    Dim bStandard As Boolean
    Dim xOrigin As Single, yOrigin As Single, zOrigin As
Single
    Dim fAbs(0 To 2) As Single
    Dim snapIm As Integer
    Dim numX As Single, numY As Single
    Dim guardPix As Single, xPix As Single, yPix As Single
    Dim calX As Single, sizeX As Single, sizeY As Single
    Dim extentX As Single, extentY As Single

    Dim objNa As Single, objMag As Single, objRI As Single
    Dim objStr As String*100

    ' Check for objective information
    'ret = CheckObj()
    'If ret < 0 Then
    '    Beep
    '    Exit Sub
    'End If

    ' Check the scan size
    ret = IpStageGet(STG_X_FIELDS, 0, numX)
    ret = IpStageGet(STG_Y_FIELDS, 0, numY)

    ret = IpStageGet(STG_X_MM, 0, sizeX)
    ret = IpStageGet(STG_Y_MM, 0, sizeY)

    ret = IpStageGet(STG_GUARD_PIX, 0, guardPix)
    ret = IpStageGet(STG_X_PIX, 0, xPix)
    ret = IpStageGet(STG_Y_PIX, 0, yPix)

    ' Calculate the actual scan area based on this, minus
guard frame
    extentX = numX * (sizeX * (xPix-guardPix*2) / xPix) +
sizeX * (guardPix*2 / xPix)
    extentY = numY * (sizeY * (yPix-guardPix*2) / yPix) +
sizeY * (guardPix*2 / yPix)

    ' Check with the user re: scan pattern
    ret = IpMacroStop("The current scan pattern is " + _
        IpTrim(Str(numX)) + "x" + IpTrim(Str(numY)) + vbCr
+ _
        "Is this correct?", MS_MODAL+MS_YESNO)

    If ret = 0 Then
        ret = IpMacroStop("Set scan pattern as desired and
```

```vba
try again", 0)
        Exit Sub
    End If

    ret = IpAppGetStr(APPGETSTR_GETAPPDIR, 0, appDir)
    fName = Dir(IpTrim(appDir) + "RefImage", vbDirectory)
    If fName = "" Then
        MkDir IpTrim(appDir) + "RefImage"
    End If

    plateIm = IpTrim(appDir) + "RefImage" + "\" +
gstrPlateID + ".tif"
    plateOffset = IpTrim(appDir) + "RefImage" + "\" +
gstrPlateID + ".Offset"

    ' Turn Backlash correction on
    ipStgVal = 1
    ret = IpStageControl(STG_SELECT_REMOVE_BACKLASH,
ipStgVal)

    If gFiducial(0) = 0.0 And gFiducial(1) = 0.0 Then
        ' No fiducal 'standard location' known - try to
generate one
        bStandard = False
        ret = IpMacroStop("NOTE: Since baseline offsets
have not yet been set," + vbCr + _
            "the Fiducial and Well origins set here will be
used as references", 0)
    Else

        'For debugging
        OutputCoordinates()

        ' Move to the generic fiducial location
        ret = IpStageXY(gFiducial(0), gFiducial(1))
        bStandard = True

        'For debugging
        OutputCoordinates()

    End If

TryFiducial:
    ret = IpScopeSettings("D:\IPWIN63\ScpSettings\10X
Brightfield (Camera).scp",SCP_LOAD)
    ret = IpAcqShow(ACQ_LIVE, 1)
    ret = IpMacroStop("Locate and focus on the fiducial
```

```vbscript
mark for this plate." + vbCr + _
        "This should be a distinct feature in both X and Y
that can be found again.", 0)

    'For debugging
    OutputCoordinates()

    ' Capture and save the image
    ret = IpAcqShow(ACQ_LIVE, 0)
    snapIm = IpAcqSnap(ACQ_NEW)
    ret = IpPcTint(TINT_REMOVE)
    ret = IpMacroStop("Is this the desired fiducial point?
Click 'No' if you" + vbCr + _
        "wish to search again", MS_MODAL+MS_YESNO)

    If ret = 0 Then
        ret = IpDocCloseEx(snapIm)
        GoTo TryFiducial
    End If

    ret = IpScopeSettings("D:\IPWIN63\ScpSettings\20X
Brightfield (Camera).scp",SCP_LOAD)

    ret = IpStageControl(GETX, xFid)
    ret = IpStageControl(GETY, yFid)
    ret = IpStageGetAbsPosition(fAbs(0))
    ret = IpWsSaveAs(plateIm, "TIF")

    ' Offset by scan size
    ret = IpStageControl(GETX, xOrigin)
    ret = IpStageControl(GETY, yOrigin)
    ret = IpStageControl(GETZ, zOrigin)

    offsetX = xOrigin - xFid
    offsetY = yOrigin - yFid
    offsetZ = zOrigin

    Open plateOffset For Output As #1
    Write #1, OFFSET_FILE_VERSION
    Write #1, fAbs(0)
    Write #1, fAbs(1)
    Write #1, offsetX
    Write #1, offsetY
    Write #1, offsetZ
    Close #1

    ' If these have not been initialized, save them!
```

```vba
    If gFiducial(0) = 0.0 And gFiducial(1) = 0.0 Then
        gFiducial(0) = fAbs(0)
        gFiducial(1) = fAbs(1)

        gWell(0) = offsetX
        gWell(1) = offsetY
        gWell(2) = offsetZ

        Call SaveSettings()
    End If

    ret = IpDocCloseEx(snapIm)

DebugOut:

End Sub

Function CheckObj() As Integer
    Dim nLenses As Long, i As Long
    Dim sTmp As String*256

    ' Get whatever the last lens used was
    Dim sNominalLens As String*256

    gMatchObj = -1

    ret = IpIniFileStr(INICMDSTR_GETSTRING, "Nominal
Objective", sNominalLens)

    If ret < 0 Then
        ' Go ask about objectives
        Call Mag_settings()
    Else
        ' Obtain information about the current set of
lenses
        ret = IpLensGetLong(LENSGETLNG_NUMLENSES, nLenses)

        If nLenses < 1 Then Exit Function

        ReDim gNames(0 To nLenses-1) As String
        ReDim gNA(0 To nLenses-1) As Single
        ReDim gMag(0 To nLenses-1) As Single
        ReDim gRI(0 To nLenses-1) As Single

        For i=0 To nLenses-1
            ret = IpLensGetStr(LENS_LIST, i, sTmp)
            gNames(i) = IpTrim(sTmp)
```

```
            ret = IpLensGetSng(gNames(i),
LENSGETSNG_MAGNIFICATION, gMag(i))
            ret = IpLensGetSng(gNames(i), LENSGETSNG_NA,
gNA(i))
            ret = IpLensGetSng(gNames(i), LENSGETSNG_RI,
gRI(i))
        Next i

        For i=LBound(gNames) To UBound(gNames)
            If gNames(i) = IpTrim(sNominalLens) Then
                gMatchObj = i
                Exit For
            End If
        Next i

        gDOF = DOF(gMag(gMatchObj), gNA(gMatchObj),
gRI(gMatchObj))
        gNumPlanes = FOCAL_DISTANCE/(gDOF*FRACTION_DOF)
        If gNumPlanes < 5 Then gNumPlanes = 5
        If gNumPlanes Mod 2 = 0 Then gNumPlanes =
gNumPlanes + 1

    End If

    CheckObj = gMatchObj

End Function

' Autofocus routine, can stop as soon as focus critera
start to diminish
Private Function AutoFocus_ToMax(numPlanes As Integer, DOF
As Single, _
        firstBest As Boolean, statusStr As String) As
Boolean

    Dim fValue() As Single, bestValue As Single, bestIndex
As Integer
    Dim worstValue As Single, worstIndex As Integer
    Dim zDepth() As Single, zPos As Single
    Dim snapDoc As Integer, floatDoc As Integer
    Dim hStats(10) As Single
    Dim i As Integer, halfPlanes As Integer
    Dim dInfo As IPDOCINFO
    Dim bLive As Integer
    Dim bEndFlag As Integer

    bLive = IpAcqShow(ACQ_ISLIVE, bLive)
```

```vbnet
        If bLive <> 0 Then ret = IpAcqShow(ACQ_LIVE, 0)

    snapDoc = -1
    floatDoc = -1

    ' Test input to be an odd number
    If (numPlanes Mod 2) <> 1 Then numPlanes = numPlanes +
1

    If numPlanes < 3 Then numPlanes = 3
    halfPlanes = CInt(numPlanes / 2) - 1

    AutoFocus_ToMax = True

    ' Get the current stage position, in relative
coordinates
    ret = IpStageControl(GETZ, zPos)

    ' Calculate the limits of the Autofocus range
    ReDim fValue(0 To numPlanes-1) As Single
    ReDim zDepth(0 To numPlanes-1) As Single

    ' Set up locations
    For i=0 To numPlanes-1
        zDepth(i) = zPos + (i-halfPlanes) * DOF
    ' Debug.Print i; zDepth(i)
    Next i

    ret = IpMacroProgSetStr(MPROG_TITLE, 0, statusStr)
    ret = IpMacroProgSetStr(MPROG_TEXT, 0, "...")
    ret = IpMacroProgSetInt(MPROG_BUTTONTYPE, 0,
MPROG_BUTTON_CANCEL)
    ret = IpMacroProgSetInt(MPROG_NUMBUTTONS, 0, 1)

    ret = IpMacroProgShow(1)

    ' Iterate on depth
    For i=0 To numPlanes-1

        ret = IpMacroProgSetStr(MPROG_TEXT, 0, "Plane" &
Str(i+1) & " of" & Str(numPlanes))

        ret = IpStageZ(zDepth(i))

        ' Capture the best image
        If i=0 Then
            snapDoc = IpAcqSnap(ACQ_NEWEX)
            ret = IpPcTint(TINT_REMOVE)
```

179

```vbnet
            ret = IpDocGet(GETDOCINFO, snapDoc, dInfo)

            ipRect.Left = dInfo.Width / 4
            ipRect.Right = dInfo.Width * 3/4
            ipRect.top = dInfo.Height / 4
            ipRect.bottom = dInfo.Height * 3/4
            ret = IpAoiCreateBox(ipRect)
        Else
            ret = IpAppSelectDoc(snapDoc)
            ret = IpAoiShow(FRAME_NONE)

            OpenBrightfieldShutter()
            ret = IpAcqSnap(ACQ_CURRENTEX)
            ret = IpPcTint(TINT_REMOVE)

            ret = IpAoiShow(FRAME_RECTANGLE)
'           ret = IpWsCopy()
        End If

        ' Calculate variance on it
        If floatDoc < 0 Then
            floatDoc = IpWsConvertImage(IMC_FLOAT,
CONV_DIRECT, 0, 0, 0, 0)
            ret = IpHstCreate()
            ret = IpHstMinimize()
            ret = IpDocMinimize()
            ret = IpAppSelectDoc(floatDoc)
        Else
            ret = IpAppSelectDoc(floatDoc)
'           ret = IpWsPaste(0,0)
            ret = IpOpImageArithmetics(snapDoc, 0.0,
OPA_SET, 0)
        End If

        ret = IpFltVariance(3, 3)
        ret = IpHstUpdate()
        ret = IpHstGet(HSTGET_GETSTATS, 0, hStats(0))
        fValue(i) = hStats(2)

        ' Check against previous values
        If i = 0 Then
            bestIndex = 0
            bestValue = fValue(i)
            worstIndex = 0
            worstValue = fValue(i)
        Else
            If fValue(i) > bestValue Then
```

180

```vba
                bestIndex = i
                bestValue = fValue(i)
            End If
            If fValue(i) < worstValue Then
                worstIndex = i
                worstValue = fValue(i)
            End If
        End If

        If firstBest = True Then
            If fValue(i) < bestValue Then
                GoTo ReturnBest
            End If
        End If

        ret = IpMacroProgGet(MPROG_FLAG, 0, bEndFlag)

        ' Cancel...
        If bEndFlag <> 0 Then
            bestIndex = halfPlanes
            GoTo ReturnBest
        End If

    Next i

ReturnBest:
    ' Check for blanks...
    If worstValue = bestValue Then bestIndex = halfPlanes

    ret = IpMacroProgShow(0)

    ret = IpDocCloseEx(snapDoc)
    ret = IpDocCloseEx(floatDoc)

    ret = IpStageZ(zDepth(bestIndex))
    If bLive <> 0 Then ret = IpAcqShow(ACQ_LIVE, bLive)

End Function

' Get Objective information
Private Sub Mag_settings()
    Dim nLenses As Long, i As Long
    Dim sTmp As String*256

    ' Get whatever the last lens used was
    Dim sNominalLens As String*256
```

```
        ret = IpIniFileStr(INICMDSTR_GETSTRING, "Nominal
Objective", sNominalLens)
    If ret < 0 Then sNominalLens = ""

    ' Obtain information about the current set of lenses
    ret = IpLensGetLong(LENSGETLNG_NUMLENSES, nLenses)

    If nLenses < 1 Then Exit Sub

    ReDim gNames(0 To nLenses-1) As String
    ReDim gNA(0 To nLenses-1) As Single
    ReDim gMag(0 To nLenses-1) As Single
    ReDim gRI(0 To nLenses-1) As Single

    For i=0 To nLenses-1
        ret = IpLensGetStr(LENS_LIST, i, sTmp)
        gNames(i) = IpTrim(sTmp)
        ret = IpLensGetSng(gNames(i),
LENSGETSNG_MAGNIFICATION, gMag(i))
        ret = IpLensGetSng(gNames(i), LENSGETSNG_NA,
gNA(i))
        ret = IpLensGetSng(gNames(i), LENSGETSNG_RI,
gRI(i))
    Next i

    ' Present a dialog allowing the user to select the lens
    Begin Dialog UserDialog 370,175,"Lens
Selection",.dlgLensSelect '%GRID:10,7,1,1
        OKButton 140,147,90,21
        Text 20,14,90,14,"Objective:",.Text1
        DropListBox 130,14,220,105,gNames(),.DropListObj
        GroupBox 20,42,330,91,"Objective
Information",.GroupBox1
        Text 60,63,250,63,"ObjInfo",.ObjInfo
        PushButton 40,147,40,21,"?",.LensHelp
    End Dialog
    Dim dlg As UserDialog

    ret = Dialog( dlg )

End Sub

' Utility function to calculate a rough DOF for a
particular objective
' Use 550 nm as the expected wavelength, output in mm.
Private Function DOF(mag As Single, na As Single, ri As
Single) As Single
```

```vb
    Dim resolution As Single

    resolution = 0.61/na * 0.55

    DOF = ((0.55*ri) / na^2.0 + (ri/(mag*na)) * resolution)
    DOF = DOF / 1000.0
End Function

Rem See DialogFunc help topic for more information.
Private Function dlgLensSelect(DlgItem$, Action%,
SuppValue?) As Boolean
    Dim sNominal As String*256
    Dim sText As String
    Dim i As Integer

    Select Case Action%
    Case 1 ' Dialog box initialization
        Call SetWindPos("Lens Selection dialog")

        ret = IpIniFileStr(INICMDSTR_GETSTRING, "Nominal
Objective", sNominal)
        If ret < 0 Then sNominal = ""

        If IpTrim(sNominal) = "" Then
            sText = "No lens selected"
            gMatchObj = -1
        Else
            For i=LBound(gNames) To UBound(gNames)
                If gNames(i) = IpTrim(sNominal) Then
                    gMatchObj = i
                    Exit For
                End If
            Next i

            sText = StrObjInfo(gMatchObj)
        End If

        DlgValue "DropListObj", gMatchObj
        DlgText "ObjInfo", sText

    Case 2 ' Value changing or button pressed
        dlgLensSelect = True ' Prevent button press from
closing the dialog box

        Select Case DlgItem$
        Case "DropListObj"
            gMatchObj = DlgValue("DropListObj")
```

```vba
            sText = StrObjInfo(gMatchObj)
            DlgText "ObjInfo", sText

            ret = IpIniFileStr(INICMDSTR_SETSTRING, _
"Nominal Objective", gNames(gMatchObj))

        Case "OK"
            Call RecWindPos("Lens Selection dialog")
            dlgLensSelect = False

        Case "LensHelp"
            ret = IpMacroStop("Select a lens from the _
defined list" + vbCr + _
                "of objectives for focus and alignment", 0)
            ret = IpMacroStop("If the lens you are using is _
not defined," + vbCr + _
                "exit the dialog, open 'Edit | Lens _
List...'," + vbCr + _
                "add it, and return here to select it for" _
+ vbCr + _
                "alignment and focus.", 0)

        End Select

    Case 3 ' TextBox or ComboBox text changed
    Case 4 ' Focus changed
    Case 5 ' Idle
        Rem Wait .1 : dlgLensSelect = True ' Continue _
getting idle actions
    Case 6 ' Function key
    End Select

End Function

Private Function StrObjInfo(match As Integer)
    Dim sText As String

    sText = "Magnification" + vbTab + Str(gMag(match)) + _
"x" + vbCrLf
    sText = sText + "RI" + vbTab + vbTab + Str(gRI(match)) _
+ vbCrLf
    sText = sText + "NA" + vbTab + vbTab + Str(gNA(match)) _
+ vbCrLf
    sText = sText + vbCrLf
    sText = sText + "DOF @ 550nm" + vbTab + _
        FormatNumber(DOF(gMag(match), gNA(match), _
gRI(match))*1000.0) + " microns"
```

```vba
    StrObjInfo = sText
End Function


' Utility function for displaying a large range of numbers
Private Function FormatNumber(fNum As Single) As String
    Dim fString As String

    fString = "0.0"

    If Abs(fNum) >= 1000000.0 Then fString = "0.0000E+00"
    If Abs(fNum) < 100.0 Then fString = "0.000"
    If Abs(fNum) < 10.0 Then fString = "0.0000"
    If Abs(fNum) < 0.1 Then fString = "0.000E+00""
    If Abs(fNum) = 0.0 Then fString = "0"

    FormatNumber = Format(fNum, fString)
End Function


Private Sub OutputCoordinates

    'Error checking (are we in the same place?)
    Dim xcorr As Single, ycorr As Single, xcurr As Single,
ycurr As Single, zcurr As Single
    Dim absXYZ(0 To 2) As Single

    ret = IpStageGetAbsPosition(absXYZ(0))
    ret = IpStageGet(STG_GET_X_CORRECTION,0,xcorr)
    ret = IpStageGet(STG_GET_Y_CORRECTION,0,ycorr)
    ret = IpStageControl(GETX, xcurr)
    ret = IpStageControl(GETY, ycurr)
    ret = IpStageControl(GETZ, zcurr)
    IpOutputShow(1)
    IpOutput("Absolute X: " + CStr(absXYZ(0)) + "   " +
"Absolute Y: " + CStr(absXYZ(1)) + "   " +"Absolute Z: " +
CStr(absXYZ(2)) + vbLf)
    IpOutput("Current X: " + CStr(xcurr) + "   " + "Current
Y: " + CStr(ycurr) + "   " + "Current Z: " + CStr(zcurr) +
vbLf)
    IpOutput("Fiducial X: " + CStr(gFiducial(0)) + "   " +
"Fiducial Y: " + CStr(gFiducial(1)) + vbLf)
    IpOutput("XCorr: " + CStr(xcorr) + "   " + "YCorr: " +
CStr(ycorr) + vbLf)
    IpOutput("   ")

End Sub
```

```
Sub MoveOriginToA1Center_24Well()

    Dim sTmpZ As Single, sA1Z As Single, PFOffset As Single

    If Not gbIsInit Then
        Call InitSettings()
    End If

    ' Take the user to general location, ask for
confirmation
    ret = IpStageXY(gCurrPosX+g24Well(0),
gCurrPosY+g24Well(1))
    ret = IpStageControl(GETZ,sTmpZ)
    sA1Z = sTmpZ + g24Well(2)
    ret = IpStageAbsZ(sA1Z)

    WaitZPosition(sA1Z)
    UpdateCurrPos()

End Sub

Private Sub MoveOriginToA1Center()

    Dim sTmpZ As Single, sA1Z As Single, PFOffset As Single

    If Not gbIsInit Then
        Call InitSettings()
    End If

    ' Take the user to general location, ask for
confirmation
    ret = IpStageXY(gCurrPosX+gWell(0), gCurrPosY+gWell(1))
    ret = IpStageControl(GETZ,sTmpZ)
    sA1Z = sTmpZ + gWell(2)
    ret = IpStageAbsZ(sA1Z)

    WaitZPosition(sA1Z)
    UpdateCurrPos()

End Sub

Private Sub FineFocus()

    OpenBrightfieldShutter()
    ret = AutoFocus_ToMax(gNumPlanes, gDOF*FRACTION_DOF,
False, "Fine focusing well center")
    CloseBrightfieldShutter()
```

```vb
End Sub

Private Sub CoarseFocus()

    OpenBrightfieldShutter()
    ret = AutoFocus_ToMax(gNumPlanes,
gDOF*FRACTION_DOF*(gNumPlanes/2), False, "Coarse focusing
well center")
    CloseBrightfieldShutter()

End Sub

Sub UpdateCurrPos()

    'Initialize the global array that holds the current X
and Y positions of the stage
    ret = IpStageControl(GETX,gCurrPosX)
    ret = IpStageControl(GETY,gCurrPosY)

End Sub
Sub MoveOneWellRight_24W()

    ret =
IpStageXY(gCurrPosX+X_INTERWELL_DIST_24W,gCurrPosY)
    UpdateCurrPos()

End Sub


Sub MoveOneWellRight()

    ret = IpStageXY(gCurrPosX+X_INTERWELL_DIST,gCurrPosY)
    UpdateCurrPos()

End Sub
Sub MoveOneWellLeft_24W()

    ret = IpStageXY(gCurrPosX-
X_INTERWELL_DIST_24W,gCurrPosY)
    UpdateCurrPos()

End Sub

Sub MoveOneWellLeft()

    ret = IpStageXY(gCurrPosX-X_INTERWELL_DIST,gCurrPosY)
```

```vb
    UpdateCurrPos()

End Sub

Sub MoveOneWellUp_24W()

    ret = IpStageXY(gCurrPosX,gCurrPosY-
Y_INTERWELL_DIST_24W)
    UpdateCurrPos()

End Sub

Sub MoveOneWellUp()

    ret = IpStageXY(gCurrPosX,gCurrPosY-Y_INTERWELL_DIST)
    UpdateCurrPos()

End Sub
Sub MoveOneWellDown_24W()

    ret =
IpStageXY(gCurrPosX,gCurrPosY+Y_INTERWELL_DIST_24W)
    UpdateCurrPos()

End Sub

Sub MoveOneWellDown()

    ret = IpStageXY(gCurrPosX,gCurrPosY+Y_INTERWELL_DIST)
    UpdateCurrPos()

End Sub

Private Sub MoveToA1Center()

    ret = IpStageXY(gA1Center(0),gA1Center(1))
    UpdateCurrPos()

End Sub

Private Sub MoveToAbsoluteXY(xAbsPos As Single, yAbsPos As
Single)

    ret = IpStageXY(xAbsPos,yAbsPos)
    UpdateCurrPos()

End Sub
```

```vb
Private Sub PlateAcquire_24BRG()

    Dim strAppDir As String, strDir As String, strIm As
String
    Dim imIdx As Integer, i As Integer

    ret = IpAppGetStr(APPGETSTR_GETAPPDIR, 0, strAppDir)

    'Check if PlateImages directory exists
    strDir = Dir(IpTrim(strAppDir) + "PlateImages",
vbDirectory)
    If strDir = "" Then
        MkDir IpTrim(strAppDir) + "PlateImages"
    End If

    strDir = IpTrim(strAppDir) + "PlateImages" + "\"
    strIm = gstrPlateID

    'Change to specified polychroic
    ret = IpScopeSetPosition(SCP_FWHEEL1, TURRET_POS)
    'Change to specified objective
    ret = IpScopeSetPosition(SCP_OBJECTIVE, OBJECTIVE_POS)
    'Load exposure file
    ret = IpAcqSettings(EXP_FILE,0)
    'Change to arc lamp shutter
    ret = IpScopeControl(SCP_SETCURRSHUTTER, 0, 0, "",
IPNULL)

    'Moves through all of the wells of a 24 well plate and
acquires brightfield, GFP, and RFP Images
    For i=1 To (NUM_ROW_24WELL/2) Step 1

        SingleRowCapture_24Well(strDir, strIm, 1, 2*i-1)
        PerfectFocusOFF()
        MoveOneWellDown_24W()
        PerfectFocusON()

        SingleRowCapture_24Well(strDir, strIm, -1, 2*i)
        If i<>(NUM_ROW_24WELL/2) Then
            PerfectFocusOFF()
            MoveOneWellDown_24W()
            PerfectFocusON()
        End If

    Next i
```

```vba
    ' Only execute if there is an odd number of rows
defined
    If (NUM_ROW_24WELL Mod 2) Then
        SingleRowCapture_24Well(strDir, strIm, 1, 2*i-1)
    End If

End Sub

Private Sub PlateAcquire_96BRG()

    Dim strAppDir As String, strDir As String, strIm As
String
    Dim imIdx As Integer, i As Integer

    'strDir = IpTrim(strAppDir) + "PlateImages" + "\"
    strDir = "D:\IPWIN70\PlateImages\"
    strIm = gstrPlateID

    'Change to specified polychroic
    ret = IpScopeSetPosition(SCP_FWHEEL1, TURRET_POS)
    'Change to specified objective
    ret = IpScopeSetPosition(SCP_OBJECTIVE, OBJECTIVE_POS)
    'Load exposure file
    ret = IpAcqSettings(EXP_FILE,0)
    'Change to arc lamp shutter
    ret = IpScopeControl(SCP_SETCURRSHUTTER, 0, 0, "",
IPNULL)

    'Moves through all of the wells of a 96 well plate and
acquires brightfield, GFP, and RFP Images
    For i=1 To (NUM_ROW_96WELL/2) Step 1

        SingleRowCapture_96Well(strDir, strIm, 1, 2*i-1)
        PerfectFocusOFF()
        MoveOneWellDown()
        PerfectFocusON()

        ' If it is not the last well to capture
        SingleRowCapture_96Well(strDir, strIm, -1, 2*i)
        If i<>(NUM_ROW_96WELL/2) Then
            PerfectFocusOFF()
            MoveOneWellDown()
            PerfectFocusON()
        End If

    Next i
```

```vba
     ' Only execute if there is an odd number of rows
defined
     If (NUM_ROW_96WELL Mod 2) Then
         SingleRowCapture_96Well(strDir, strIm, 1, 2*i-1)
     End If

End Sub

Private Sub SingleWellCapture(strDir As String, strIm As
String, numImY As Single, numImX As Single)

    Dim i As Integer, j As Integer
    Dim tempCurrPosX As Single, tempCurrPosY As Single
    Dim strImMod As String

    tempCurrPosX = gCurrPosX
    tempCurrPosY = gCurrPosY

    MoveStageByFrames(-(numImX/2-.5),-(numImY/2-.5))

    For i = 1 To numImY Step 1

        For j = 1 To numImX Step 1
            strImMod = strIm + "_" + CStr(numImX*(i-1)+j)
            SingleFrameCapture(strDir,strImMod,i,j)
            If Not (j=numImX) Then
                If ((i Mod 2) = 0) Then
                    MoveOneFrameLeft()
                Else
                    MoveOneFrameRight()
                End If
            End If
        Next j

        If Not (i=numImY) Then
            MoveOneFrameDown()
        End If

    Next i

    IpStageXY(tempCurrPosX, tempCurrPosY)
    UpdateCurrPos()

End Sub

Private Sub SingleFrameCapture(strDir As String, strIm As
String, idxImY As Integer, idxImX As Integer)
```

191

```vba
    Dim strImDate As String*255, strImDateFormatted As
String
    Dim snapIm As Integer

    ' Add the loop number onto the file name
    If IS_LOOP = 1 Then
        strIm = strIm + "_L" + CStr(gLoopNum)
    End If

'--------------------------- Photoswitch ----------------
------------'

    If PHOTOSWITCHFLAG = 1 Then
        'Photoswitch -> Needs configuration
        snapIm = IpScopeAcquire(ACQ_NEW)
        ret = IpPcTint(TINT_REMOVE)
        IpDocClose()
    End If

'--------------------------- Brightfield ----------------
------------'

    If BFFLAG = 1 Then

        If (idxImY=2 And idxImX=2) Then
            'Brightfield -> Needs configuration
            ret = IpScopeSetPosition(SCP_LAMP1, 30)
            snapIm = IpScopeAcquire(ACQ_NEW)
            ret = IpPcTint(TINT_REMOVE)
        End If
TryBFSave:
        IpWsSaveAs(strDir + "Brightfield" + "\" + strIm +
"_BF" +".tif","TIF")
        If ret=0 Then
            IpDocClose()
        Else
            GoTo TryBFSave
        End If
    End If

'--------------------------- BFP ------------------------
-----'

    If BFPFLAG = 1 Then
        If TURRET_POS = 0 Then
            ret = IpScopeSetPosition(SCP_FWHEEL2, 0) '
```

```vbscript
                ret = IpScopeSetPosition(SCP_FWHEEL3, 0) '
        ElseIf TURRET_POS = 2 Then
                ret = IpScopeSetPosition(SCP_FWHEEL2, 6) '
                ret = IpScopeSetPosition(SCP_FWHEEL3, 0) '
        End If
        snapIm = IpScopeAcquire(ACQ_NEW)
TryBFPSave:
        ret = IpWsSaveAs(strDir + "BFP" + "\" + strIm +
"_BFP" + ".tif","TIF")
        If ret=0 Then
            IpDocClose()
        Else
            GoTo TryBFPSave
        End If
    End If

'-------------------------- CFP ------------------------
-----'

    If CFPFLAG = 1 Then
        'CFP -> Needs configuration
        ret = IpScopeSetPosition(SCP_FWHEEL2, 3) '
        ret = IpScopeSetPosition(SCP_FWHEEL3, 3) '
        snapIm = IpScopeAcquire(ACQ_NEW)
TryCFPSave:
        ret = IpWsSaveAs(strDir + "CFP" + "\" + strIm +
"_CFP" + ".tif","TIF")
        If ret=0 Then
            IpDocClose()
        Else
            GoTo TryCFPSave
        End If
    End If

'-------------------------- GFP ------------------------
-----'

    If GFPFLAG = 1 Then
        'GFP
        If TURRET_POS = 0 Then
            ret = IpScopeSetPosition(SCP_FWHEEL2, 1) '
            ret = IpScopeSetPosition(SCP_FWHEEL3, 1) '
        ElseIf TURRET_POS = 2 Then
            ret = IpScopeSetPosition(SCP_FWHEEL2, 1) '
            ret = IpScopeSetPosition(SCP_FWHEEL3, 7) '
        End If
        snapIm = IpScopeAcquire(ACQ_NEW)
```

```
TryGFPSave:
        ret = IpWsSaveAs(strDir + "GFP" + "\" + strIm +
"_GFP" + ".tif","TIF")
        If ret=0 Then
            IpDocClose()
        Else
            GoTo TryGFPSave
        End If
    End If

'-------------------------- YFP ------------------------
-----'

    If YFPFLAG = 1 Then
        'YFP -> Needs configuration
        ret = IpScopeSetPosition(SCP_FWHEEL2, 4) 'S500/20x
        ret = IpScopeSetPosition(SCP_FWHEEL3, 4) 'S535/30m
        snapIm = IpScopeAcquire(ACQ_NEW)
TryYFPSave:
        ret = IpWsSaveAs(strDir + "YFP" + "\" + strIm +
"_YFP" + ".tif","TIF")
        If ret=0 Then
            IpDocClose()
        Else
            GoTo TryYFPSave
        End If
    End If

'-------------------------- RFP ------------------------
-----'

    If RFPFLAG = 1 Then
        'RFP
        If TURRET_POS = 0 Then
            ret = IpScopeSetPosition(SCP_FWHEEL2, 2) '
            ret = IpScopeSetPosition(SCP_FWHEEL3, 2) '
        ElseIf TURRET_POS = 1 Then
            ret = IpScopeSetPosition(SCP_FWHEEL2, 5) '
            ret = IpScopeSetPosition(SCP_FWHEEL3, 5) '
        ElseIf TURRET_POS = 2 Then
            ret = IpScopeSetPosition(SCP_FWHEEL2, 8) '
            ret = IpScopeSetPosition(SCP_FWHEEL3, 8) '
        End If
        snapIm = IpScopeAcquire(ACQ_NEW)
TryRFPSave:
        ret = IpWsSaveAs(strDir + "RFP" + "\" + strIm +
"_RFP" + ".tif","TIF")
```

```vba
        If ret=0 Then
            IpDocClose()
        Else
            GoTo TryRFPSave
        End If
    End If


'-------------------------- CY5 -------------------------
-----'

    If CY5FLAG = 1 Then
        'CY5
        ret = IpScopeSetPosition(SCP_FWHEEL2, 9) 'S500/20x
        ret = IpScopeSetPosition(SCP_FWHEEL3, 9) 'S535/30m
        snapIm = IpScopeAcquire(ACQ_NEW)
TryCY5Save:
        ret = IpWsSaveAs(strDir + "CY5" + "\" + strIm +
"_CY5" + ".tif","TIF")
        If ret=0 Then
            IpDocClose()
        Else
            GoTo TryCY5Save
        End If
    End If

End Sub

Private Sub SingleRowCapture_24Well(strDir As String, strIm
As String, xDir As Single, intRowNum As Integer)

    Dim i As Integer
    Dim strImLong As String, strWell As String

    If xDir = 1 Then 'move in positive x direction when
acquiring
        For i = 1 To NUM_COL_24WELL Step 1
            strWell = GetWellString(intRowNum,i)
            strImLong = strIm + "-" + strWell
            SingleWellCapture(strDir, strImLong,
NUM_TILES_Y, NUM_TILES_X)
            If i <> NUM_COL_24WELL Then
                PerfectFocusOFF()
                MoveOneWellRight_24W()
                PerfectFocusON()
            End If
        Next i
    ElseIf xDir = -1 Then 'move in negative x direction
```

```vbnet
when acquiring
        For i = NUM_COL_24WELL To 1 Step -1
            strWell = GetWellString(intRowNum,i)
            strImLong = strIm + "-" + strWell
            SingleWellCapture(strDir, strImLong,
NUM_TILES_Y, NUM_TILES_X)
            If i <> 1 Then
                PerfectFocusOFF()
                MoveOneWellLeft_24W()
                PerfectFocusON()
            End If
        Next i
    End If


End Sub

Private Sub SingleRowCapture_96Well(strDir As String, strIm
As String, xDir As Single, intRowNum As Integer)

    Dim i As Integer
    Dim strImLong As String, strWell As String

    If xDir = 1 Then 'move in positive x direction when
acquiring
        For i = 1 To NUM_COL_96WELL Step 1
            strWell = GetWellString(intRowNum,i)
            strImLong = strIm + "_" + strWell
            SingleWellCapture(strDir, strImLong,
NUM_TILES_Y, NUM_TILES_X)
            If i <> NUM_COL_96WELL Then
                PerfectFocusOFF()
                MoveOneWellRight()
                PerfectFocusON()
            End If
        Next i
    ElseIf xDir = -1 Then 'move in negative x direction
when acquiring
        For i = NUM_COL_96WELL To 1 Step -1
            strWell = GetWellString(intRowNum,i)
            strImLong = strIm + "_" + strWell
            SingleWellCapture(strDir, strImLong,
NUM_TILES_Y, NUM_TILES_X)
            If i <> 1 Then
                PerfectFocusOFF()
                MoveOneWellLeft()
                PerfectFocusON()
```

```vba
            End If
        Next i
    End If

End Sub

Private Function FormatDateString(strDateIn As String) As
String

    Dim dateIm, strFormatDate As String

    dateIm = Now()
    strFormatDate = CStr(Month(dateIm)) + CStr(Day(dateIm))
+ CStr(Year(dateIm)) + "-" + CStr(Hour(dateIm)) +
CStr(Minute(strDateIn)) + CStr(Second(dateIm))
    FormatDateString = strFormatDate

End Function

Private Function GetWellString(intRowNum As Integer,
intColNum As Integer) As String

    Dim strWellAlphaArr(1 To 8) As String

    strWellAlphaArr(1) = "A"
    strWellAlphaArr(2) = "B"
    strWellAlphaArr(3) = "C"
    strWellAlphaArr(4) = "D"
    strWellAlphaArr(5) = "E"
    strWellAlphaArr(6) = "F"
    strWellAlphaArr(7) = "G"
    strWellAlphaArr(8) = "H"

    GetWellString = strWellAlphaArr(intRowNum) +
CStr(intColNum)

End Function

Private Sub GoToFiducial_24Well()

    If Not gbIsInit Then
        Call InitSettings()
    End If

    ' Move to the generic fiducial location
    ret = IpStageXY(g24Fiducial(0), g24Fiducial(1))
    ret = IpStageAbsZ(g24Fiducial(2))
```

```vba
    WaitZPosition(g24Fiducial(2))

    'Call CoarseFocus()
    'Call FineFocus()

End Sub


Private Sub GoToFiducial()

    If Not gbIsInit Then
        Call InitSettings()
    End If

    ' Move to the generic fiducial location
    ret = IpStageXY(gFiducial(0), gFiducial(1))
    ret = IpStageAbsZ(gFiducial(2))

    WaitZPosition(gFiducial(2))

    'Call CoarseFocus()
    'Call FineFocus()

End Sub

Private Sub WaitZPosition(zPosition As Single)

    Dim sZpos As Single

GetZPosition:
    ret = IpStageControl(GETZ,sZpos)

    If (sZpos > (zPosition-.01)) And (sZpos <
(zPosition+.01)) Then
        Exit Sub
    Else
        GoTo GetZPosition
    End If

End Sub

Private Sub OpenBrightfieldShutter()

    ret = IpScopeSetPosition(SCP_SHUTTER2, 1)

End Sub
```

```vbnet
Private Sub CloseBrightfieldShutter()

    ret = IpScopeSetPosition(SCP_SHUTTER2, 0)

End Sub

Private Sub AcquireRefImage()

    Dim offsetX As Single, offsetY As Single, offsetZ As Single
    Dim strAppDir As String*255, strFName As String
    Dim strPlateIm As String, strPlateOffset As String
    Dim xFid As Single, yFid As Single
    Dim xOrigin As Single, yOrigin As Single, zOrigin As Single
    Dim fAbs(0 To 2) As Single
    Dim snapIm As Single

    ret = IpStageControl(GETX, xFid)
    ret = IpStageControl(GETY, yFid)
    ret = IpStageGetAbsPosition(fAbs(0))

    ' Offset by scan size
    ret = IpStageControl(GETX, xOrigin)
    ret = IpStageControl(GETY, yOrigin)
    ret = IpStageControl(GETZ, zOrigin)

    offsetX = xOrigin - xFid
    offsetY = yOrigin - yFid
    offsetZ = zOrigin

    ret = IpAppGetStr(APPGETSTR_GETAPPDIR, 0, strAppDir)
    strFName = Dir(IpTrim(strAppDir) + "RefImage", vbDirectory)
    If strFName = "" Then
        MkDir IpTrim(strAppDir) + "RefImage"
    End If

    strPlateIm = IpTrim(strAppDir) + "RefImage" + "\" + gstrPlateID + ".tif"
    strPlateOffset = IpTrim(strAppDir) + "RefImage" + "\" + gstrPlateID + ".Offset"

    Open strPlateOffset For Output As #1
    Write #1, OFFSET_FILE_VERSION
    Write #1, fAbs(0)
```

```
    Write #1, fAbs(1)
    Write #1, offsetX
    Write #1, offsetY
    Write #1, offsetZ
    Close #1

    'Acquire and Save the reference image
    snapIm = IpScopeAcquire(ACQ_NEW)
    ret = IpPcTint(TINT_REMOVE)
    ret = IpWsSaveAs(strPlateIm, "TIF")

End Sub

Sub PerfectFocusON()

    ret = IpScopeSetPosition(SCP_CONTINUOUSFOCUS, 1)

End Sub

Sub PerfectFocusOFF()

    ret = IpScopeSetPosition(SCP_CONTINUOUSFOCUS, 0)

End Sub

Sub MoveOneFrameUp()

    ret = IpStageXY(gCurrPosX,gCurrPosY-(HEIGHT_PIXELS-
MONTAGE_OVERLAP_PIXELS)/gPixelsPerMM)
    UpdateCurrPos()

End Sub

Sub MoveOneFrameDown()

    ret = IpStageXY(gCurrPosX,gCurrPosY+(HEIGHT_PIXELS-
MONTAGE_OVERLAP_PIXELS)/gPixelsPerMM)
    UpdateCurrPos()

End Sub

Sub MoveOneFrameRight()

    ret = IpStageXY(gCurrPosX+(WIDTH_PIXELS-
MONTAGE_OVERLAP_PIXELS)/gPixelsPerMM,gCurrPosY)
    UpdateCurrPos()
```

```vba
End Sub

Sub MoveOneFrameLeft()

    ret = IpStageXY(gCurrPosX-(WIDTH_PIXELS-
MONTAGE_OVERLAP_PIXELS)/gPixelsPerMM,gCurrPosY)
    UpdateCurrPos()

End Sub

Sub MoveStageByFrames (xFrames As Single, yFrames As
Single)

    Dim xMM As Single, yMM As Single

    xMM = xFrames*(WIDTH_PIXELS-
MONTAGE_OVERLAP_PIXELS)/gPixelsPerMM
    yMM = yFrames*(HEIGHT_PIXELS-
MONTAGE_OVERLAP_PIXELS)/gPixelsPerMM

    ret = IpStageXY(gCurrPosX+xMM,gCurrPosY+yMM)
    UpdateCurrPos()

End Sub

Private Sub Pause(pTimeMsec As Long)

    Dim StartTime As Long

    StartTime = timeGetTime

    While timeGetTime - StartTime < pTimeMsec
        DoEvents
    Wend

End Sub

Private Sub ChangeExcitationWheel()
    ret = IpScopeSetPosition(SCP_FWHEEL2, 5)
End Sub

Private Sub ChangeEmissionWheel()
    ret = IpScopeSetPosition(SCP_FWHEEL3, 6)
End Sub

Private Sub ChangeTurret()
    ret = IpScopeSetPosition(SCP_FWHEEL1, 2)
```

```vb
End Sub

Private Sub ChangeObjective()
    ret = IpScopeSetPosition(SCP_OBJECTIVE, 2)
End Sub

Private Sub ChangeShutter()
    ret = IpScopeControl(SCP_SETCURRSHUTTER, 0, 0, "",
IPNULL)
End Sub

Private Sub SecureGate(intStatus As Integer)

    Select Case intStatus
    Case 0
        'Open stage secure gate
        ret = IpStageXYWrite("secure x=1.0"+
Chr(13)+Chr(10),50)
    Case 1
        'Close stage secure gate
        ret = IpStageXYWrite("secure x=0.5"+
Chr(13)+Chr(10),50)
    Case Else
        'Do nothing
    End Select

End Sub

Private Function CalculateAlignment() As POINTAPI

    Dim ptOffset As POINTAPI
    Dim xOffsetMM As Single, yOffsetMM As Single
    Dim imgIDs(0 To 1) As Integer

    ret = IpAlignRemove(DOCSEL_ALL, -1)

    IpDocGet(GETDOCLST,2,imgIDs(0))
    ret = IpAlignAdd(imgIDs(0), -1)
    ret = IpAlignAdd(imgIDs(1), -1)

    ret = IpAlignSetInt(ALGN_TRIMBORDERS, 0, 1)
    ret = IpAlignSetInt(ALGN_OPTIONS, ALGN_ROTATE, 0)
    ret = IpAlignSetInt(ALGN_OPTIONS, ALGN_SCALE, 0)
    ret = IpAlignSetInt(ALGN_OPTIONS, ALGN_TRANSLATE, 1)
    ret = IpAlignSetInt(ALGN_ALG_OPTION, ALGN_METHOD,
ALGN_FFTPHASE)
    ret = IpAlignSetInt(ALGN_ALWAYSRECALC, 0, 1)
```

```vba
    ret = IpAlignCalculate()
    ret = IpAlignGet(ALGN_BEST_OFFSET, 1, ptOffset)

    CalculateAlignment = ptOffset

End Function

Sub OpenGate()
    SecureGate(0)
End Sub

Sub CloseGate()
    SecureGate(1)
End Sub

Sub FocusOnFiducial()
    Dim absXYZ(0 To 2) As Single, PFOffset As Single, sZpos
As Single, sZposLow As Single
    Dim FiducialOffset As POINTAPI, xOffsetMM As Single,
yOffsetMM As Single, ipStgSpd As Single, ipStepSize As
Single

    Dim fVal_old As Single, fVal_new As Single
    Dim floatDoc As Integer
    Dim hStats(10) As Single
    Dim i As Integer

    'Initialization
    Call InitSettings()

    'Change stage speed to maximum
    ipStgSpd = 100
    ret = IpStageControl(STG_SET_XY_SPEED, ipStgSpd)

    ret =
IpAcqSettings("D:\IPWIN70\Exposure\ANDOR_33MS_EXP.vpf",0)
    ret = IpScopeSettings("D:\IPWIN70\ScpConfig\20X
Brightfield (Camera).scp",SCP_LOAD)
    ret = IpScopeSetPosition(SCP_LAMP1, 3)

    'Close the stage secure gate
    SecureGate(1)

    'Register fiducial point on plate and make relative
move to Well A,1
    'Move to the Z Absolute Position
    GoToFiducial()
```

```
    ret = IpAcqControl(800, 1, IPNULL) ' ACQCMD_WSPREVW
    'Change to arc brightfield shutter
    ret = IpScopeControl(SCP_SETCURRSHUTTER, 0, 1, "",
IPNULL)
    'Open shutter
    ret = IpScopeSetPosition(SCP_CURRSHUTTER, 1)
    'Show live in current workspace
    ret = IpAcqShow(ACQ_LIVE,1) 'Show live image
    'Move Z Axis up until there is a decrease in contrast
    ret = IpStageZ(gFiducial(2)-0.02)


    'Initialize
    floatDoc = IpWsConvertImage(IMC_FLOAT, CONV_DIRECT, 0,
0, 0, 0)
    ret = IpHstCreate()
    ret = IpFltVariance(3, 3)
    ret = IpHstUpdate()
    ret = IpHstGet(HSTGET_GETSTATS, 0, hStats(0))
    fVal_old = hStats(2)


End Sub
```
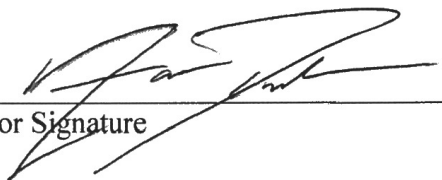Table 16. ImagePro Plus script to control automated microscope acquision.

Publishing Agreement

It is the policy of the University to encourage the distribution of all theses, dissertations, and manuscripts. Copies of all UCSF theses, dissertations, and manuscripts will be routed to the library via the Graduate Division. The library will make all theses, dissertations, and manuscripts accessible to the public and will preserve these to the best of their abilities, in perpetuity.

Please sign the following statement:

I hereby grant permission to the Graduate Division of the University of California, San Francisco to release copies of my thesis, dissertation, or manuscript to the Campus Library to provide access and preservation, in whole or in part, in perpetuity.

_____   ___9/1/2013___
Author Signature   Date